

# Direct Measurement of $W$ Boson Decay Width at DØ

by

Qichun Xu

A dissertation submitted in partial fulfillment  
of the requirements for the degree of  
Doctor of Philosophy  
(Physics)  
in the University of Michigan  
2001

Doctoral Committee:

Associate Professor Bing Zhou, Chair  
Professor J. Chapman  
Assistant Professor Yan Chen  
Assistant Professor James Liu  
Assistant Professor Georg Raithel

© Qichun Xu 2001  
ALL RIGHTS RESERVED

To my family

my parents, wife and son

# Acknowledgments

This dissertation is a cumulative effort of many years of research by a large number of people. I would like to thank everyone who has contributed to this work in various way.

First and foremost, I want to thank my advisor, Professor Bing Zhou, for her continuous support and encourage in this analysis and in my research at the University of Michigan. She has helped to get me started on this analysis that needed the initial input by someone experienced in high energy physics. In the analysis process, she helped me to find the solutions to some critical issues, from overall strategy to analysis details. Without her help, it is impossible to finish this dissertation.

At the University of Michigan, I am indebted to everyone in DØ group, which I spent the past three year to work with in one small team. I am very glad to have Professor Homer Neal in our group and he always encouraged me on my graduate physics study. Professor Jianming Qian deserves special recognition for his continuous suggestions and help in my thesis. Without the help from Beth Demkowski, my research on my thesis would not go so easily due to my frequent travel back and forth to Fermilab.

At DØ, I would like to thank all people in the electroweak group for their continuous support. From the beginning of this analysis, I am glad to have Neeti Parashar to work together on this analysis. Without the initial help from Slava Kulik, Miguel Mostafa and Georg Steinbrueck, I could not finish my thesis by now. They provide me the analysis tools and answer my enormous questions. Cecilia Gerber and Dylan Casey deserve special thanks for their help and support. They explained problems to me with great patience through the analysis process. I also

appreciate the help and encouragement from Harry Melanson, John Ellison, Ulrich Heintz, Tom Diehl and Darien Wood.

I also would like to thank my thesis committee member. In addition to my advisor and committee chair, Professor Bing Zhou, every member spent many time to read my thesis and provide me many helpful information. Professor J. Chapman and Professor James Liu deserve the special recognition for their efforts.

My time at Fermilab would not have been so enjoyable without these friends such as Zhongmin Wang, Jundong Huang, Chunhui Luo, Chunhui Han and Yimei Huang. We shared a lot of common feeling, experience and happiness.

The greatest thanks should go to my family. My wife, Qiao, has always been supportive in this research. Special thanks also go to my son Jingwei, who brings so much fun and excitement into our lives. He always has lots of questions waiting for me. Sometimes, his questions are really hard for me to answer with all my knowledge from books and experience.

Finally, I am very grateful to my parents for their love, encourage and support over the past decades. They always have much more confidence in me than I have in myself.

# Contents

<b>1</b>	<b>The Standard Model and the <math>W</math> Decay Width</b>	<b>1</b>
1.1	Introduction . . . . .	1
1.2	The Standard Model . . . . .	5
1.2.1	Elementary Particles in the SM . . . . .	5
1.2.2	Electroweak Theory . . . . .	8
1.2.3	Higgs Mechanism . . . . .	13
1.2.4	$W$ Decay Width . . . . .	14
1.3	$W$ Production and Decay . . . . .	15
1.3.1	$W$ Production at Tevatron . . . . .	15
1.3.2	Decay of the $W$ Boson . . . . .	16
1.4	$W$ Width Measurement . . . . .	17
1.4.1	Motivation . . . . .	17
1.4.2	Indirect Measurement . . . . .	17
1.4.3	Direct Measurement . . . . .	18
1.4.4	Challenge of the Direct Measurement . . . . .	19
<b>2</b>	<b>The DØ Experiment at Tevatron</b>	<b>22</b>
2.1	The Tevatron $p\bar{p}$ Collider at Fermilab . . . . .	22
2.2	Overview of the DØ Detector . . . . .	26
2.3	The Central Detector . . . . .	27
2.3.1	The Vertex Chamber . . . . .	29
2.3.2	The Transition Radiation Detector . . . . .	29

2.3.3	The Central Drift Chamber . . . . .	30
2.3.4	The Forward Drift Chambers . . . . .	31
2.4	The Calorimeter . . . . .	32
2.4.1	Overview of Calorimeter . . . . .	32
2.4.2	Central Calorimeter . . . . .	37
2.4.3	Endcap Calorimeter . . . . .	38
2.4.4	Intercryostat Detectors and Massless Gaps . . . . .	38
2.4.5	Calorimeter Calibration . . . . .	39
2.5	The Muon System . . . . .	40
2.6	The Trigger System for Data Acquisition . . . . .	41
2.6.1	Level-0 . . . . .	43
2.6.2	Level-1 . . . . .	43
2.6.3	Level-2 . . . . .	44
<b>3</b>	<b>Event Reconstruction and Selection</b>	<b>46</b>
3.1	Event Reconstruction . . . . .	46
3.2	Electron Identification . . . . .	47
3.2.1	Electromagnetic Energy Fraction . . . . .	48
3.2.2	Shower Shape Analysis . . . . .	48
3.2.3	Shower Isolation . . . . .	51
3.2.4	Track Matching . . . . .	52
3.2.5	The Four Variable Likelihood Function . . . . .	54
3.2.6	Off-line Electron Selection . . . . .	56
3.3	Neutrino Identification . . . . .	58
3.4	$W \rightarrow e\nu$ Event Selection . . . . .	58
3.4.1	$W \rightarrow e\nu$ Trigger . . . . .	59
3.4.2	$W \rightarrow e\nu$ Off-line Selection . . . . .	60
3.5	$Z \rightarrow ee$ Event Selection . . . . .	60

3.5.1	$Z \rightarrow ee$ Trigger . . . . .	61
3.5.2	$Z \rightarrow ee$ Off-line Selection . . . . .	62
3.6	Event Displays . . . . .	62
<b>4</b>	<b>Background Estimation</b>	<b>66</b>
4.1	Background Description . . . . .	66
4.2	QCD Background . . . . .	67
4.2.1	Electron Efficiency Determination . . . . .	68
4.2.2	Jet Efficiency Determination . . . . .	71
4.2.3	QCD Background Shape . . . . .	73
4.2.4	QCD Background Fit . . . . .	74
4.3	$Z \rightarrow ee$ Background . . . . .	76
4.4	$W \rightarrow \tau\nu$ Background . . . . .	78
<b>5</b>	<b><math>W</math> Width Measurement</b>	<b>79</b>
5.1	Monte Carlo . . . . .	79
5.1.1	$W$ Boson Generation . . . . .	80
5.1.2	$d\sigma/dm$ Calculation . . . . .	80
5.1.3	$d^2\sigma/dp_t dy$ Calculation . . . . .	84
5.1.4	$W$ Boson Decay . . . . .	88
5.1.5	QED Radiative Decays . . . . .	88
5.1.6	Simulation of $W \rightarrow \tau\nu \rightarrow e\nu\nu$ . . . . .	89
5.1.7	Detector Simulations . . . . .	90
5.1.8	Comparison of MC and Data . . . . .	92
5.2	Determination of the $W$ Boson Width . . . . .	93
5.2.1	Log-likelihood . . . . .	94
5.2.2	Fitting . . . . .	96
5.3	Systematic Uncertainties . . . . .	100
5.4	Consistency Check of the Result . . . . .	104



5.4.1	Number of Events Ratio . . . . .	104
5.4.2	Pt(W) Cut . . . . .	106
5.4.3	Non-linearity of the Calorimeter . . . . .	108
5.4.4	Ensemble Study for Background . . . . .	110
5.4.5	Upper Limit of Fitting Region . . . . .	110
5.4.6	Different Bin Size . . . . .	111
5.4.7	Statistical Error Checks . . . . .	111
5.5	Prospective for Run II . . . . .	112
5.6	Conclusion . . . . .	113

# List of Tables

1.1	Previous measurements of the $W$ decay width and the current world average, compared to the Standard Model prediction. The quoted results are followed by the statistical uncertainties and the systematic uncertainties. The * indicates the direct method used in the Large-Electron-Positron collider experiments (L3, OPAL, DELPHI and ALEPH), which is different from the one by the CDF experiment at a hadron collider. Detailed descriptions will be given in the section on $W$ width measurement. . . . .	4
1.2	The elementary particles of the Standard Model. The Higgs has not been found yet and is not listed. . . . .	7
4.1	Number of $Z \rightarrow ee$ events for tight and loose samples. . . . .	70
4.2	Jet efficiency in different ranges of $\cancel{E}_T$ . . . . .	72
4.3	QCD background fitting parameters and their uncertainties. . . . .	76
5.1	Patron luminosity slope $\beta$ in the $W$ production model. . . . .	84
5.2	The maximum likelihood fitting results of $W$ decay widths for different fitting regions and their statistical uncertainties. The chi-square and Kolmogorov-Smirnov(KS) are also listed. . . . .	97
5.3	The uncertainty due to PDFs. The uncertainty listed is the difference between the fitting width with a specific PDF as input for CMS when generating MC data and the width for the main template. The $\delta\Gamma$ in the last column is the maximum of the differences. . . . .	101

5.4	QCD background uncertainties due to fitting parameters in different fitting regions. The uncertainties listed are taken to be the difference between the fitting $W$ width when a specific parameter is taken at its up or low limit and the mean value when the parameter is taken at its mean value. The total $\delta\Gamma$ error is the quadratic summation of all the four individual errors. . . . .	102
5.5	The systematic uncertainties and total uncertainty on the $W$ width measurement for the different fitting regions. The unit of errors is in $MeV$ . . . . .	103
5.6	Consistency check for various $p_t(W)$ cuts. The $p_t(W)$ cut is changed by 3 GeV. The numbers in parenthesis of the first four rows are percentages compared to a $p_t(W)$ cut of 15 GeV. For the last three rows, the numbers in parenthesis mean the difference starting from the least significant digit compared to $p_t(W) < 15 GeV$ . The ratio, ratio fitting results and likelihood fitting results are all within their uncertainties. . . . .	107
5.7	The fitting width change due to non-linearity term of calorimetry. Units are in $MeV$ . The non-linear term of the calorimeter is added to electron energy, either in electron energy calibration when $W$ events are selected or in CMS MC simulation. The fitting results are compared to the normal fitting results without the non-linear term. . . . .	109
5.8	The effect of change of fitting region upper limit, compared to our standard fitting region. . . . .	111

# List of Figures

1.1	Quark and lepton doublets. . . . .	6
1.2	Dominant $W$ boson production process in $p\bar{p}$ collider. . . . .	16
1.3	Transverse mass spectra from Monte Carlo $W \rightarrow e\nu$ samples with different $W$ widths in logarithm scale. The squares show the spectrum for $\Gamma_W = 1.60 \text{ GeV}$ , the up triangles for $\Gamma_W = 2.10 \text{ GeV}$ and down triangles for $\Gamma_W = 2.60 \text{ GeV}$ . All MC data have been normalized to an arbitrary unit. . . . .	20
2.1	Fermilab Tevatron Collider complex. . . . .	23
2.2	Overview of the DØdetector. . . . .	27
2.3	Side view of the central tracking system. . . . .	28
2.4	The Transition Radiation Detector. . . . .	30
2.5	Cross sectional view of the CDC. . . . .	31
2.6	Layout of the FDC. . . . .	32
2.7	The DØcalorimeter. . . . .	33
2.8	One-quarter $\eta$ -view of the calorimeter and the Central detector. . .	35
2.9	Two unit cells of the DØcalorimeter. . . . .	36
2.10	Side view of the muon system. . . . .	41
2.11	DØ trigger and data acquisition system. . . . .	42
3.1	Electromagnetic energy fraction $f_{em}$ distributions for $Z \rightarrow ee$ candidates (solid) and electrons in multi-jet triggered data (dashed) (Central Electrons). . . . .	49

3.2	$\chi_{hm}^2$ distributions for test beam electrons (unshaded), test beam pions (shaded), and electrons from $W \rightarrow e\nu$ events (dots). . . . .	51
3.3	H-matrix $\chi_{hm}^2$ distributions for electrons from $Z \rightarrow ee$ candidates (solid) and electrons in multi-jet triggered data (dashed) (Central electrons). . . . .	52
3.4	Isolation distribution $f_{iso}$ for electrons from $Z \rightarrow ee$ candidates(solid) and electrons in multi-jet triggered data (dashed) (Central electrons). . . . .	53
3.5	Definition of the track match significance in terms of the cluster centroid in EM3 and the projection of the track to that radius. . .	54
3.6	Track match significance distribution $S_{trk}$ for electrons from $Z \rightarrow ee$ candidates(solid) and electrons in multi-jet triggered data (dashed) (Central electrons). . . . .	55
3.7	Transverse mass distribution of the $W$ candidates on logarithmic scale. The bin size is 5 GeV. The total number of events is 24485, while 24479 events are in the region 0-200 GeV . (There are 24483 events in 0-250 GeV) . . . . .	61
3.8	Invariant mass distribution of $Z \rightarrow e^+e^-$ event. Both electron are required to be in the CC region. . . . .	63
3.9	$W$ Boson candidate, end view. . . . .	64
3.10	$W$ Boson candidate. . . . .	65
4.1	$Z$ invariant mass for loose (left) and tight (right) electrons. The signal region and the two side-bands are hatched. . . . .	70
4.2	QCD background shape as a function of the transverse mass. . . .	73

4.3	In the first plot, QCD background is fit in the high end $m_t(W) > 80 \text{ GeV}$ with function $f = \exp(a_0 + a_1 * x + a_2 * x^2 + a_3 * x^3)$ . The fit background is taken to be the area under the fitting curve. The second plot show $(\text{background}(\text{original}) - \text{background}(\text{fit}))/\text{error}$ , where error is taken to be the square root of $\text{background}(\text{fit})$ . . . . .	75
4.4	The $Z \rightarrow ee$ background distribution as a function of the transverse mass. . . . .	77
4.5	Electron $E_T$ spectrum for $W \rightarrow \tau\nu \rightarrow e\nu\nu$ events (from CMS). . .	78
5.1	The unsmeared $W$ mass distribution for different PDFs and $\beta$ 's. For different PDFs of CTEQ4M [77] and MRSA with the same $\beta$ (solid line and black square), the spectrum is nearly identical. However, for the same PDF of CTEQ4M (solid line and dashed line) with different $\beta$ 's, $W$ mass distributions have an obvious difference, especially in the low mass region and high mass tail. . . . .	82
5.2	The transverse mass distribution for different PDFs and $\beta$ values. In the low end of the spectrum, all distributions are close. The difference appears in the high end. For different PDFs of CTEQ4M and MRSA with the same $\beta$ (solid line and black square), the spectrum is nearly identical. But for the same PDF of CTEQ4M (solid line and dashed line), the difference in $\beta$ causes the obvious different distributions. . . . .	83

5.3	The luminosity fitting for MRSA. The $W$ mass spectrum is generated by applying lepton fiducial cuts to the data made by RESBOS. The fitting function is Breit-Wigner skewed by $e^{-\beta*mass}/mass$ . The fitting parameters are normalization factor(p1), beta(p2) and $W$ mass(p3). The fitted $W$ mass is 80.374, which is a good check for this fitting. The chi-square is 0.3955 for 148 degrees of freedom. The fitting region is 72 GeV to 110 GeV. The result is $\beta = 0.00852 \pm 0.00012$ . The second plot shows the (data-fit)/sqrt(fit) in each bin. . . . .	85
5.4	The luminosity slope fitting for CTEQ4M. The method and procedure is the same as that for MRSA. The chi-square is 0.3955 for 148 degrees of freedom. The fitting region is 72 GeV to 110 GeV. The fitting result is $\beta = 0.00852 \pm 0.00013$ . The second plot shows the (data-fit)/sqrt(fit) in each bin. . . . .	86
5.5	Lowest order (Drell-Yan) diagrams for $W$ production. . . . .	87
5.6	Higher order diagrams for $W$ production: (left) the initial state gluon radiation process and the (right) Compton process. . . . .	88
5.7	Leading order diagrams for $W \rightarrow e\nu$ decays. . . . .	89
5.8	Invariant dielectron mass distribution of $Z \rightarrow ee$ MC simulation events. The $M_{Zee}$ is obtained by fitting the histogram with the sum of a Breit-Wigner convoluted with a Gaussian and a linear background contribution. The histogram is the MC sample. The curve is the fitting. . . . .	91
5.9	Invariant dielectron mass of $Z \rightarrow ee$ as a function of input $\alpha_{EM}$ . The black dots are data that was determined by fitting the MC sample. The line is the fitted with slope=90.986 and offset=0.57154. . . . .	92

5.10	Comparison of invariant dielectron mass of $Z \rightarrow ee$ , its fitting and MC simulation. The histogram is $Z \rightarrow ee$ from data. The curve is the fitting. The black square with error bar on it is the MC simulation with $\alpha_{EM} = 0.9545$ . They are normalized to the number of events in the data. . . . .	93
5.11	The comparison of data to CMS. The left column is the data overlap with CMS MC for electron Et, missing Et and $W$ pt. The solid line is for the data and the black square is for the MC sample. The CMS MC samples are generated with $\Gamma(W) = 2.050 \text{ GeV}$ and normalized to the number of events in the data. There is no background added to the MC sample. The right column is (data-MC)/error in each bin, where error is taken to be $\sqrt{\text{MC}} + \sqrt{\text{data}}$ in each bin. .	94
5.12	The comparison of data to CMS. Everything is the same as the previous plots, except the data events and MC sample are only these events with $m_T > 90 \text{ GeV}$ . . . . .	95
5.13	Results of the log-likelihood fit of the data to Monte Carlo templates. Monte Carlo templates are generated with values of $\Gamma(W)$ between 1.55 and 2.75 GeV at 50 MeV intervals. Each point represents a log-likelihood fit performed over the range $90 \text{ GeV} < m_t < 200 \text{ GeV}$ . The curve is the best fit of the likelihood points to a fourth order polynomial. The best fitting value is $\Gamma(W) = 2.231 \text{ GeV}$ . The uncertainty is statistical only. . . . .	98
5.14	Comparison of data to Monte Carlo templates. The solid line of the histogram is data. Black squares with error bars are the MC plus background. Monte Carlo templates are generated with $\Gamma(W) = 2.231 \text{ GeV}$ and normalized to the data with background subtracted. The dashed line is the background. . . . .	99



5.15 The ratio vs. $W$ decay width. The dots are the ratio from MC for different $W$ decay widths. It is fit with a straight line. The horizontal solid line represents the ratio from data. The two horizontal dashed lines show the uncertainties. . . . .	105
--	-----

## Abstract of the Dissertation

### Direct Measurement of $W$ Boson Decay Width at DØ

by

Qichun Xu

Doctor of Philosophy

in Physics

The University of Michigan

September 2001

This thesis presents the first direct measurement of the  $W$  boson decay width,  $\Gamma_W$ , with the  $W$  decay into an electron and neutrino final state using data collected by the DØ detector at the Tevatron collider. This analysis has used the  $W$  event sample collected in the Run I physics program. Backgrounds that contaminate the  $W$  sample are estimated using additional DØ data samples. Detailed Monte Carlo samples are used to template the transverse mass spectrum of the  $W$  events to extract the  $W$  decay width. Various sources of the systematic uncertainties of this measurement are investigated. The direct measurement result obtained in this thesis work is  $\Gamma(W) = 2.231_{-0.138}^{+0.145}(stat) \pm 0.092(sys) GeV$ . This result is consistent with the prediction of the Standard Model and the result from the indirect measurement from the DØ experiment.

# Chapter 1

## The Standard Model and the $W$ Decay Width

The two most fundamental questions that physicist have been trying to answer are what the building blocks of our universe are and what forces hold them together. The most successful theory of our current understanding is called the Standard Model (SM).

### 1.1 Introduction

The  $W$  boson plays an important role in the development of the electroweak theory. Before the foundation of the Standard Model (SM), which describes the fundamental particles and their interactions, was established, it was known that the Fermi effective V-A theory [1] about weak interactions is badly divergent at high energies. The theoretical calculation of the total cross section for the electron and neutrino scattering process explodes with increasing center-of-mass energy. Therefore, there must exist a massive boson as the weak force carrier to cancel the divergence in

theory to represent the real physics. By introducing the intermediate vector boson  $W^\pm$ , a propagator term is naturally added in the calculation, and thus the weak interaction cross section could converge at high energies. Unlike a massless photon which makes the electromagnetic force stronger than the weak force, the  $W$  must be massive to limit the weak interaction in a finite region. Based on the known Fermi Constant measured in weak interactions,  $G_f = 1.16639 \times 10^{-5} GeV^{-2}$ , the  $W$  boson mass was estimated to be at an order of 100  $GeV$ .

Hinted by the above considerations, a remarkable advance in particle physics in the last 3 decades is the establishment of the electroweak theory, which successfully introduced massive gauge bosons,  $W^\pm$  and  $Z^0$ , to the gauge theory to describe the weak interactions and to unify the electromagnetic interactions with the weak interactions.

The discovery of the  $W^\pm$  bosons in 1983 at the UA1 and the UA2 experiments at the CERN  $p\bar{p}$  collider [2, 3], along with the  $Z^0$  boson discovery also at the CERN  $p\bar{p}$  collider [4, 5], opened new windows for further detailed studies of the elementary particles and their interactions. The discoveries provided a direct confirmation of the unification of the weak and the electromagnetic interactions. Today, the effective theory that explains the fundamental particle interactions is called the Standard Model. It comprises of two theories: electroweak theory [6, 7, 8] of the weak and the electromagnetic interactions and Quantum Chromodynamics (QCD) [9, 10, 11], which describes the strong interactions. Both the electroweak and QCD theories are gauge theories based on symmetry groups  $SU(2) \times U(1)$  and  $SU(3)$ , respectively. In a gauge theory, the interactions are naturally introduced through the requirement of symmetry invariance. The force-carrying particles (gauge bosons) correspond to the generators of the gauge symmetry group, and the allowed set of couplings (the strength of the interactions) between particles is fixed by the requirement that the Lagrangian function (the frame work of the theory) be locally invariant under the symmetry transformations.

The  $W$  bosons, the weak interaction force carriers, have a very short life time. Its decay width,  $\Gamma_W$ , is a derived quantity in the Standard Model.  $\Gamma_W$  is very well predicted in terms of the masses and the couplings of the gauge bosons. The experimental measurement of the  $W$  decay width is motivated to test the Standard Model and to search for possible new physics beyond the Standard Model.

There are two methods, *direct* and *indirect*, to measure the  $W$  decay width experimentally. These two methods will be discussed in detail in the later section of this chapter. To date, the world average result of the  $W$  decay width measurement is  $2.12 \pm 0.05 \text{ GeV}$  [12]. This result includes measurement using both methods from major high energy experiments around the world. The individual experiment results are given in Table 1.1

This thesis work is the first measurement at the DØ experiment using the direct method to determine the  $W$  decay width from selected  $W$  event sample from the RUN I data.

The outline of this thesis is as following. The first chapter presents the theory which this measurement is based upon. The experimental measurement strategy is also described in this chapter. Chapter 2 gives the detailed information about the experiment apparatus, including the accelerator, the detector and the trigger system for data taking. Chapter 3 describes the DØ offline physics event reconstructions and the  $W$  data sample selection. Chapter 4 gives detailed estimation of various backgrounds contaminating the selected  $W$  event sample. Chapter 5 begins with the introduction of the Monte Carlo method, which is a very important technique used in this analysis, and follows with the measurement procedure and the results. The calculation of the systematic uncertainties is presented and the prospects and conclusion are given finally.

Experiment	Year	$\Gamma_W(GeV)$	# of Event	Method
UA1 [13]	1991	$2.18^{+0.26}_{-0.24} \pm 0.04$	-	Indirect
UA2 [14]	1992	$2.10^{+0.14}_{-0.13} \pm 0.09$	3559	Indirect
CDF [15]	2000	$2.05 \pm 0.10 \pm 0.08$	662	Direct
CDF [16]	1995	$2.064 \pm 0.060 \pm 0.059$	-	Indirect
D0 [17]	2000	$2.152 \pm 0.066$	79176	Indirect
L3 [18]	1999	$1.97 \pm 0.34 \pm 0.17$	687	Direct(*)
OPAL [19]	2001	$2.04 \pm 0.16 \pm 0.09$	2756	Direct(*)
DLPH [20]	1999	$2.48 \pm 0.40 \pm 0.10$	737	Direct(*)
ALEP [21]	2000	$2.24 \pm 0.20 \pm 0.13$	1711	Direct(*)
World Average	2000	$2.12 \pm 0.05$	-	-
SM prediction [12]	-	$2.0927 \pm 0.0025$	-	-

Table 1.1: Previous measurements of the  $W$  decay width and the current world average, compared to the Standard Model prediction. The quoted results are followed by the statistical uncertainties and the systematic uncertainties. The \* indicates the direct method used in the Large-Electron-Positron collider experiments (L3, OPAL, DELPHI and ALEPH), which is different from the one by the CDF experiment at a hadron collider. Detailed descriptions will be given in the section on  $W$  width measurement.

## 1.2 The Standard Model

The Standard Model of particle physics is so far the most successful theory about elementary particles and their interactions [22, 23]. Up to now, there is no confirmed experimental data that deviates from the Standard Model.

### 1.2.1 Elementary Particles in the SM

The theory that is referred as the Standard Model in particle physics includes the electroweak theory and Quantum Chromodynamics (QCD). The predictions of the Standard Model have been verified by experiments to high levels of precision. The electromagnetic force and the weak force have been successfully unified in the Standard Model. The strong interaction on the other hand has not been unified with the weak and electromagnetic interactions in the current framework of the theory.

Within the SM, a quantum field theory, the building blocks of our universe are a set of elementary particles. These particles are presented as fields in the quantum field theory. Two types of particles can be distinguished on the basis of their statistical properties: Fermions and bosons. Fermions are half-integer spin particles that obey the Pauli exclusion principle, which states that two particles with all quantum numbers identical cannot exist at the same quantum state. Bosons, on the other hand, are integer spin particles governed by Bose-Einstein statistics. Bosons can occupy the same quantum state.

The elementary particles can be divided into two classes: matter particles, fermions with spin  $1/2$ , and force carriers, gauge bosons with spin  $1$ . There are two types of fermions: quarks and leptons. They can each be formed into three families as isospin doublets (See figure 1.1). The up-like quarks ( $u, c, t$ ) all have fractional electric charge of  $2/3$ , while the down-like quarks ( $d, s, b$ ) have electric charge of  $-1/3$ . The three charged leptons ( $e, \mu, \tau$ ) have unit charge of  $-1$ , while

the neutrinos ( $\nu_e, \nu_\mu, \nu_\tau$ ) are electrically neutral. For each of the six quarks and the six leptons, there exists an antiparticle with electric charge negated.

$$\begin{pmatrix} u \\ d \end{pmatrix} \begin{pmatrix} c \\ s \end{pmatrix} \begin{pmatrix} t \\ b \end{pmatrix} \qquad \begin{pmatrix} e \\ \nu_e \end{pmatrix} \begin{pmatrix} \mu \\ \nu_\mu \end{pmatrix} \begin{pmatrix} \tau \\ \nu_\tau \end{pmatrix}$$

Figure 1.1: Quark and lepton doublets.

In addition to quarks and leptons, the Standard Model includes gauge bosons, the mediator particles of the various forces. In the case of the electroweak force, these are the electroweak force carrier gauge bosons: the massive  $W^\pm$  and  $Z^0$  bosons, and the massless photon ( $\gamma$ ). The QCD theory predicts eight spin-1 massless gluons as the strong force carrier. The Standard Model also predicts the existence of the Higgs boson (spin 0). Through the Higgs boson, a process called spontaneous symmetry breaking creates masses for all the massive particles. The Higgs boson is the only particle predicted by the Standard Model which has not yet been observed experimentally. It is interesting to notice that the introduction of the Higgs boson in the SM is necessary to cancel the  $WW$  scattering divergence at high energies in the calculation, which is analogous to the necessity of introducing the  $W$  boson in the calculation for the electron and neutrino scattering process. Table 1.2 [12] lists all the SM elementary particles and their properties.

In particle physics experiments, leptons and  $W, Z, \gamma$  can be observed directly or through their decay products in detectors. However, no free quarks and gluons have been observed. This phenomenon can be described by the QCD theory: quarks and gluons all carry a quantum number called color (the strong interaction charge). Each quark carries one of the three colors: green, red and blue. The associated anti-quark carries the color negated. Gluons are their own anti-particle and carry a color, anti-color pair. The color is a conserved quantum number in



Particle	Charge	Mass (GeV/c <sup>2</sup> )	Interactions
Leptons(spin 1/2)			
Electron (e)	-1	$5.11 \times 10^{-4}$	EM, Weak
Electron Neutrino( $\nu_e$ )	0	$< 5.1 \times 10^{-9}$	Weak
Muon ( $\mu$ )	-1	0.1057	EM, Weak
Muon Neutrino( $\nu_\mu$ )	0	$< 2.7 \times 10^{-4}$	Weak
Tau ( $\tau$ )	-1	1.771	EM, Weak
Tau Neutrino( $\nu_\tau$ )	0	$< 0.031$	Weak
Quarks(spin 1/2)			
Up( $u$ )	+2/3	$\approx 0.005$	EM, Weak, Strong
Down( $d$ )	-1/3	$\approx 0.010$	EM, Weak, Strong
Charm( $c$ )	2/3	$\approx 1.30$	EM, Weak, Strong
Strange( $s$ )	-1/3	$\approx 0.20$	EM, Weak, Strong
Top( $t$ )	2/3	$174.3 \pm 5.1$	EM, Weak, Strong
Bottom( $b$ )	-1/3	$\approx 4.3$	EM, Weak, Strong
Bosons(spin 1)			
Photon ( $\gamma$ )	0	0	EM
$W$ boson ( $W^\pm$ )	$\pm 1$	80.22	Weak (Charged)
$Z$ boson ( $Z^0$ )	0	91.187	Weak (Neutral Current)
Gluon ( $G$ )	0	0	Strong

Table 1.2: The elementary particles of the Standard Model. The Higgs has not been found yet and is not listed.

interaction, just like the electric charge is a conserved quantum number. QCD asserts all the free particles in nature are color-neutral. This can be achieved in two ways: (1) “red+green+blue” gives white (colorless) – in case of baryons, which are composited by three quarks; (2) a color and its anticolor also add up to white – in case of mesons, which are made of quark and anti-quark pairs. If a colored particle is emitted in an interaction, it immediately causes a spray of other particles to be created in order to shield its color. This process is called hadronization and the collimated spray of particles is called a hadronic jet that may be recorded in a detector.

### 1.2.2 Electroweak Theory

Electroweak interactions in the standard model are mediated by the  $\gamma$ ,  $W^\pm$  and  $Z^0$  bosons, which are quanta of gauge fields. For simplicity, we will describe the theory below beginning with the first generation of leptons. The generalization to the other generations should be straight forward. A more complete description of the standard model is given in Ref. [24, 25].

The frame work of the theory begins with the construction of a Lagrangian density function for a free (non-interacting), massless fermion field  $\psi(x)$ :

$$\mathcal{L} = \bar{\psi} i \gamma^\mu \partial_\mu \psi \quad (1.1)$$

where  $\mu$  is the space-time( $x^\mu$ ) index which runs from 0 to 3,  $\gamma^\mu$  are the  $4 \times 4$  Dirac matrices,  $\bar{\psi} \equiv \psi^\dagger \gamma^0$  and  $\partial_\mu = \partial/\partial x^\mu = (\partial_o, \nabla)$ .

Experimentally, no right handed neutrinos are observed ( i.e., neutrinos always have their spin pointing in the direction opposite to their momentum), so one writes the electron and neutrino fields as a left handed doublet and a right handed

singlet:

$$R_e = (e_R) \quad (1.2)$$

$$L_e = \begin{pmatrix} \nu_e \\ e_L \end{pmatrix} \quad (1.3)$$

where the left and right handed components of a field  $\psi$  are defined by

$$L_e \equiv \psi_L = P_L \psi = \frac{1 - \gamma^5}{2} \psi \quad (1.4)$$

$$R_e \equiv \psi_R = P_R \psi = \frac{1 + \gamma^5}{2} \psi \quad (1.5)$$

where  $\gamma^5$  is a matrix  $\begin{pmatrix} 0 & \underline{1} \\ \underline{1} & 0 \end{pmatrix}$  (in Dirac representation) and  $\underline{1}$  stands for the unit  $2 \times 2$  matrix.

The Lagrangian for free massless leptons is then

$$\mathcal{L} = \overline{L}_e i \gamma^\mu \partial_\mu L_e + \overline{R}_e i \gamma^\mu \partial_\mu R_e \quad (1.6)$$

The quantum numbers (internal degrees of freedom) are postulated: weak isospin  $T$  and hypercharge  $Y$ . The doublet has  $T = 1/2$  and the singlet  $T = 0$ . The upper component of the doublet has weak isospin  $T_3 = +1/2$  and the lower component has  $T_3 = -1/2$ . The hypercharge is given by the relation below

$$Q = T_3 + Y/2 \quad (1.7)$$

where  $Q$  is the electrical charge of the particle. The way particles behave under the electroweak symmetry group ( $SU(2)$ ) transformations is familiar because spin also transforms under a (different)  $SU(2)$  group. We know from quantum mechanics that particles with spin zero are singlets, particles with spin  $1/2$  ( $J = 1/2$ ) form doublet with  $J_3 = +1/2, -1/2$ , and so on. All known quarks and leptons are experimentally observed to be either electroweak singlets or doublets. The theory is required to be invariant under  $SU(2)$  phase transformations in the space describing the internal isospin degrees of freedom. Since  $T = 0$  for the singlet, the  $SU(2)$

group acts non-trivially only on the doublet. The Lagrangian must be invariant under  $SU(2)$  transformation of the form

$$L_e \rightarrow e^{i\vec{\alpha} \cdot \vec{\tau}/2} L_e \quad (1.8)$$

where  $\vec{\alpha}$  are the three parameters which specify the rotation and  $\vec{\tau}$  are the Pauli matrices, the generators of the isospin  $SU(2)$  group.

The fact that these matrices do not commute implies that the transformation is non-Abelian, which means that the order of transformation matters.

In a similar way, the theory is required to be invariant under  $U(1)$  transformations of the form  $\psi \rightarrow e^{i\alpha Y}$ , which implies:

$$L_e \rightarrow e^{-i\alpha} L_e \quad R_e \rightarrow e^{-2i\alpha} R_e \quad (1.9)$$

where  $\alpha$  specifies the transformation and hypercharge  $Y$  is the generator of the  $U(1)$  group. Electroweak singlets have  $Y = Y_R = -2$  while doublets have  $Y = Y_L = -1$ .

The requirement that gauge symmetries hold locally corresponds to allowing the coefficients  $\alpha$  and  $\vec{\alpha}$  to be functions of space-time. In order for the Lagrangian to remain invariant under local  $U(1)_Y$  transformation, one must introduce a gauge field  $B_\mu$  which transforms as a four-vector and replace the derivatives by gauge-covariant derivatives. Gauge invariance under local  $SU(2)$  transformation requires the introduction of three vector fields  $W_\mu^a$ ,  $a=1,2,3$ . The covariant derivative is thus introduced as:

$$D^\mu = \partial^\mu - ig_1 \frac{Y}{2} B_\mu - ig_2 \frac{\tau^a}{2} W_\mu^a \quad (1.10)$$

which has the property that  $D_\mu \psi$  transforms in the same way as  $\psi$  and  $g_1, g_2$  are coupling constants. If we define the field strength tensors

$$F^{\mu\nu} \equiv \partial_\mu B_\nu - \partial_\nu B_\mu \quad (1.11)$$

$$F_{\mu\nu}^a \equiv \partial_\mu W_\nu^a - \partial_\nu W_\mu^a + g_2 \epsilon^{abc} W_\mu^b W_\nu^c \quad (1.12)$$

where  $\epsilon^{abc} = +1(-1)$  if  $abc$  is a cyclic (anticyclic) permutation of 123 and  $\epsilon^{abc} = 0$  otherwise. By replacing  $\partial^\mu$  with  $D^\mu$  and adding the kinematic terms for the gauge fields, the electroweak Lagrangian is constructed as:

$$\mathcal{L} = \overline{L}_e i \gamma^\mu D_\mu L_e + \overline{R}_e i \gamma^\mu D_\mu R_e + \frac{1}{4} F_{\mu\nu} F^{\mu\nu} + \frac{1}{4} \vec{F}^{\mu\nu} \vec{F}_{\mu\nu} \quad (1.13)$$

which is invariant under the local  $U(1)_Y$  symmetry transformations:

$$L_e \rightarrow e^{-i\alpha} L_e \quad (1.14)$$

$$R_e \rightarrow e^{-2i\alpha} R_e \quad (1.15)$$

$$B_\mu \rightarrow B_\mu + \frac{2}{g_1} \partial_\mu \alpha(x) \quad (1.16)$$

$$(1.17)$$

and under the local  $SU(2)$  transformations:

$$L_e \rightarrow e^{i\vec{\alpha} \cdot \vec{\tau}/2} L_e \quad (1.18)$$

$$W_\mu^a \rightarrow W_\mu^a + \frac{1}{g_2} \partial_\mu \alpha^a(x) + \epsilon^{abc} \alpha^b W_\mu^c \quad (1.19)$$

This Lagrangian describes massless leptons interacting with four massless vector gauge fields. This can be generalized to the whole first generation fermions by adding two quarks, which are arranged in right handed singlets and a left handed doublet:

$$Q_L = \begin{pmatrix} u_L \\ d_L \end{pmatrix}, \quad u_R, \quad d_R \quad (1.20)$$

If one defines the gauge fields as

$$W^+ = (-W^1 + iW^2)/\sqrt{2} \quad (1.21)$$

$$W^- = (-W^1 - iW^2)/\sqrt{2} \quad (1.22)$$

$$W^0 = W^3 \quad (1.23)$$

and

$$\begin{aligned}
A_\mu &= \frac{g_2 B_\mu + g_1 W_\mu^0}{\sqrt{g_2^2 + g_1^2}} \\
Z_\mu &= \frac{-g_1 B_\mu + g_2 W_\mu^0}{\sqrt{g_2^2 + g_1^2}} \\
e &= \frac{g_1 g_2}{\sqrt{g_1^2 + g_2^2}} \\
\sin\theta_w &= s_w = \frac{g_1}{g_1^2 + g_2^2} \\
\cos\theta_w &= c_w = \frac{g_2}{g_1^2 + g_2^2}
\end{aligned} \tag{1.24}$$

after some straight-forward algebra and adding the quark terms, the electroweak interaction Lagrangian for the first generation becomes:

$$\begin{aligned}
\mathcal{L}_{SU(2) \times U(1)} &= \sum_{f=\nu_e, e, u, d} e Q_f (\bar{f} \gamma^\mu f) A_\mu \\
&+ \frac{g_1}{c_w} \sum_{f=\nu_e, e, u, d} [\bar{f}_L \gamma^\mu f_L (T_f^3 - Q_f s_w^2) + \bar{f}_R \gamma^\mu f_R (-Q_f s_w^2)] Z_\mu \\
&+ \frac{g_2}{\sqrt{2}} [(\bar{u}_L \gamma^\mu d_L + \bar{\nu}_e \gamma^\mu e_L) W_\mu^+ + h.c.]
\end{aligned} \tag{1.25}$$

where  $Q_f$  and  $T_f^3$  are the electromagnetic charge and third component of isospin, respectively, for each fermion  $f$ , and the h.c denotes the Hermitian conjugate. In Equation 1.25, the h.c of  $W^+$  is  $W^-$ . The fields  $A_\mu$ ,  $Z_\mu$ ,  $W_\mu^+$  and  $W_\mu^-$  are then identified as the photon ( $\gamma$ ), the  $Z^0$ , and the  $W^\pm$  fields, respectively. All fermions which have electric charge interact with the electromagnetic field  $A_\mu$ , regardless of their isospins, with a strength proportional to the charge. The neutrino which has  $Q_\nu = 0$  interact only with the  $Z^0$  and the  $W^\pm$  fields. Also, only left handed fermion interact with  $W^\pm$  fields. This is due to the fact that right handed fermions are  $SU(2)$  singlets with  $T = 0$ .

### 1.2.3 Higgs Mechanism

In above discussion, we have dealt with massless particles. In the Standard Model, the fermions and gauge bosons acquire mass through the *Higgs* mechanism. We introduce a doublet of complex scalar Higgs fields with  $T = 1/2$  and  $Y = 1$

$$\phi = \begin{pmatrix} \phi^+ \\ \phi^0 \end{pmatrix} = \begin{pmatrix} \frac{\phi_1 + i\phi_2}{\sqrt{2}} \\ \frac{\phi_3 + i\phi_4}{\sqrt{2}} \end{pmatrix} \quad (1.26)$$

and Higgs terms of the Lagrangian which arise from self interactions of the scalar field:

$$\mathcal{L}_H = (D_\mu \phi)^\dagger (D_\mu \phi) + \mu^2 \phi^\dagger \phi - \lambda (\phi^\dagger \phi)^2 \quad (1.27)$$

The potential  $\mu^2 \phi^\dagger \phi - \lambda (\phi^\dagger \phi)^2$  has a minimum at

$$|\phi^\dagger \phi| = \frac{\mu^2}{2\lambda} \equiv \frac{v}{\sqrt{2}} \quad (1.28)$$

Quantization must therefore start from a ground state, called the *vacuum*, which has a non-zero expectation value. This phenomenon is called spontaneous symmetry breaking: the Lagrangian exhibits a symmetry, but the behavior of the system is determined by the fluctuation of the field around a ground state which does not have the full symmetry of the Lagrangian, and the observable physical system will have a broken symmetry, meaning that the full symmetry of the Lagrangian will not be manifest. One usually makes the particular choice of the vacuum,  $\phi_0$ ,

$$\phi_0 = \begin{pmatrix} 0 \\ v/\sqrt{2} \end{pmatrix} \quad (1.29)$$

which corresponds to setting  $\phi_3 = v$  (the expectation of vacuum) and  $\phi_1 = \phi_2 = \phi_4 = 0$  (expression in Equation 1.26). The coupling of the Higgs field with the gauge bosons is then given by the covariant derivative term in Equation 1.27:

$$\phi^\dagger (ig_1 \frac{Y}{2} B_\mu + ig_2 \frac{\vec{\tau}}{2} \vec{W}_\mu)^\dagger (ig_1 \frac{Y}{2} B_\mu + ig_2 \frac{\vec{\tau}}{2} \vec{W}_\mu) \phi \quad (1.30)$$

Putting  $Y = 1$  and  $\phi = \phi_0$ , writing the Pauli matrices explicitly and using the definition for  $W_\mu^\pm$ ,  $A_\mu$  and  $Z_\mu$  gives, after some algebra, the following terms in the expression of the  $\mathcal{L}_H$ :

$$\frac{g_2^2 v^2}{8} (|W_\mu^+|^2 + |W_\mu^-|^2) + \frac{g_2^2 v^2}{8c_w^2} |Z_\mu|^2 \quad (1.31)$$

Since the expected mass term for a charged boson is  $m^2 |W_\mu|^2/2$ , we see that the  $W$  acquired mass  $M_W = vg_2/2$ . For the neutral vector fields the expected mass terms in the Lagrangian are  $M_Z^2 Z_\mu Z^\mu/2$  and  $M_\gamma^2 A_\mu A^\mu/2$ . Since there is no  $A_\mu A^\mu$  term, we see that the photon remains massless, while  $M_Z = vg_2/2c_w$ . Thus the standard model predicts the mass ratio  $M_W/M_Z = c_w$ , which has been verified experimentally.

The fermions also acquire mass by interacting with the Higgs field. For the leptons in the first generation, the Lagrangian term is given by

$$\mathcal{L}_{Yukawa} = -g_e (\bar{L}_e \phi R_e + \bar{R}_e \phi^\dagger L_e) \quad (1.32)$$

All fermions have similar terms. The coupling  $g_f$  is arbitrary and are called Yukawa coupling. Inserting the vacuum expression of  $\phi$  in Equ. 1.32, one can obtain the fermion masses as

$$m_f = \frac{g_f v}{\sqrt{2}} \quad (1.33)$$

So far, the Higgs boson has not been detected yet. It is a major task for the next generation collider experiments, such as ATLAS [27] at the Large Hadron Collider(LHC) at CERN, to find the Higgs boson.

#### 1.2.4 $W$ Decay Width

The  $W$  boson decay width,  $\Gamma(W)$ , is a derived quantity in the Standard Model and is very well predicted in terms of the masses and couplings of the gauge bosons.



At tree level, the matrix element for the  $W$  decay process,  $W \rightarrow e + \nu$ , is [22]:

$$\mathcal{M} = -i \frac{g_2}{\sqrt{2}} \epsilon_\mu \bar{e} \gamma^\mu \frac{1 - \gamma_5}{2} \nu \quad (1.34)$$

where  $\epsilon_\mu$  is the polarization function of the  $W$  and  $\bar{e}$ ,  $\nu$  represent the spinors wave functions for the electron and neutrino, respectively. Averaging  $|\mathcal{M}|^2$  over  $W$ -polarization, summing over final lepton spins and integrating over the available phase space, one obtains the partial decay width  $\Gamma(W \rightarrow e\nu) \equiv \Gamma_{e\nu} = g_2^2 M_W / 48\pi$  [12]. However, with radiative corrections, we need to rewrite it as

$$\Gamma_{e\nu} = \frac{G_F M_W^3}{6\sqrt{2}\pi} (1 + \delta_{\text{SM}}) \quad (1.35)$$

where we have used  $G_F/\sqrt{2} = g_2^2/8M_W^2$ . The SM radiative correction,  $\delta_{\text{SM}}$ , is calculated by Rosner *et al* [26] to be less than 0.5%. With experimental values of  $G_F$  (measured from muon decay) and  $W$  mass,  $M_W$  (measured at Tevatron and LEP), the predicted partial width is

$$\Gamma_{e\nu} = 226.5 \pm 0.3 \text{ MeV} \quad (1.36)$$

The uncertainty comes from the  $W$  mass measurement error. With three fermion families, the  $W$  boson has three leptonic decay channels and two hadronic decay channels. Including the QCD color factor and the radiation corrections, the electron-neutrino decay branching ratio,  $Br(W \rightarrow e\nu)$  is  $1/(3 + 6(1 + \alpha_s(M_W)/\pi + \mathcal{O}(\alpha_s^2)))$ . This leads to the SM prediction for the total decay width of the  $W$  boson:

$$\Gamma_W = 2.0927 \pm 0.0025 \text{ GeV} \quad (1.37)$$

## 1.3 $W$ Production and Decay

### 1.3.1 $W$ Production at Tevatron

Based on the Standard Model, in  $p\bar{p}$  collisions,  $W$ 's are produced mainly through three processes shown in Figure 1.2. At the Tevatron  $p\bar{p}$  collider with center-of-

mass energy  $\sqrt{s} = 1.8\text{TeV}$ , the total cross section for  $W$  production is about  $24\text{ nb}$ . Taking the decay branchings into consideration, the production cross section for the electron and neutrino final state can be determined as  $\sigma_W \cdot Br(W \rightarrow e + \nu_e) = 2.4\text{ nb}$ .

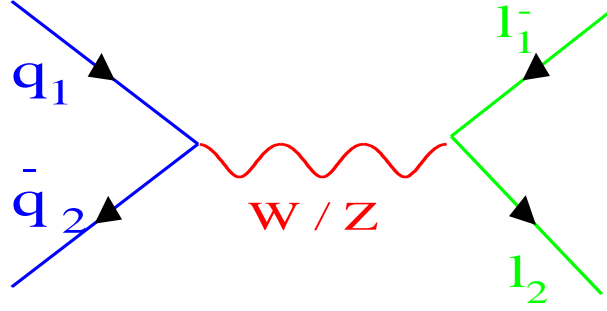


Figure 1.2: Dominant  $W$  boson production process in  $p\bar{p}$  collider.

### 1.3.2 Decay of the $W$ Boson

The decay of the  $W$  is predicted in the Standard Model, either leptonically or hadronically in the following processes with measured branching ratios:

$W \rightarrow e + \nu_e$  with branching ratio of  $10.9 \pm 0.4\%$

$W \rightarrow \mu + \nu_\mu$  with branching ratio of  $10.2 \pm 0.5\%$

$W \rightarrow \tau + \nu_\tau$  with branching ratio of  $11.3 \pm 0.8\%$

$W^\pm \rightarrow q'\bar{q}$  with branching ratio of  $67.8 \pm 1.0\%$

where  $q$  represents one of the quarks  $u, d, c$  or  $s$ . The decay of  $W$  to the third-generation quark doublet is kinematically suppressed because the top quark is considerably heavier than the  $W$ .

## 1.4 $W$ Width Measurement

### 1.4.1 Motivation

In the SM, the total  $W$  decay width is the sum of the partial widths of the leptonic decay over three generations and hadronic decay over two generations. The precision measurement of the  $W$  decay width could be a good test for the Standard Model. In addition, if additional non-standard model particles exist, which are lighter than the  $W$  and could couple to the  $W$ , there would be additional contributions to the total decay width. An example of this is the supersymmetry model where  $W$  can decay to the lightest superpartner of the charged gauge bosons and the lightest superpartner of the neutral gauge bosons, with a width that depends on the mass of the super-particles [28]. Thus, the  $W$  width is of interest as a test of the SM and also as a probe for possible new physics.

### 1.4.2 Indirect Measurement

Historically, the  $W$  width has been measured by UA1 [13], UA2 [14], CDF [16] and DØ [17] experiments using an indirect measurement method. The most recent results are  $\Gamma_W = 2.169 \pm 0.079 \text{ GeV}$  from DØ and  $\Gamma_W = 2.064 \pm 0.084 \text{ GeV}$  from CDF. They used the ratio  $\mathcal{R}$  of the process  $W \rightarrow e\nu$  and  $Z \rightarrow ee$  cross sections and decay branchings given by

$$\mathcal{R} = \frac{\sigma(p\bar{p} \rightarrow W + X) \cdot Br(W \rightarrow e\nu)}{\sigma(p\bar{p} \rightarrow Z + X) \cdot Br(Z \rightarrow ee)}$$

$$\begin{aligned}
&= \frac{\sigma_W}{\sigma_Z} \times \frac{\Gamma(W \rightarrow e\nu)}{\Gamma(Z \rightarrow ee)} \times \frac{\Gamma_Z}{\Gamma_W} \\
&= \frac{\sigma_W}{\sigma_Z} \times \frac{\Gamma_Z}{\Gamma(Z \rightarrow ee)} \times Br(W \rightarrow e\nu)
\end{aligned} \tag{1.38}$$

A measurement of  $\mathcal{R}$ , together with the theoretical calculations [29] of the production cross section ratio  $\sigma_W/\sigma_Z$  and partial decay width  $\Gamma(W \rightarrow e + \nu)$ , and the measurements of the branching ratio  $\Gamma(Z \rightarrow ee)/\Gamma(Z)$  at the CERN  $e^+e^-$  collider LEP [30], can determine the branching ratio,  $Br(W \rightarrow e\nu) = \Gamma(W \rightarrow e + \nu)/\Gamma(W)$ , which leads to the extraction of the full  $W$  decay width.

In the indirect measurement, calculations of  $\Gamma(W \rightarrow e + \nu)$  and  $\sigma_W/\sigma_Z$  are used to obtain the full  $W$  width. Thus, a measurement result of the  $\Gamma(W)$  extracted from  $\Gamma(W \rightarrow e + \nu)/\Gamma(W)$  assumes that the  $W$  boson coupling to the leptons is given by the standard model. To observe any non-SM couplings, a direct measurement of the full width  $\Gamma(W)$  is desirable, which does not depend on theoretical calculation. The radiative correction to the decay width could be also observed by the direct measurement.

### 1.4.3 Direct Measurement

This thesis describes the first direct measurement of the  $W$  boson decay width using the high mass tail of the transverse mass spectrum [31, 32, 33, 34], measured from the  $W \rightarrow e\nu$  decay channel with data collected by DØ detector.

In an  $e^+e^-$  collider experiment, such as L3, OPAL, DELPHI and ALEPH at LEP, the invariant mass spectrum can be reconstructed and fitting can be directly applied to extract the  $W$  decay width. In a hadron collider experiment, however, such as in DØ, we cannot fully reconstruct the energy and momentum of the neutrino due to the fact that protons and antiprotons are composite particles in the collision. Thus it is very difficult to reconstruct an invariant mass for  $W \rightarrow e\nu$  and directly determine the width  $\Gamma_W$  from the  $W$  mass distribution. The direct

measurement of  $\Gamma_W$  must rely on other physics quantities that are sensitive to the  $W$  decay width.

It has been proposed [35] that  $\Gamma_W$  can be extracted from the transverse mass spectrum. The  $W$  transverse mass is defined as

$$\begin{aligned} m_T &= \sqrt{2E_T^e E_T^\nu - 2\vec{p}_T^e \cdot \vec{p}_T^\nu} \\ &= \sqrt{2E_T^e E_T^\nu [1 - \cos(\phi_e - \phi_\nu)]} \end{aligned} \quad (1.39)$$

where  $E_T^e, E_T^\nu$  are the transverse energies,  $\vec{p}_T^e, \vec{p}_T^\nu$  are transverse momenta and  $\phi_e, \phi_\nu$  are azimuthal angles of the electron and the neutrino, respectively. The transverse mass exhibits a kinematical edge, as is in the  $W$  mass spectrum, but at the value of  $M_W$ . This edge is called the Jacobian edge. The value of the width  $\Gamma_W$  will change the shape of the  $m_T$  spectrum. This can be illustrated in Figure 1.3, which shows the Monte Carlo simulated  $W$   $m_T$  spectrum for different widths. From this plot we can see the sensitivity of the tail of the distribution to the values of width  $\Gamma_W$ , particularly in the region from 100 GeV to 200 GeV.

Since there is no analytic description for the lineshape of the transverse mass distribution in data, the determination of the  $m_T$  lineshape, which depends on  $\Gamma_W$ , relies on modeling the transverse mass spectrum through Monte Carlo simulations. The measured  $\Gamma_W$  is then extracted by comparing the  $m_T$  distribution of data with the Monte Carlo templates generated with different  $\Gamma_W$ . Obviously, the Monte Carlo simulation has to represent the real physics process in collision and the response of the detector. We have used the  $D\bar{O}$  data to calibrate the simulation parameters in the Monte Carlo program. Particularly, the  $Z \rightarrow ee$  events are extensively used for the calibration of the energy scales, energy resolutions, etc.

#### 1.4.4 Challenge of the Direct Measurement

The challenge of the direct measurement of the  $W$  width is that only the tail of the transverse mass spectrum is sensitive to  $\Gamma(W)$ , as already shown in Figure 1.3.

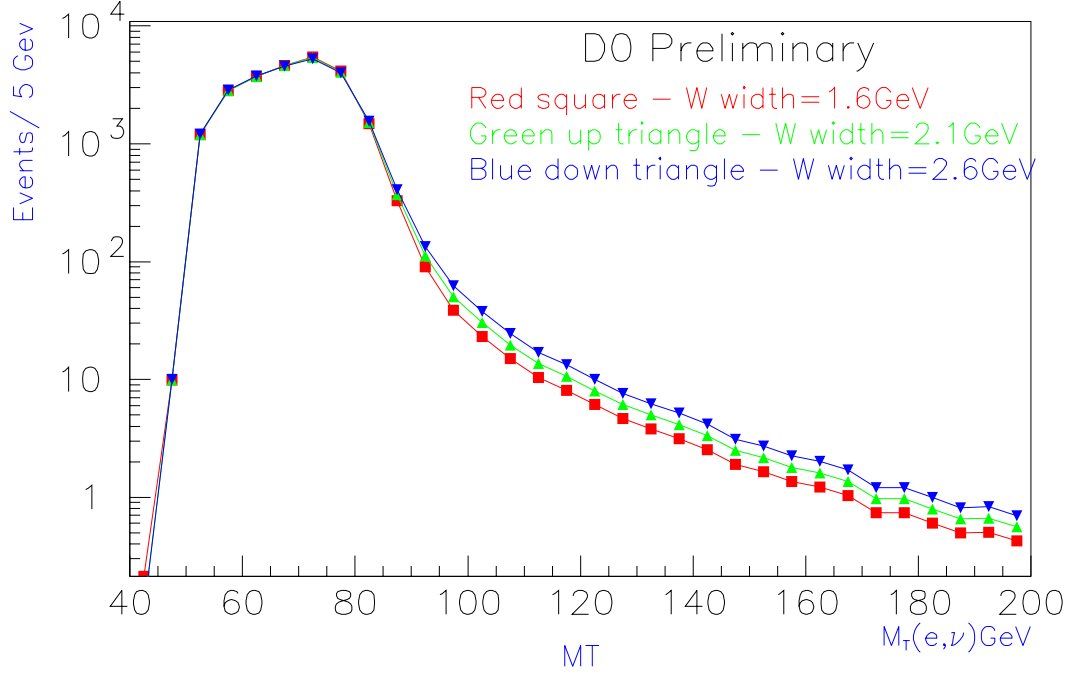


Figure 1.3: Transverse mass spectra from Monte Carlo  $W \rightarrow e\nu$  samples with different  $W$  widths in logarithm scale. The squares show the spectrum for  $\Gamma_W = 1.60 \text{ GeV}$ , the up triangles for  $\Gamma_W = 2.10 \text{ GeV}$  and down triangles for  $\Gamma_W = 2.60 \text{ GeV}$ . All MC data have been normalized to an arbitrary unit.

Due to the rapid decrease of events in the  $m_T$  tail, the available events for this analysis will be limited. It is important to notice that Figure 1.3 uses the logarithm scale. Only a very small fraction, about 1-2% of the total  $W \rightarrow e\nu$  events can be used for the fitting to determine the  $\Gamma_W$  value. This will give a large statistical uncertainty in the result.

Since the Monte Carlo templates are used to extract the  $W$  decay width, the uncertainties of every parameter in the Monte Carlo that could change the line-shape of transverse mass spectrum will cause systematic uncertainty. Most of these parameters are determined from the  $D\bar{O}$  data, thus they are limited by statistical and systematic uncertainties. The physics constants, such as the  $W$  mass and the  $Z$  mass, also include errors. These uncertainties will eventually lead to measurement error in the result of this measurement. The uncertainties of these parameters that are important to the lineshape of the transverse mass spectrum have to be studied very carefully.

## Chapter 2

# The DØ Experiment at Tevatron

The DØ experiment [36, 37] was designed to study a wide range of high-energy physics phenomena for proton-antiproton collisions at  $\sqrt{s}=1.8$  TeV in the Fermilab Tevatron Collider. The physics under investigation focused primarily on high mass and high- $p_T$  physics, which includes: top quark search,  $W$  and  $Z$  boson measurement, QCD, as well as new phenomena of non-Standard Model physics.

### 2.1 The Tevatron $p\bar{p}$ Collider at Fermilab

The Fermilab Tevatron [38], as shown in Figure 2.1, is presently the highest energy particle accelerator in the world, where protons and antiprotons collide head-on with a center-of-mass energy of 1.8 TeV. This makes its physics capabilities unique, as we can see in the discovery of the top quark in 1994 by both DØ [39] and CDF [40].

The Tevatron is actually referred to the last of a chain accelerators. These accelerators include:

- Preaccelerator



- Linac
- Booster
- Main Ring
- Antiproton Source
- Tevatron

All above accelerators are based on the same principle: when a charged particle traverses an electric field, the particle will accelerate in the direction parallel to the electric field lines. An actual accelerator consists of a series of gaps with electric fields coming from RF cavities. Electrically charged particles are accelerated along the gradients of the RF fields.

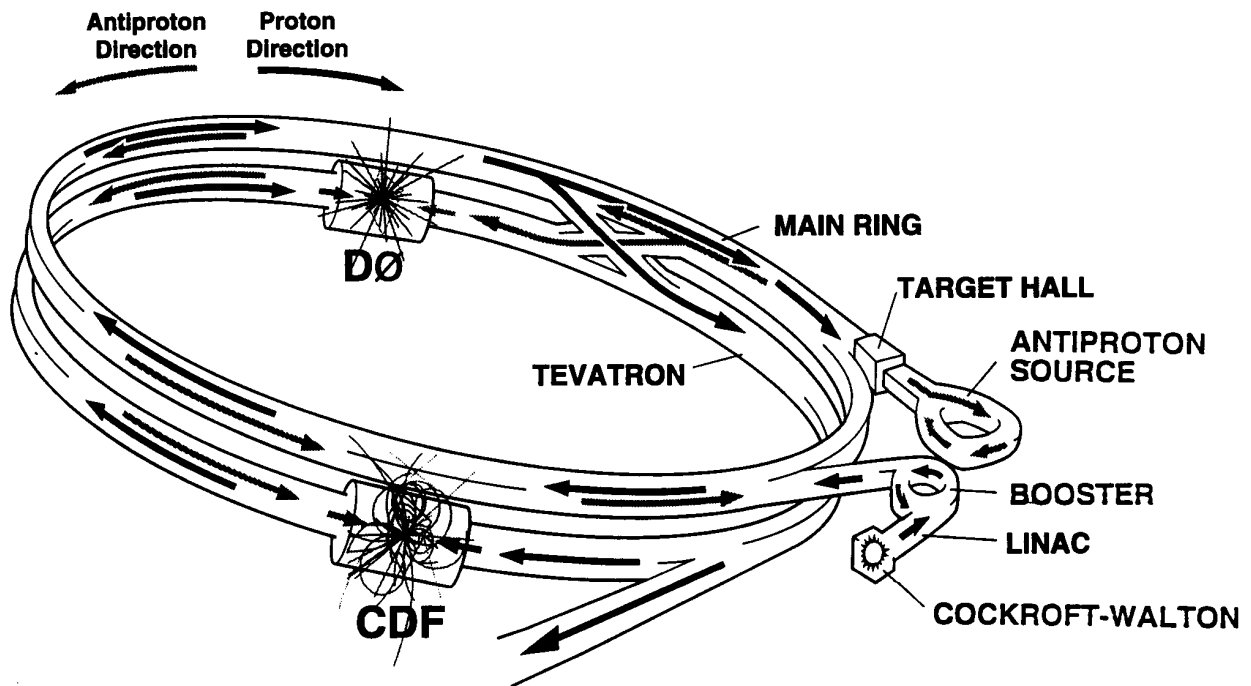


Figure 2.1: Fermilab Tevatron Collider complex.

There are two kinds of accelerators according to their geometric arrangements, linac and synchrotron. In a linear accelerator, the gaps are arranged in a straight line. While in a synchrotron, the gaps are situated along a circle. Compared to a linac, the advantage of a synchrotron is that it can keep the charged particles in orbit to accelerate by reusing the gaps as long as the desired energies are reached. On the other hand, the disadvantage is the requirement of very strong magnetic fields to bend the beam and the energy loss of the particles due to radiation, especially for light particles at very high energies.

In the Tevatron, the source of the proton beam comes from a pressurized hydrogen gas. The hydrogen atoms are ionized to form  $H^-$  ions, which are accelerated to an energy of 750 KeV by an electrostatic Cockcroft-Walton accelerator. The ions are then injected into the Linac, a 150 m long linear accelerator, which raises the ion energy to 400 MeV. Once the ions come out of the Linac, they are passed through a carbon foil to strip off the electrons. The resulting protons are steered into the Booster, which is a synchrotron with a diameter of 151 meters, and the proton energy are increased to 8 GeV. The next stage is the Main Ring, a 1 km radius synchrotron with about 1000 non-superconducting copper-coiled magnets. Within the the Main Ring, the protons are compressed into small bunches, with about  $2 \times 10^{12}$  protons per bunch. Some of the bunches are accelerated to 150 GeV and directly injected into Tevatron, while some other bunches are accelerated to 120 GeV and directed into the Antiproton Source.

When the 120 GeV proton bunches are dumped onto a nickel/copper target (in the Target Hall), antiprotons are produced at a rate of about 20 antiprotons per 1 million protons that are sent to the Target Hall. These antiproton have a wide range of angular and energy spread. They are focused with a Lithium lens and 8 GeV antiprotons are selected by a magnetic field. The antiprotons are then transported into a storage ring called the Debuncher, where antiproton are equalized in momentum and time spread. For every 2.4 seconds, the resulting

monochromatic  $\bar{p}$ -beam with about  $2 \times 10^6$  antiprotons per bunch is injected into a second storage ring, the Accumulator. When about  $4 \times 10^{11}$  are collected, which typically takes 8 - 12 hours, they are injected into the Main Ring and accelerated to 150 GeV and transported into the Tevatron in opposite direction of the protons.

The Tevatron is located in the same tunnel as the Main Ring at a distance of about 1m beneath it, except in the two interaction regions where the detector are located. The B0 intersection region is for the CDF detector and the DØ intersection region for the DØ detector. The Tevatron is a synchrotron with about 1000 super-conducting magnets operating at 4.6 K. These magnets can produce a magnetic field up to 3 Tesla, which allow the proton and antiproton beams to orbit in a circle of radius 1000 meters. In the final acceleration stage, six bunches of about  $10^{11}$  protons and six bunches of about  $5 \times 10^{10}$  antiprotons are ramped to 900 GeV at the same time and brought to collision in two places, at the CDF and the DØ detector. The proton and antiproton beams are kept apart everywhere else by electrostatic separators. Over time, the density of the  $p$ - and  $\bar{p}$ -bunches decreases as a result of collisions of the beam with residual pipe gas and the beam-beam effects that blow up the beam size. The beam have a typical life time of 12-18 hours, after which they have to be replaced. During the 1992-1993 run, the instantaneous luminosities, or the proton-antiproton flux, reached as high as  $10 \times 10^{30} cm^{-2} s^{-1}$ .

Generally, high-energy particles can collide in two different modes, either in fixed target mode or colliding beam mode. In fixed target mode, a beam is directed on a target to produce secondary particles whose energy and type can be varied, whereas in colliding beams mode, a proton and an antiproton beam are brought to collision. The advantage of the collider mode is that the center-of-mass energy is proportional to  $E$ , instead of  $\sqrt{E}$  as in fixed target mode. The disadvantage is that the luminosity of a collider is lower than that of a fixed target experiment using a beam of similar intensity.

## 2.2 Overview of the DØ Detector

The DØ detector [36, 37] is a large general purpose detector. It consists of three subsystems with distinct purposes, which is shown in Figure 2.2. These three subsystems are:

- Central Detector(CD)
  - Vertex Drift Chamber(VTX)
  - Transition Radiation Detector(TRD)
  - Central Drift Chamber(CDC)
  - Forward Drift Chambers(FDC)
- Liquid Argon Calorimeter
  - Central Calorimeter(CC)
  - End Calorimeter(EC)
  - Intercryostat Detectors(ICD)
- Muon Detector
  - Wide Angle Muon System(WAMUS)
  - Small Angle Muon System(SAMUS)

Each of these sub-detector has its purpose. The main purpose of the Central Detector is tracking particles created in proton-antiproton collisions, the Calorimeter measures the energy of the particle-jets, and the Muon system detects muons which escape the inner parts of the detector due to their long lifetime and high mass. A conceptual difference between the innermost tracking system and the calorimeter is that tracking should be as undestructive as possible. That means that the incoming particles should only lose a very small fraction of their energy in the tracking system.

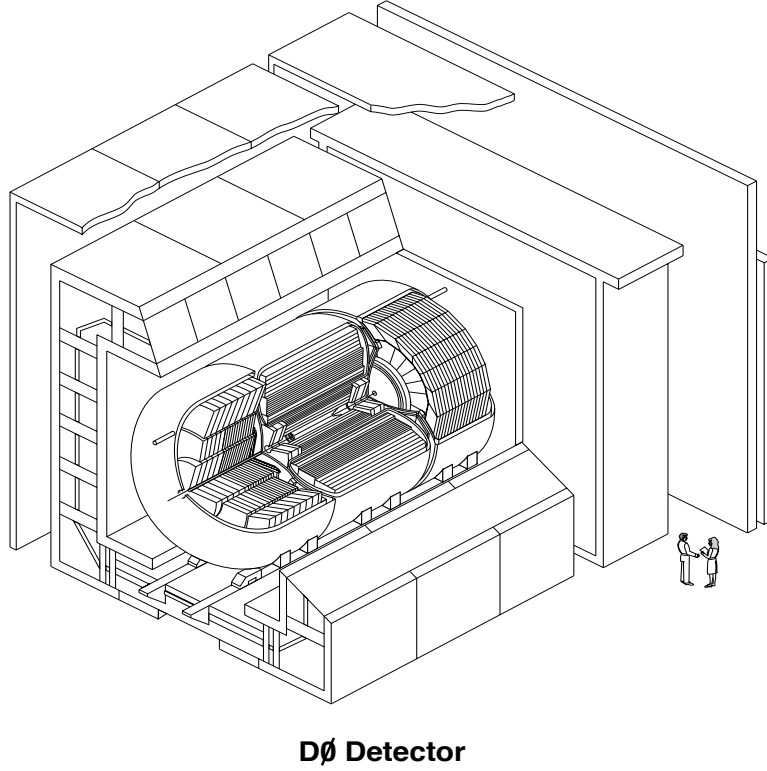


Figure 2.2: Overview of the DØ detector.

The following sections will describe in details each of the sub-detectors, with emphasis on those that are related to this analysis. More detailed descriptions of DØ can be found in reference [37].

## 2.3 The Central Detector

There are four major subsystems in the central detector [36, 37, 41]: the innermost vertex drift chamber (VTX) is surrounded by the transition radiation detector (TRD) used for electron identification which is followed by the cylindrical central drift chamber (CDC), as shown in Figure 2.3. Two disk shaped forward drift chambers (FDC) extend the forward coverage. The VTX, TRD and CDC have a cylindrical geometry and are arranged concentrically around the beam pipe. The FDCs are oriented perpendicular to the beam line. All central detectors are

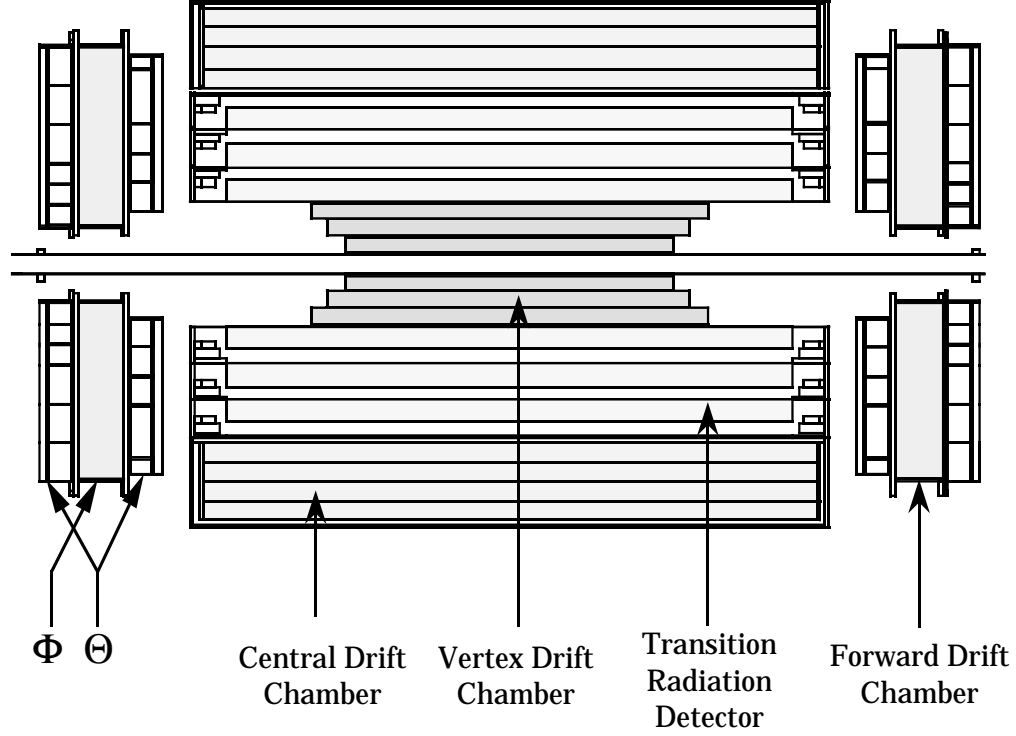


Figure 2.3: Side view of the central tracking system.

contained in a cylinder of 75 cm radius and 270 cm length.

The VTX, CDC and FDC are wire drift chambers, which are gas filled volumes with a strong electric field applied between a thin anode wire and a cathode. When a charged particle crosses the gas, it creates a track of electron-ion pairs along its trajectory. In the presence of an electric field, the electrons will drift towards the anode, while ions in opposite direction. Because of their large mass, they move comparatively very slowly and can be neglected. The small diameter of wire generates a very strong electric field in its vicinity, which accelerate the electrons to energies high enough to induce further ionization. In this manner, the number of electrons increases exponentially, which results in a cascade of electrons moving towards the anode and gives a measurable current. The difference between the known  $p\bar{p}$  collision time and the arrival time of the pulse at the wire is called the drift time, which is used to infer the drift distance.

### 2.3.1 The Vertex Chamber

The vertex chamber (VTX) [37] lies directly outside the beam pipe and is the first detector that particles pass through. Its primary use is to accurately determine event vertex positions. The VTX chamber consists of three concentric cylinders which occupy the region from 3.7 cm to 16.2 cm. The active length of the inner layer is 97 cm while the two outer successive layers are 10 and 20 cm longer, respectively. The innermost layer has 16 cells in azimuth, while the outer two layers each has 32 cells. Each cell contains eight sense wires, which are  $25\text{ }\mu\text{m}$  in diameter. The active medium (the gas ionized) is  $CO_2(95\%)-C_2H_6(5\%)$  with a small amount (0.5%) of water added. The water helps stabilize the detector against radiation damage. [42, 43]. The sense wires operate at an electrical potential of +2.5 keV. The average drift velocity is about  $7.3\mu\text{m ns}^{-1}$ . The vertex resolution of VTX is about  $60\text{ }\mu$  in  $r\phi$  and 1.5 cm in  $z$  [41].

### 2.3.2 The Transition Radiation Detector

The transition radiation detector (TRD) [37, 41] is located between the VTX and the CDC. It is used to provide independent electron identification to that of calorimeters. It is based on the fact that relativistic particles radiate when they cross the boundary between two media with different dielectric coefficients. The energy of the emitted X-rays increases with Lorenz  $\gamma$  and is hence inversely proportional to the mass of the incident particle. Consequently, the measurement of the energy of the X-rays produced can be used to distinguish electron from heavier particles such as pions.

The DØ TRD consists of three independent sections, each containing a radiator (layered polypropylene foil) and an X-ray detection chamber (a proportional wire chamber, PWC). A cross sectional view of the first layer of the TRD is shown in Figure 2.4. An incident particle produces X-rays in the radiator stack, which

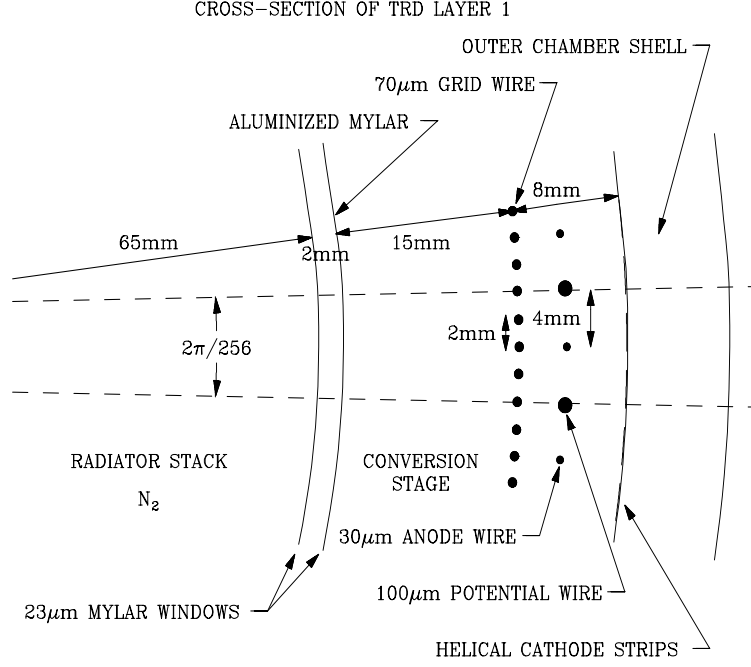


Figure 2.4: The Transition Radiation Detector.

is converted in the gas of the PWC and charge drifts radially outwards and is amplified before reaching the sense wires. The TRD provides an additional factor of about 50 [37] in rejection of isolated pions beyond that given by the calorimeter alone.

### 2.3.3 The Central Drift Chamber

The central drift chamber (CDC) [44] is located immediately outside the TRD and just inside the Central Calorimeter. It provides coverage for tracks at large angles. It is a cylindrical shell of 184 cm in length and with a active radius from 49.5 cm to 74.5 cm. This results in an  $\eta$  coverage up to 1.2. A plot of cross sectional view of the CDC is shown in Figure 2.5.

The CDC contains four concentric rings. Each ring has 32 azimuthal cells, with each cell housing seven 30  $\mu$ m gold-plated tungsten sense wires. The hit position in  $r - \phi$  is inferred from the coordinates of the hit wire and the drift time.



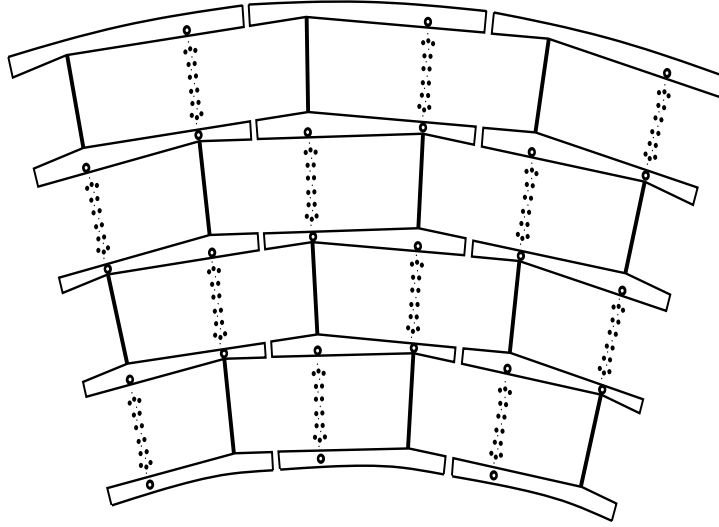


Figure 2.5: Cross sectional view of the CDC.

Two additional delay lines are included in each cell to provide  $z$ -information. The delay lines allow to determine  $z$ -position of the track by measuring the difference of arrival times at the two ends. The resolution achieved in the CDC is  $180 \mu\text{m}$  in  $r - \phi$  and  $2.9 \text{ mm}$  in  $z$ .

### 2.3.4 The Forward Drift Chambers

The Forward Drift Chambers (FDC) [45] provide the angular coverage to  $\theta \approx 5^\circ$  or  $\eta = 3.1$ . They are located on both ends of the VTX, TRD and CDC. Each of two FDC chambers is made of three separate modules: one  $\Phi$  chamber with axial sense wires for a  $\phi$  measurement and two  $\Theta$  chambers for  $\theta$ . See Figure 2.6 for their orientation. The two  $\Theta$ -chambers are rotated by  $45^\circ$  with respect to each other. The resolution achieved by the FDC is  $200 \mu\text{m}$  in  $\phi$  and  $300 \mu\text{m}$  in  $\theta$ .

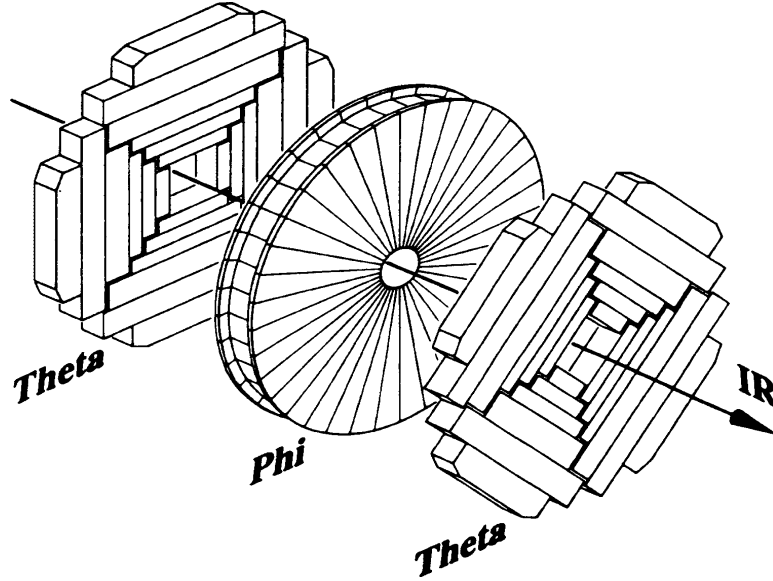


Figure 2.6: Layout of the FDC.

## 2.4 The Calorimeter

The design of the DØ detector places a very heavy emphasis on the calorimeter. It plays a vital role in the energy measurement and particle identification of electrons, muons, taus, photons, jets and neutrinos. The structure of the DØ calorimeter is depicted in Figure 2.7.

### 2.4.1 Overview of Calorimeter

In general, high energy electrons interact with high-Z material through Bremsstrahlung. High energy photons, on the other hand, can produce electron-positron pairs in the Coulomb-field of a nucleus which can in turn interact through Bremsstrahlung. Consequently, an electron or photon can produce a cascade of photons and electron-positron pairs until the energy of each of these particles is low enough for other energy loss processes such as ionization to become dominant. The amount of energy a electron or photon loses while traversing a certain material is characterized

## DØ LIQUID ARGON CALORIMETER

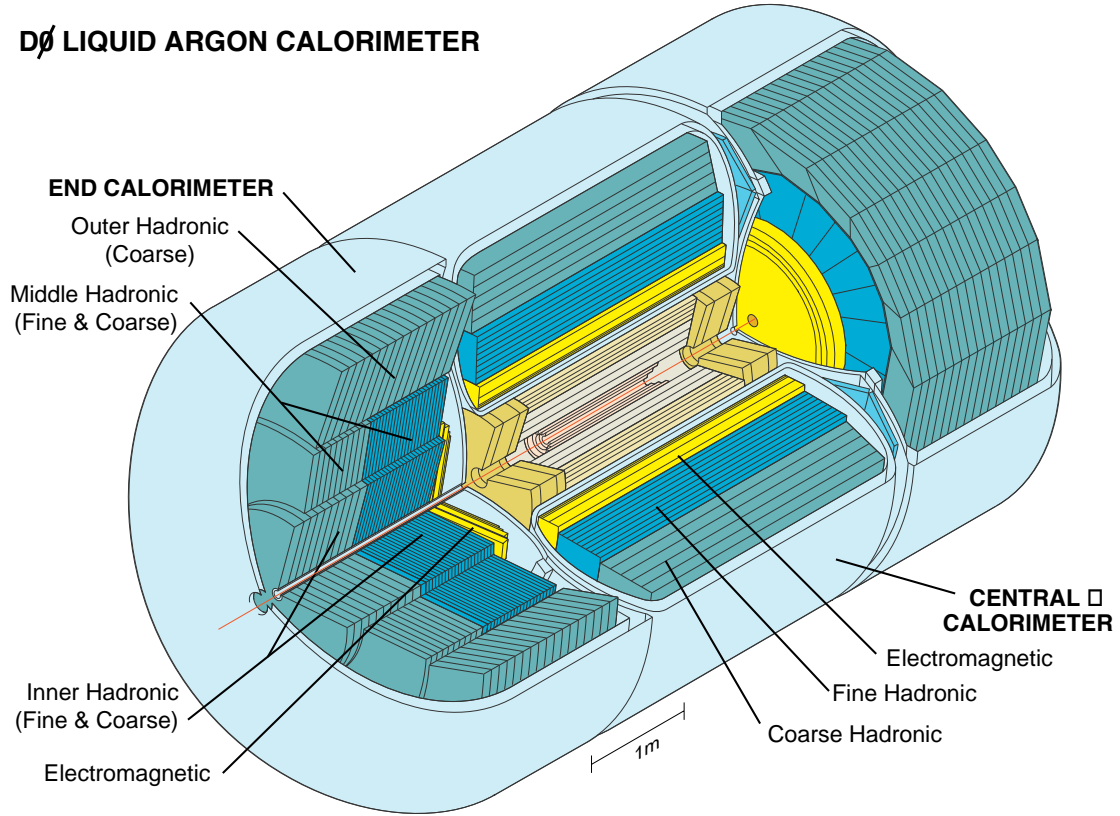


Figure 2.7: The DØ calorimeter.

by a material constant, the radiation length  $X_0$ , according to:

$$\frac{dE}{E} = -\frac{dx}{X_0} \quad (2.1)$$

The radiation length is defined as the mean distance at the end of which the energy of a particle decreases to  $1/e$  of its initial energy. Physically, the radiation length is the mean free path for emitting bremsstrahlung. For charged particles, the radiation length depends on the Compton wavelength of the particle. Since muons are about 200 times heavier than electrons, they don't suffer considerable Compton losses in the calorimeter. Electrons, on the other hand produce electromagnetic showers. This definition for radiation length applies to photons as well. For electrons, radiation length may be parameterized in terms of atomic mass ( $A$ )

and atomic number ( $Z$ ) [46]:

$$X_0 \approx 180 \frac{A}{Z^2} \quad (2.2)$$

For optimal energy resolution, it is desirable to use materials with small radiation length for the calorimeter, in which the particles lose a large fraction of their energy  $dE$  in a short path  $dx$ . For uranium, as used in the DØ detector, the radiation length  $X_0$  is 3.2 mm which is rather small, allowing for compact detector design.

The physical process for hadronic particles to interact with matter is quite different from the one just described above. Here the main energy loss process is through inelastic collisions with atomic nuclei. These collisions result in new hadrons which can then in turn scatter inelastically, resulting in hadronic showers. The size of these showers is characterized by the nuclear interaction length,  $\lambda$ , which is the mean free path between inelastic collisions. The  $\lambda$  is 10.5 cm for uranium, which is much larger than the electromagnetic radiation length. Hadronic showers are more extended in size than electromagnetic showers. While almost all electromagnetic showers will have lost their energy within the inner electromagnetic sections of the calorimeter, hadron showers typically extend into the outer, hadronic sections.

There are two different types of calorimeters: homogeneous calorimeters and sampling calorimeters. In a homogeneous calorimeter, the absorber material also functions as the active material. For example, a lead glass scintillator can trap a large fraction of the energy of the incoming particles and generate light pulses that can be read out through photomultipliers (PMTs). In a sampling calorimeter, on the other hand, layers of a dense inert material absorbing most of the energy are interleaved with layers of active material sensitive to radiation. The fraction of the incident energy that is actually detected in the active material is called the sampling fraction. In the DØ detector depleted uranium is used as the absorber

material with the advantage that its density allows for a compact calorimeter. Copper and stainless steel are used in addition in the outer regions. The ionization medium is liquid argon which requires cryogenic cooling of the calorimeter.

The resolution of a calorimeter is limited by the statistical nature of the energy loss processes in matter and scales like  $\frac{1}{\sqrt{N_{ion}}}$  where  $N_{ion}$  is the number of ions liberated. Since  $N_{ion}$  is proportional to the incident energy, one expects the resolution to be roughly proportional to  $\frac{1}{\sqrt{E}}$ . This ideal resolution gets further degraded by noise effects, instabilities in the run conditions of the detector like temperature fluctuations, natural radioactivity from the depleted uranium and energy leakage out of the calorimeter. For a good discussion on calorimetry in high energy physics see [47].

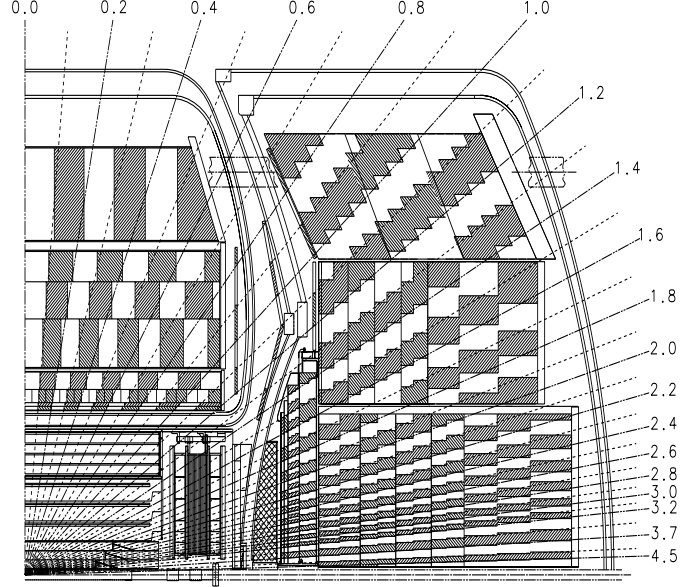


Figure 2.8: One-quarter  $\eta$ -view of the calorimeter and the Central detector.

The DØ calorimeter, as shown in Figure 2.7 and Figure 2.8 , consists of one Central Cryostat (CC), covering the region  $|\eta| \leq 1.2$ , two Endcap Cryostats (EC's)

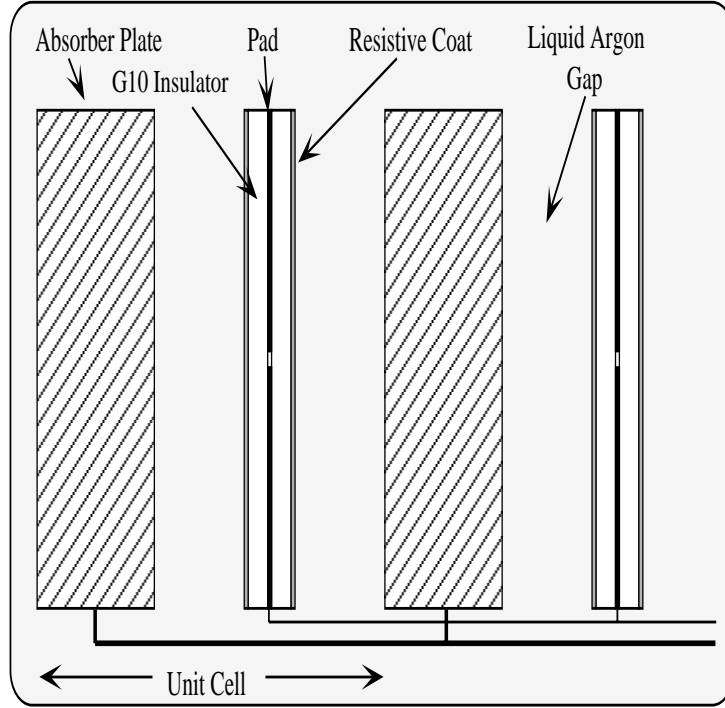


Figure 2.9: Two unit cells of the DØ calorimeter.

extending the coverage to  $|\eta| \approx 4$ , and the Inter-Cryostat Detector (ICD), covering the region between CC and EC modules. It is finely segmented in the transverse and longitudinal shower directions. The size and construction of the calorimeter cells varies between layers to account for the specifics of shower profiles. Each calorimeter cell consists of alternating absorber plates and signal readout boards as seen in Figure 2.9. The gap between absorber plate and pad is filled with liquid argon. The signal boards consist of a copper pad with two 0.5 mm thick G-10 sheets laminated on each side whose outer surfaces are coated with highly resistive epoxy. An electric field is established by grounding the absorber plates while applying 2 - 2.5 keV to the resistive epoxy surfaces. When an incoming particle hits an absorber plate, it showers into many particles ionizing the liquid argon in the adjacent gap. Liberated electrons drift to the signal board with typical drift times of around 450 ns, inducing a signal on the copper pad. Signals from several

signal boards in the same  $\eta - \phi$  region are grouped together to form a readout cell.

The overall pattern is pseudo-projective as shown in Figure 2.8: The centers of the calorimeter cells lie on lines that project back to the center of the detector, whereas the cell boundaries are perpendicular to the absorber plates.

### 2.4.2 Central Calorimeter

The Central Calorimeter (CC) includes three concentric cylindrical shells, corresponding to the EM, fine-hadronic(FH) and coarse-hadronic(CH) modules, from inside to out. They cover  $75 \text{ cm} \leq r \leq 222 \text{ cm}$  from the nominal beam axis. The angular coverage is  $35^\circ \leq \theta \leq 145^\circ$  which corresponds to  $|\eta| \leq 1.2$ . There are 32 EM modules thick enough to contain most electromagnetic showers. The middle shell consists of 16 FH modules to measure showers of hadronic particles while the outer shell, with 16 CH modules, measures any leakage out of the FH layer while minimizing punch through, the energy flow out of the calorimeter into the muon system.

There are 21 radial cells in each EM module and they are formed in 4 readout layers EM1-EM4. The size of each EM layer is  $\delta\eta \times \delta\phi = 0.1 \times 0.1$ , except for EM3 where it is reduced to  $0.05 \times 0.05$  to optimize the separation between electromagnetic and hadronic showers in the layer where most EM showers deposit the bulk of their energy. The total radiation length is 20.5. Each cell contains a 3 mm depleted uranium absorber plate, a 2.3 mm liquid argon gap and a signal board as described above, leading to a sampling fraction of 12.9 %.

Each cell in the FH module has a 6 mm uranium-niobium alloy(Niobium is added for better mechanical strength)(U-Nb) absorber plate, a 2.3 mm liquid argon gap, and a signal board as described above, which amounts to a sampling fraction of 6.9 %. The total radiation length is 96.0. The transverse segmentation is  $0.1 \times 0.1$  in  $\eta \times \phi$ .

A sampling fraction of 1.7 % is achieved in CH cell by using 4.75 cm thick copper absorber plates with 2.3 mm liquid argon gaps. The transverse segmentation is the same as in FH. The total radiation length is 32.9.

### 2.4.3 Endcap Calorimeter

The Endcap Calorimeters (EC's) cover the forward regions  $2^\circ \leq \theta \leq 30^\circ$  and  $150^\circ \leq \theta \leq 178^\circ$  ( $1.3 \leq |\eta| \leq 4$ ). Each EC cryostat is divided into four sections, Electromagnetic (EM), Inner Hadronic (IH), Middle Hadronic (MH), and Outer Hadronic (OH). The details are shown in Figure 2.7). This analysis will not use the data from the EC. Detailed information can be found in reference [36, 37, 41].

### 2.4.4 Intercryostat Detectors and Massless Gaps

In the region  $0.8 < |\eta| < 1.4$ , there are a large amount of un-instrumented material, see Figure 2.8. This consists of cryostat walls, stiff rings and modules endplates. To correct for the energy loss in this dead material, two additional detectors have been installed. The massless gap detector (MG) is an additional layer of liquid argon sampling on the face of each MH and OH module in the EC and each end of the FH modules in the CC. The massless gaps present no significant absorber material but they sample the shower energy before and after the dead material between cryostats which means they measure the energy lost therein. The second type of compensating detector is the Intercryostat detector (ICD). It consists of two arrays of 384 scintillation counter tiles mounted on the front surface of each EC cryostat. The size of the tiles is matched to that of the liquid argon calorimeter cells. Grooves cut into each scintillating tile guide wavelength-shifting optic fibers that channel the scintillation photons to photomultiplier tubes (PMT's) for readout. The tile arrays cover the entire rapidity range from 0.8 to 1.4.



### 2.4.5 Calorimeter Calibration

The readout of the calorimeter signals is done in three steps: the 450 ns wide pulses are routed through four ports in the cryostats to charge sensitive preamplifiers. Subsequently the pulses are input to baseline subtractor modules (BLS) which perform analog signal shaping and splitting of the signal into two. The first signal serves as input to the calorimeter Level-1 trigger and the second one is used for data readout. Sampling occurs just before each beam crossing and  $2.2\mu\text{s}$  later so that the difference between the two readings is a dc voltage that is proportional to the collected charge. Finally, if an event is accepted by the Level-1 trigger, the difference is sent to analog-to-digital converters (ADC's) that digitize and zero-suppress the signals before being sent to the Level-2 trigger.

To utilize the DØ calorimeter to its fullest potential it was necessary to study its performance extensively so that measured pulses read out by the calorimeter electronics can be related to physical energies. Two kinds of studies that complement each other were done: test-beam studies [37] and cosmic ray muons studies [48]. The calorimeter response was found to be linear up to 0.5% in the energy range from 10 GeV to 150 GeV. The energy resolution of a calorimeter can be parameterized as:

$$\frac{\delta E}{E} = C \oplus \frac{S}{\sqrt{E}} \oplus \frac{N}{E} \quad (2.3)$$

The constant term  $C$  includes calibration errors and affects the resolution function as a whole. The noise term  $N$  is due to residual radioactivity from the uranium in the calorimeter and is only important at low energies. The sampling term  $S$  is due to sampling fluctuations and is the dominant term. The following values for the three contributions were measured for electrons:

$$C = 0.003 \pm 0.002 \quad S = 0.157 \pm 0.005 \text{ GeV}^{\frac{1}{2}} \quad N \approx 0.140 \text{ GeV} \quad (2.4)$$

while for pions they were:

$$C = 0.032 \pm 0.004 \quad S = 0.41 \pm 0.04 \text{ GeV}^{\frac{1}{2}} \quad N \approx 1.28 \text{ GeV} \quad (2.5)$$

The parameters measured for electrons reflect the resolution of the electromagnetic calorimeter. For the hadronic calorimeter, the actual resolution depends on the particle content of the hadronic showers and will in most cases be worse than that for pions. Moreover, even two hadronic jets with the same energy that both contain mostly pions can have different responses in the calorimeter if one jet contains one very high energy pion while the other contains a large number of low energy pions.

## 2.5 The Muon System

Although this analysis does not make use of muons, the muon detector should be briefly described as an integral part of the DØ detector. Due to their long lifetime of  $2.2 \mu\text{s}$  and large mass  $m_\mu \approx 200m_e$ , muons don't likely decay and initiate electromagnetic showers within the detector. Only muons are likely to penetrate the calorimeter.

The muon detector system, as shown in Figure 2.10, consists of five magnetized iron toroids and three layers of proportional drift tubes (PDT's). One Wide Angle Muon System(WAMUS) is mounted in the central region, while two Small Angle Muon Systems(SAMUS) are located at the both ends. The principle of operation of muon PDT is nearly identical to that of VTX, CDC and FDC. Since muon detectors have multi-layer PDT, they are used to measured the trajectory of a muon and thus the momentum.

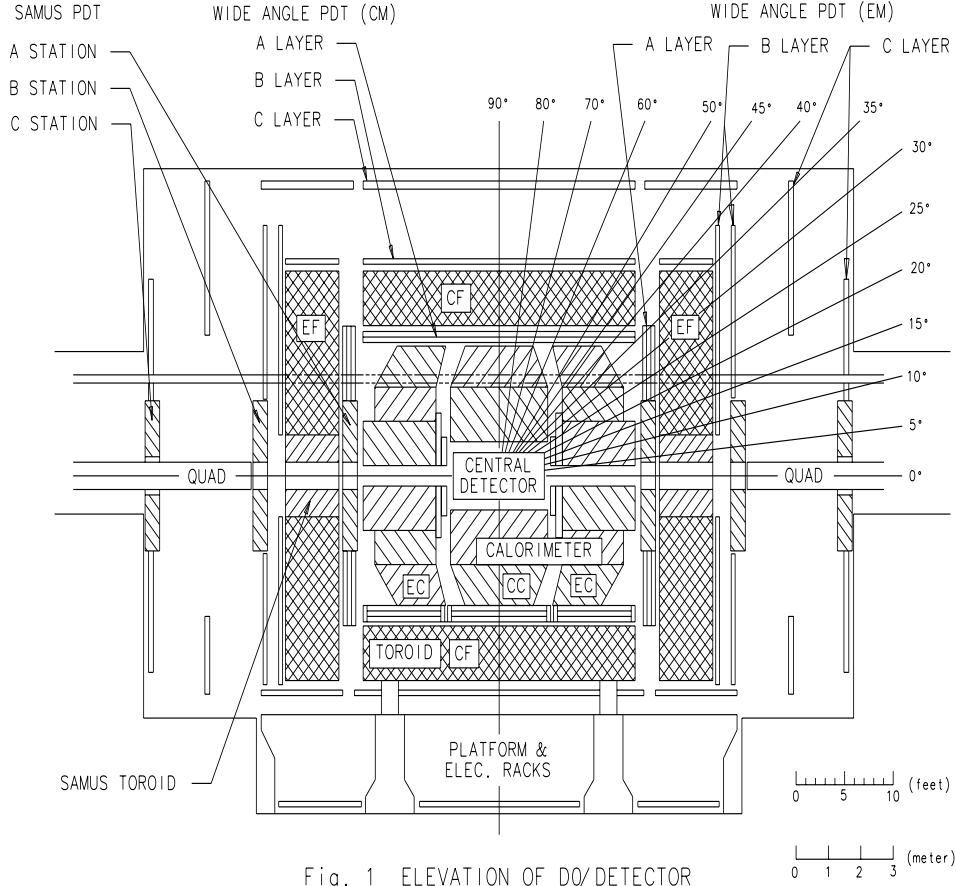


Figure 2.10: Side view of the muon system.

## 2.6 The Trigger System for Data Acquisition

The Tevatron operates with  $3.5 \mu s$  interval between bunch crossing during Run 1 which is 286 kHz. At a luminosity of  $5 \times 10^{30} \text{ cm}^{-2} \text{ s}^{-1}$ , this amounts to an average of about 1.2 interactions per crossing. It is neither practical nor necessary to read out all data at each crossing. Most physics processes of interest have rather small cross sections (for example top (5nb), W (25 nb)) compared to the total (elastic and inelastic)  $p\bar{p}$  cross section of 70 mb at  $\sqrt{s} = 1.8 \text{ TeV}$ . The process of choosing the desired events is called triggering and it is carried out in different stages. A three step trigger system of increasing complexity as shown in Figure 2.11 is implemented to quickly make these decisions with respect to various physics criteria.

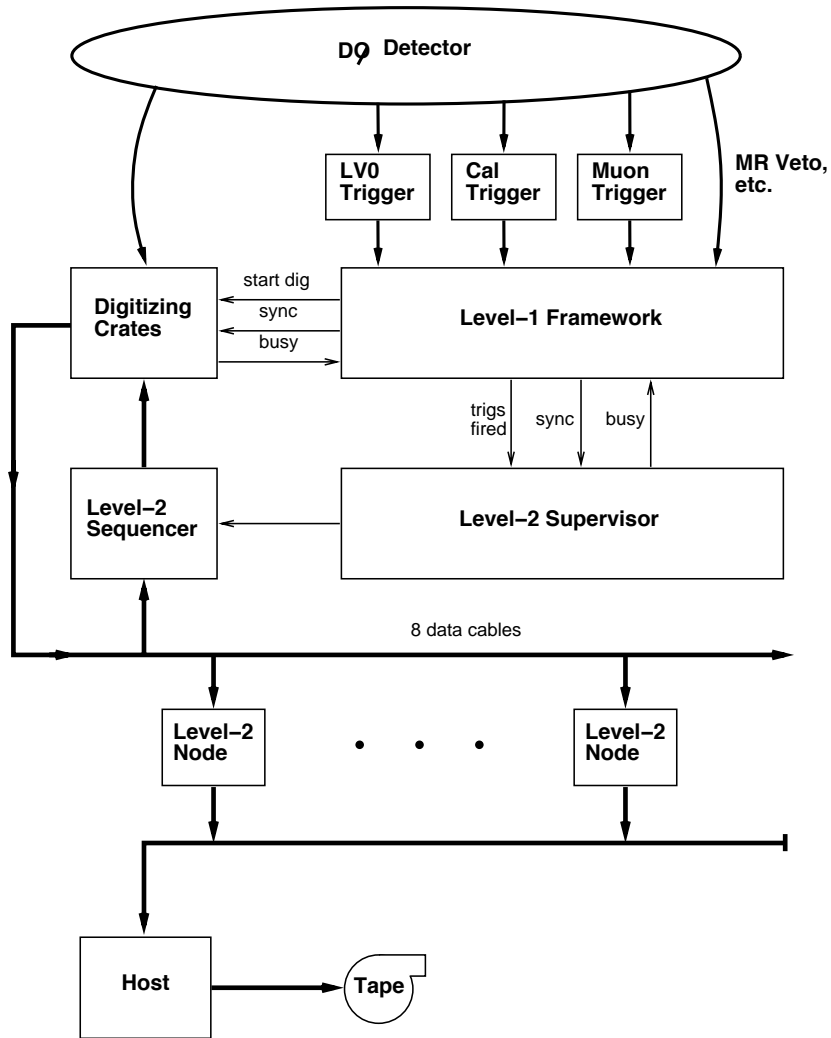


Figure 2.11: DØ trigger and data acquisition system.

### 2.6.1 Level-0

In the first stage, called Level-0, inelastic collisions are detected using scintillation counter hodoscopes installed on each end of the EC modules. This reduces the rate to 150 kHz. The information obtained from these scintillation counters serves several purposes:

- Trigger on inelastic  $p\bar{p}$  collisions with efficiency  $> 99\%$
- Luminosity monitoring
- Identification of multiple interaction within one beam crossing
- Fast determination of the  $z$ - coordinate of the interaction vertex

### 2.6.2 Level-1

The Level-1 trigger system [49, 50, 51] is a hardware trigger that uses coarse information from the calorimeter, the muon system, the Level-0 counter and accelerator timing signal in order to select events of interest. At its heart lies the Level-1 trigger framework which is a programmable hardware processor that coordinates various vetos that can inhibit triggers, accounts for trigger rates and dead-times, and digitizes the data before transporting to the Level-2 trigger. It consists of a network of 256 AND-OR single bit trigger terms. Each of these terms is related to a specific condition, such as  $\cancel{E}_T \geq 20$  GeV or at least two muons present. A subsequent and/or network then reduces these 256 trigger terms to 32 Level-1 trigger bits or specific triggers. Each Level-1 trigger is a logical combination of 256 input terms. These triggers can be pre-scaled so as to control the input rate to the Level-2 trigger.

Trigger vetos are related to any Main ring activity. This occurs mainly during injection (every 2.4 s) and transition (300 ms later) time. There will induce large

amounts of noise in the calorimeter since the Main Ring passes through the DØ detector. Veto signals in the Level-1 framework are implemented to reject events where these conditions apply: The MRBS\_LOSS condition rejects events within a 400 ms window following an injection which results in  $0.4 \text{ s} / 2.4 \text{ s} \approx 17\%$  dead time. The MICRO\_BLANK bit is set when Main Ring bunches pass through the detector within  $1.6 \mu\text{s}$  of a Tevatron beam crossing, resulting in 8 % dead time.

The Level-1 trigger system operates mainly without dead time, i.e. within the  $3.5 \mu\text{s}$  between beam crossings. It further reduces the event rate to about 100 Hz. Some of the Level-1 trigger decisions, called Level-1.5 [52], require additional time. After Level-1, events are fully digitized and can be transferred to Level-2.

### 2.6.3 Level-2

The Level-2 system serves both as the DØ data acquisition system and as a software trigger. It is composed of 48 parallel microprocessors and reduce the input 100 Hz to 2 Hz and output to the magnetic recording medium.

The Level-2 processor run software filters on the complete data for an event. When a event passes a Level-1 trigger, that information is digitized and sent to Level-2 nodes. The Level-2 then performs a partial reconstruction of the event using information from all subsystems of the detector. This includes digital information unavailable to the Level-1 trigger framework so that full resolution of the detector cab be utilized. The Level-2 reconstruction is built around a series of filter”tools”. Each tool has a specific function related to the identification of physics objects, such as: jets, muons, calorimeter EM clusters, tracks associated with calorimeter clusters, scalar  $E_T$  ( $\Sigma E_T$ ) and  $\cancel{E}_T$ . These tools are called from any one of 128 ”scripts”, or output triggers. A script is composed of Level-1 trigger requirement and any combination of Level-2 tools, depending on what type of event characteristic is desired. Events that pass any script are subsequently logged

into tape for complete event reconstruction and analysis.

Off-line reconstruction is performed on a farm of up to 96 SGI and IBM nodes. Data is stored in ZEBRA [53] format which allows for dynamic memory management in FORTRAN. At DØ, three different types of output files were used: STA's, DST's, and  $\mu$ DST's. STA files contain the raw data of the event along with the result of the reconstruction and are 600-1000 kbytes/event large; DST's only contain a summary of the event data, along with the reconstruction results for high-level objects like electrons, photons, muons, and jets. Their sizes are about 15 kbytes/event.  $\mu$ DST's are even smaller since they contain only the minimum amount of information necessary for physics analyses.

# Chapter 3

## Event Reconstruction and Selection

The Tevatron Run I took place over a period of three years from late 1992 to early 1996. The run was broken up into three distinct periods which are given the labels 1a, 1b and 1c. The data for this analysis were taken during the Tevatron Run 1b from February 1994 to April 1995. The integrated luminosity over this period was  $85 \text{ pb}^{-1}$ .

### 3.1 Event Reconstruction

The raw data recorded by the DØ detector consists of digital signals which contain information about pulse heights, widths and times. These raw data have to be converted into physics objects which can then be used in a physics analysis.

At DØ, a standard software reconstruction package, DØRECO, has been developed to fulfill this task. DØRECO starts by processing the raw data into high-level objects, such as energy clusters in the calorimeter or tracks in the tracking system. The reconstruction includes the following procedures:



- Track reconstruction: find tracks in all three drift chambers(VTX, CDC and FDC)
- Vertex finding: find vertex by a histogram method
- Hit finding in the calorimeter: calculate energy in each cell in a given  $\eta - \phi$  tower
- Missing energy: calculate the missing energy

These objects are in turn combined to form the physical particles that originated in the collision point: electrons, photons, jets, neutrinos, etc.. This analysis uses the events of  $W \rightarrow e\nu$ . The following two sections will concentrate on identification of electrons and missing  $E_t$ .

## 3.2 Electron Identification

Electrons from  $W$  and  $Z$  boson decays typically have a large  $E_t$  and are isolated from other particles. They are associated with a track in the tracking system and have a large deposit of energy in the EM calorimeter.

The algorithms in DØRECO put an emphasis on maximum efficiency in the reconstruction of electrons and photons. This allows a fair amount of background to be present in the data sample. The task of further separating it from real signal is left to the individual analysis. To identify genuine electrons with high efficiency while considerably reducing the background, a set of additional criteria is introduced for this analysis. The first two rely on the calorimeter information and exploit the difference between electromagnetic and hadronic shower: the electromagnetic energy fraction and the H-matrix chi-squared ( $\chi_{hm}^2$ ), which is derived from a shower shape analysis. The third criteria, the shower isolation fraction ( $f_{iso}$ ) is a topological cut designed to select electrons from the decay of  $W$  and  $Z$  bosons.

The fourth cut, the track match significance ( $S_{trk}$ ), quantifies the quality of the track matching performed for electrons using calorimeter and tracking information. Recent analysis in the electroweak group in DØ make use of another criteria: the four variable likelihood, which combine the above variables into a likelihood test.

In the following sub-sections these five electron identification criteria will be described in some details. For more information on the various electron identification cuts and the choices of their values, please see reference [54, 55, 56].

### 3.2.1 Electromagnetic Energy Fraction

By definition, electrons and photons must have more than 90% of their cluster energy deposited in the EM layers of the calorimeter in order to be considered electrons or photons by DØRECO. For electrons from  $W$  and  $Z$  boson decays, this requirement is quite loose. These electrons typically have much larger electromagnetic energy fractions. A tight cut can be used to further reduce background without compromising the selection efficiency. Figure 3.1 shows the electromagnetic energy fraction distribution for  $Z \rightarrow ee$  candidates and fake electron candidates from multi-jet triggered data. Additional background rejection can be obtained by a cut at  $f_{em} = 0.95$ .

### 3.2.2 Shower Shape Analysis

The shower shape of an electromagnetic object (electron and photon) can be characterized by its longitudinal and transverse profile: it is dependent on the fractional energy deposited in each cell of the calorimeter [57, 58, 59]. These fractions, besides being dependent on the incident electron energy and impact position, are correlated: if a shower deposits more energy in the first layer of the electromagnetic calorimeter due to a fluctuation it will on average deposit less in the subsequent layers, and vice versa. To fully account for all possible correlations, a covariance

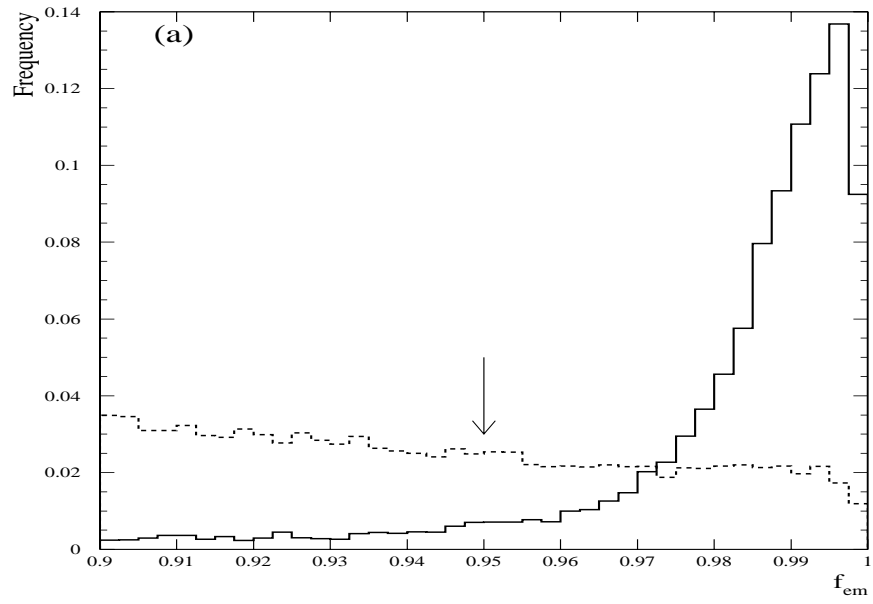


Figure 3.1: Electromagnetic energy fraction  $f_{em}$  distributions for  $Z \rightarrow ee$  candidates (solid) and electrons in multi-jet triggered data (dashed) (Central Electrons).

matrix  $M$  of 41 observables is built which is a measure of how “electron-like” a shower is. The variables are the fractional energies in layers EM1, EM2, and EM4 of the calorimeter and the fractional energy in each cell of a  $6 \times 6$  array in  $\eta - \phi$  space of the finely segmented EM3 centered around the most energetic tower in the cluster. The logarithm of the cluster energy is included to account for the dependence of the fractional energy on the cluster energy. Finally, the  $z$ -coordinate of the interaction vertex is included to account for the dependence of the shower shape on the incidence angle into the calorimeter. Since the geometry of the calorimeter is  $\eta$ -dependent, 37 different matrices  $M$  are built, one for each tower in pseudorapidity in one half of the calorimeter. The other 37 in the other half can simply be obtained using the fact that the calorimeter is mirror-symmetric.

The covariance matrix  $M$  is computed using Monte Carlo electrons with a large energy range (from 10 GeV to 150 GeV). For two variables  $x_i$  and  $x_j$  it is defined as:

$$M_{ij} = \frac{1}{N} \sum_{n=1}^N (x_i^n - \bar{x}_i)(x_j^n - \bar{x}_j) \quad (3.1)$$

where the sum is performed over  $N$  reference electrons. The matrices were verified by test beam electrons in order to ensure that they adequately describe real data.

For a particular shower, characterized by the variables  $x'_i$ , the covariance parameter  $\chi^2$  is computed as follows:

$$\chi_{hm}^2 = \sum_{i,j=1}^{41} (x'_i - \bar{x}_i) H_{ij} (x'_j - \bar{x}_j) \quad (3.2)$$

where  $H = M^{-1}$  is the error matrix obtained from the inverse of the correlation matrix  $M$ . A shower that closely resembles an electromagnetic shower will have a low  $\chi_{hm}^2$ . The  $\chi_{hm}^2$ -distribution does not follow a true  $\chi^2$  distribution because in general, the observables  $x_i$  are not normally distributed. Nevertheless, this variable offers strong rejection power against background sources, since only genuine electrons will have a low  $\chi_{hm}^2$ , as illustrated in Figure 3.2. This plot shows the

distributions of the H-matrix  $\chi^2$  variable for test beam electrons and electrons from  $W$  boson events and compares these to test beam pions. Electrons peak at low values of  $\chi_{hm}^2$  while pions pile up at large values. Figure 3.3 shows  $\chi_{hm}^2$  distributions for electrons from  $Z \rightarrow ee$  candidates and fake electrons in multi-jet triggered data. In this analysis, electron candidates are required to have  $\chi_{hm}^2 < 100$ .

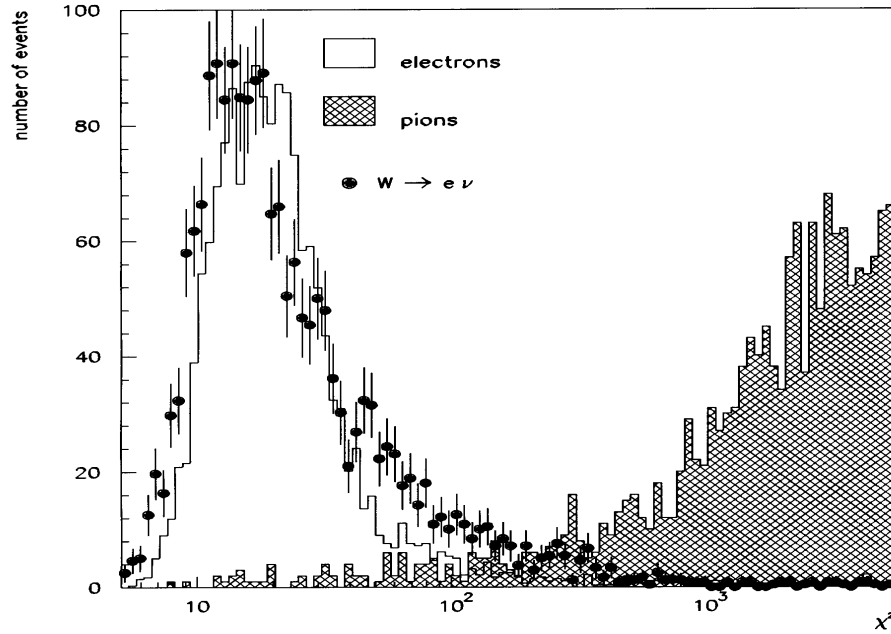


Figure 3.2:  $\chi_{hm}^2$  distributions for test beam electrons (unshaded), test beam pions (shaded), and electrons from  $W \rightarrow e\nu$  events (dots).

### 3.2.3 Shower Isolation

Electrons originating from  $W$  and  $Z$  boson decays are isolated since these electrons are not produced in association with other particles. In contrast, the production of  $\pi^0$  and  $\eta$  particles (which can decay into photons and create an electromagnetic shower) or electrons from heavy quark decays, are often accompanied by other hadrons.

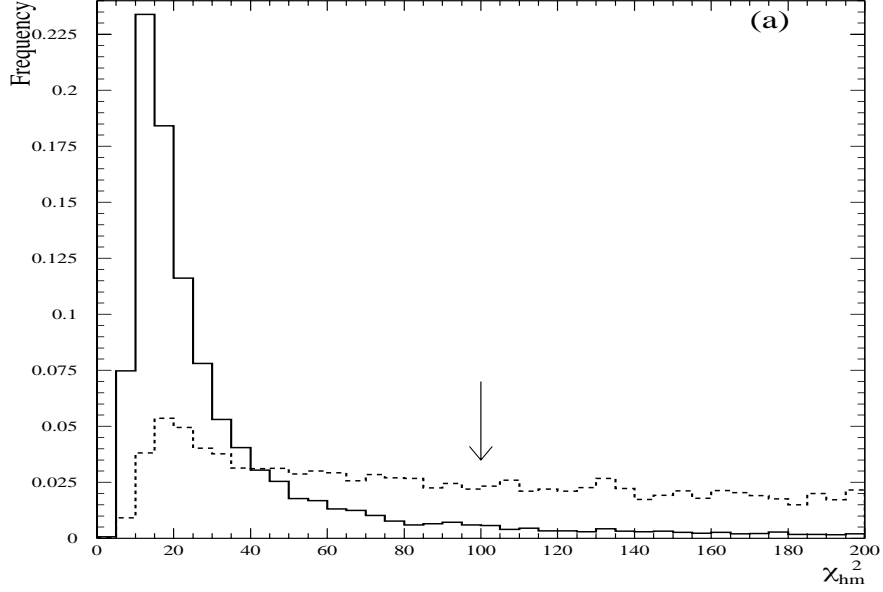


Figure 3.3: H-matrix  $\chi_{hm}^2$  distributions for electrons from  $Z \rightarrow ee$  candidates (solid) and electrons in multi-jet triggered data (dashed) (Central electrons).

An isolation variable is defined as:

$$f_{iso} = \frac{E_{total}(0.4) - E_{EM}(0.2)}{E_{EM}(0.2)} \quad (3.3)$$

where  $E_{total}(0.4)$  is the total energy in an isolation cone of radius  $\mathcal{R} = 0.4$  and  $E_{EM}(0.2)$  is the electromagnetic energy in a core cone of radius  $\mathcal{R} = 0.2$ . Figure 3.4 compares the  $f_{iso}$  distributions of electrons from  $Z \rightarrow ee$  events to the ones from multi-jet triggered data. In this analysis, a cut on  $f_{iso} < 0.15$  is imposed on all electron candidates.

### 3.2.4 Track Matching

Electrons are defined by DØRECO as electromagnetic clusters with a track present in a road defined by the vertex position and the cluster centroid. This definition is quite loose and background contamination due to accidental overlaps (such as pres-

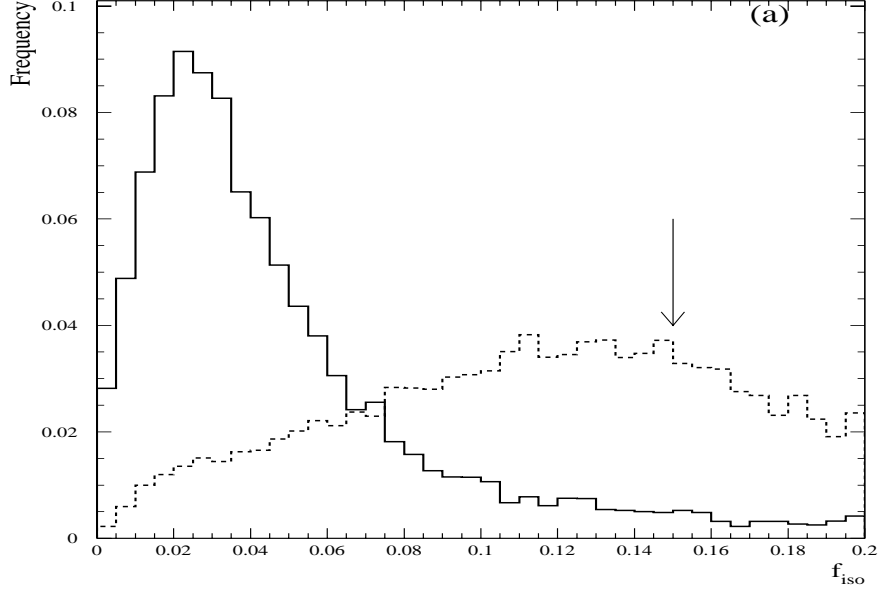


Figure 3.4: Isolation distribution  $f_{iso}$  for electrons from  $Z \rightarrow ee$  candidates (solid) and electrons in multi-jet triggered data (dashed) (Central electrons).

ence of  $\pi^0$  and  $\eta$  and additional nearby soft charged hadrons) can be substantial. The track of genuine electron is expected to be well aligned with the calorimeter cluster. If tight cluster-track matching is performed, background can be rejected.

Tracks produced by electrons can be distinguished from accidental overlaps by taking into account how well their projections from the interaction vertex into the EM3 layer of the calorimeter match the cluster centroids. Tracks associated with real electrons will have a very good track match. The track match significance in the central calorimeter is defined as follows:

$$S_{trk}^{CC} = \sqrt{\left(\frac{\rho\Delta\phi}{\sigma_{\rho\phi}}\right)^2 + \left(\frac{\Delta z}{\sigma_z}\right)^2} \quad (3.4)$$

where  $\rho\Delta\phi$  is the transverse spatial mismatch,  $\Delta z$  is the longitudinal spatial mismatch, and  $\sigma_{\rho\phi}$ , and  $\sigma_z$  are the corresponding resolutions. For the endcap calorimeter a similar expression exists:

$$S_{trk}^{EC} = \sqrt{\left(\frac{\rho\Delta\phi}{\sigma_{\rho\phi}}\right)^2 + \left(\frac{\Delta\rho}{\sigma_\rho}\right)^2} \quad (3.5)$$

where  $\rho\Delta\phi$  is the transverse spatial mismatch,  $\Delta\rho$  is the longitudinal spatial mismatch, and  $\sigma_{\rho\phi}$ , and  $\sigma_\rho$  are the corresponding resolutions. Figure 3.5 illustrates the definition for  $S_{trk}$ . In figure 3.6, the  $S_{trk}$  distribution for electrons from  $Z \rightarrow ee$  candidates is compared to electron candidates from the same control sample as before. A cut of 5 in the CC reduces the rate for fake electrons significantly while keeping the acceptance for real electrons high.

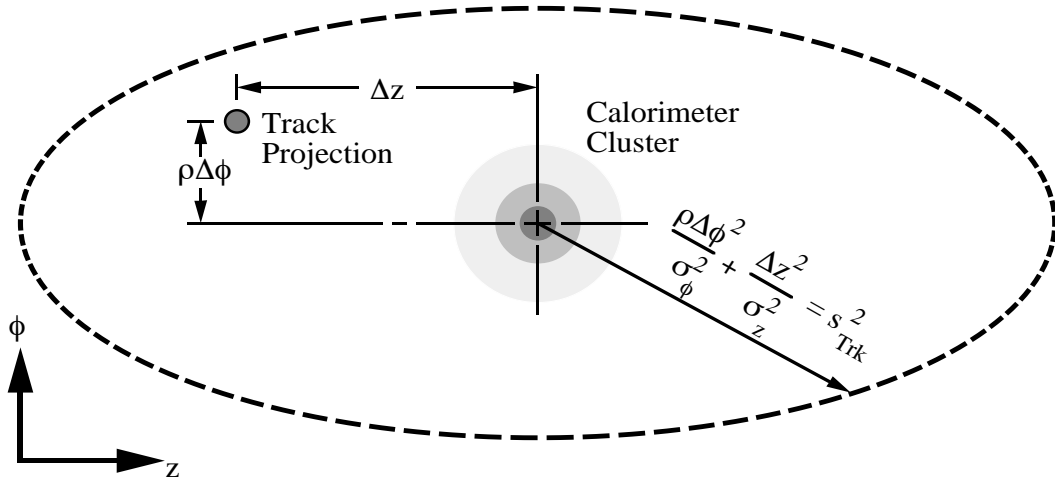


Figure 3.5: Definition of the track match significance in terms of the cluster centroid in EM3 and the projection of the track to that radius.

### 3.2.5 The Four Variable Likelihood Function

Better background rejection while maintaining high electron selection efficiency can be obtained by combining the individual electron identification variables into a likelihood test [55, 56]. A probability ratio using a Neyman-Pearson test for two hypotheses  $H$ , signal ( $H = e$ ) and background ( $H = b$ ) is defined as:



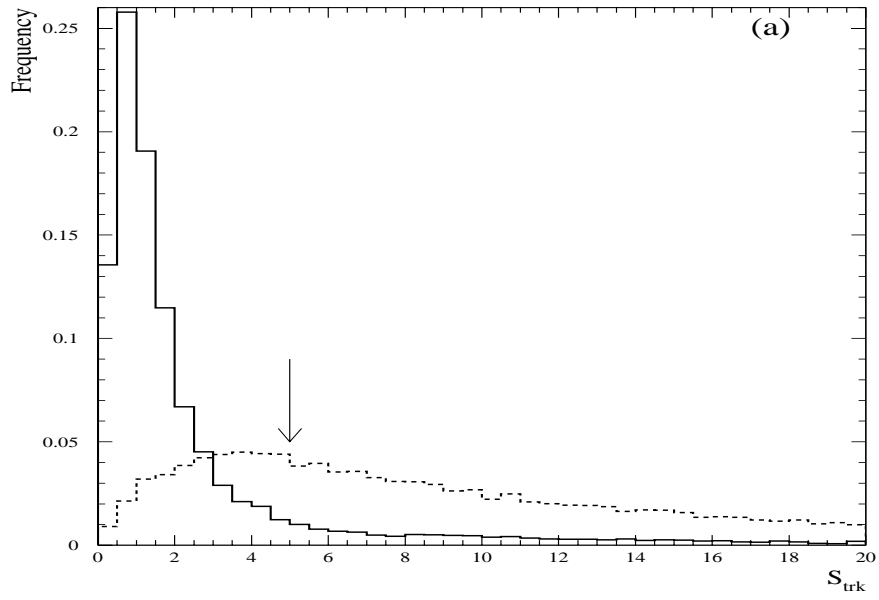


Figure 3.6: Track match significance distribution  $S_{trk}$  for electrons from  $Z \rightarrow ee$  candidates(solid) and electrons in multi-jet triggered data (dashed) (Central electrons).

$$\mathcal{R}(f_h) \equiv \frac{p(x|b)}{p(x|e)} = \frac{f_h p(x|h) + (1 - f_h) p(x|ee)}{p(x|e)} \quad (3.6)$$

where  $x$  is an observable and  $p(x|H)$  is the probability density for  $x$  given  $H$  is true. The background consists of two components, conversions ( $H = ee$ ) and hadron overlaps ( $H = h$ ) with fraction  $f_h$  of hadron overlaps in the background. A candidate EM cluster is considered an electron if  $\mathcal{R} < k$  where  $k$  is chosen to select the desired efficiency and background rejection for a specific analysis. The probability density is calculated by forming the joint likelihood of the four variables CDC  $dE/dx$ , H-matrix  $\chi^2$ , track match significance  $\sigma_{trk}$ , and EM energy fraction  $f_{EM}$ :

$$p(x|H) = p_1(dE/dx|H) \times p_2(\chi^2|H) \times p_3(\sigma_{trk}|H) \times p_4(f_{EM}|H) \quad (3.7)$$

To reduce the QCD background to a low level even at large transverse momentum, a rather tight cut on the 4-variable likelihood of 0.25 is imposed on the candidate electron in the central calorimeter(CC).

### 3.2.6 Off-line Electron Selection

Before proceeding to the selection of  $W$  and  $Z$  boson events, a description of the electron selection is given below. Two classifications of electrons are defined to describe the signal electron: a loose selection for “loose” electrons and a tight selection for tight electrons. The tight electrons form a subset of the loose one and are the electrons for  $W$  event selection. The loose electrons are for the study of detector and background. In order to ensure a well understood detector response, the fiducial region is selected such that non-instrumented or poorly instrumented regions of the detector are eliminated. These regions include the inter-cryostat

region between the CC and EC calorimeters and the boundaries between the electromagnetic central calorimeter modules.

The loose electrons are defined as follows:

- EM cluster in the good fiducial region:
  - EM cluster in central calorimeter:  $|\eta| < 1.1$
  - EM cluster in good CC module:  $0.1 < \text{mod}(\phi_{cluster}^e, 2\pi/32) < 0.90$

The definition for tight electrons is:

- Loose electron
- H-matrix: shower shape consistent with that expected for an electron:

$$\chi^2 < 100$$

- Track match significance:  $\sigma_{trk} < 5$
- High EM fraction:

$$f_{em} > 0.95$$

- Cluster position:  $|Z_{clus}| < 108 \text{ cm}$
- Track location:  $|Z_{trk}| < 80 \text{ cm}$
- Isolation of the EM cluster:

$$f_{iso} < 0.15$$

- 4-variable likelihood  $< 0.25$

### 3.3 Neutrino Identification

The cross sections for processes by which neutrinos could be detected are extremely small. Most neutrinos pass through the detector undetected and thus create an apparent momentum imbalance in an event. The transverse momentum of the neutrinos can, nevertheless, be measured by applying momentum conservation and the fact that the initial transverse momentum of the quark-antiquark system is small ( $\approx 300$  MeV). The energy imbalance, referred to as  $\cancel{E}_T$ , is calculated by adding the calorimeter energies componentwise at the cell level:

$$\cancel{E}_x = - \sum_{e,p,l} E_x(e,p,l) \quad \cancel{E}_y = - \sum_{e,p,l} E_y(e,p,l) \quad (3.8)$$

and

$$\vec{\cancel{E}}_T = \begin{pmatrix} \cancel{E}_x \\ \cancel{E}_y \end{pmatrix} \quad (3.9)$$

The missing transverse energy,  $\cancel{E}_T$ , is the magnitude of this vector:

$$\cancel{E}_T = |\vec{\cancel{E}}_T| = \sqrt{\cancel{E}_x^2 + \cancel{E}_y^2} \quad (3.10)$$

Since particles emitted in the forward direction often escape the detector undetected, the  $z$ -component of the missing energy cannot be associated with the longitudinal component of the neutrino momentum in this way.

### 3.4 $W \rightarrow e\nu$ Event Selection

Candidate  $W \rightarrow e\nu$  events are selected through their signature of an isolated, high- $p_T$  electron and a high- $p_T$  neutrino. The selection has two stages: online trigger and off-line. The online trigger requirements are rather loose and off-line requirements are imposed to optimize the signal to background ratio.

### 3.4.1 $W \rightarrow e\nu$ Trigger

The  $W \rightarrow e\nu$  data sample was collected with the `EM1_EISTRACKCC_MS` trigger. This trigger was configured with following conditions:

- Level-0 trigger(hardware): inelastic scattering
- Level-1 trigger(hardware)
  - $E_T^{em} > 12GeV$
  - `GOODCAL` Main Ring beam veto: see discussion below.
- Level-1.5 trigger(hardware)
  - $E_T^{em} > 15GeV$
  - $f_{em} > 0.85$
- Level-2 trigger(software)
  - $E_T > 20GeV$
  - Loose shower shape ( $ele$ ) and isolation fraction( $iso$ )
  - $\cancel{E}_T > 15GeV$

As mentioned earlier, the Main Ring component of the Tevatron passes through the outer part of the hadronic calorimeter. Beam losses from the Main Ring can create significant energy deposits in the calorimeter, resulting in a large false  $\cancel{E}_T$ . This occurs when beam is being injected into the Main Ring. Events occurring within a 400ms windows (called the `MRBS_LOSS` windows) of the injection are rejected by the `GOODCAL` requirement, leading to only a very small loss of data. Large beam losses can also occur when particles in the Main Ring pass through the  $D\bar{O}$  detector. Events within  $1.6 \mu s$  windows (called the `MICRO_BLANK` window) around these time period are rejected off-line, resulting in about 8% loss of data.

The GOODCAL veto rejects events occurring in the MRBS\_LOSS or MICRO\_BLANK time window.

### 3.4.2 $W \rightarrow e\nu$ Off-line Selection

We select  $W \rightarrow e\nu$  events in the central calorimeter(CC) region for this analysis. We require the electron to be a tight electron in the CC fiducial region and the  $W$  candidates are selected by requiring:

- GOODCAL Main Ring beam veto
- Events that pass the EMI\_EISTRKCC\_MS L2 filter
- One tight electron,  $E_T > 25 \text{ GeV}$
- $\cancel{E}_T > 25 \text{ GeV}$
- $p_T(W) < 15 \text{ GeV}/c$
- $|Z_{vtx}| < 100 \text{ cm}$

After applying selection cuts, we have data samples of 24485 candidate events. The transverse mass distribution of the  $W$  candidates is shown in Figure 3.7. The bin size is 5 GeV. There are 24479 events located in the region 0-200 GeV.

## 3.5 $Z \rightarrow ee$ Event Selection

Candidate  $Z \rightarrow ee$  events are selected by requiring two isolated high- $p_T$  electrons. The selection procedure is similar to  $W$  event selection and has two stages: trigger and off-line.

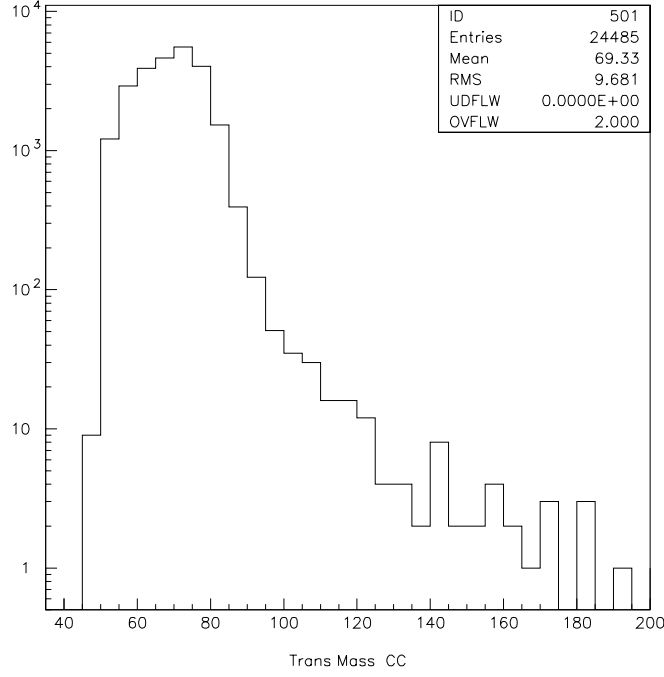


Figure 3.7: Transverse mass distribution of the  $W$  candidates on logarithmic scale.

The bin size is 5 GeV. The total number of events is 24485, while 24479 events are in the region 0-200 GeV . (There are 24483 events in 0-250 GeV)

### 3.5.1 $Z \rightarrow ee$ Trigger

The  $Z \rightarrow ee$  data sample was collected with the *EM2\_EIS2\_HI* trigger. This trigger had the following requirements:

- Level-0 trigger: universal Level-0 requirement
- Level-1
  - 2 EM objects with  $E_T^{em} > 7.0 GeV$
  - GOODCAL Main Ring beam veto
- Level-1.5

- 2 EM objects with  $E_T^{em} > 12.0 GeV$
- 2 EM objects with  $f_{em} > 0.85$
- Level-2
  - 2 EM objects with  $E_T^{em} > 20.0 GeV$
  - Loose shower and isolation fraction cut on both objects

### 3.5.2 $Z \rightarrow ee$ Off-line Selection

The cuts to select  $Z \rightarrow ee$  events are:

- GOODCAL Main Ring beam veto
- Events that pass the *EM2\_EIS2\_HI* L2 filter
- Two tight CC electron,  $E_T > 25 GeV$
- $60 < m_{ee} < 120$  GeV
- $|Z_{vtx}| < 100$  cm
- both electrons to have a track

A total of 1997 events passes the  $Z \rightarrow ee$  selection criteria. Figure 3.8 is the invariant mass distribution of  $Z \rightarrow ee$  events

## 3.6 Event Displays

To get a feeling for what a typical  $W$  boson event looks like, event displays for two different candidate events are included. Figure 3.9 shows a  $W$  candidate in the end view. A well-collimated electromagnetic energy cluster can be seen as well as large missing  $E_T$ . Figure 3.10 shows another candidate event in the  $\eta - \phi$  view.



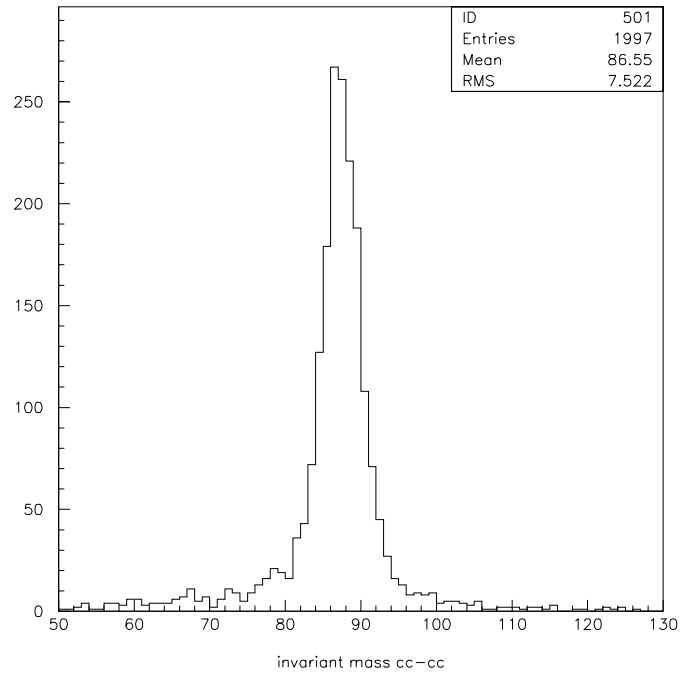


Figure 3.8: Invariant mass distribution of  $Z \rightarrow e^+e^-$  event. Both electron are required to be in the CC region.

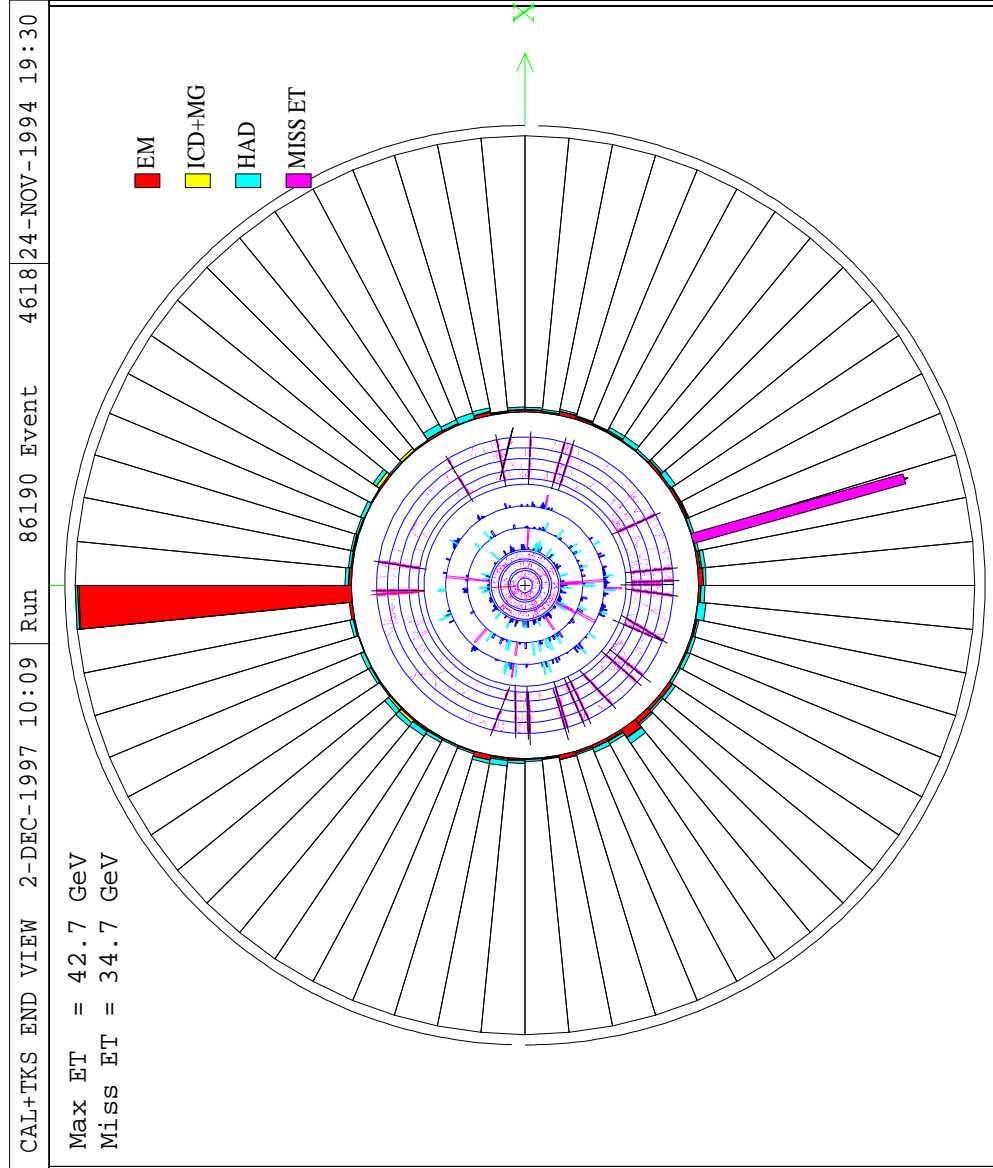


Figure 3.9:  $W$  Boson candidate, end view.

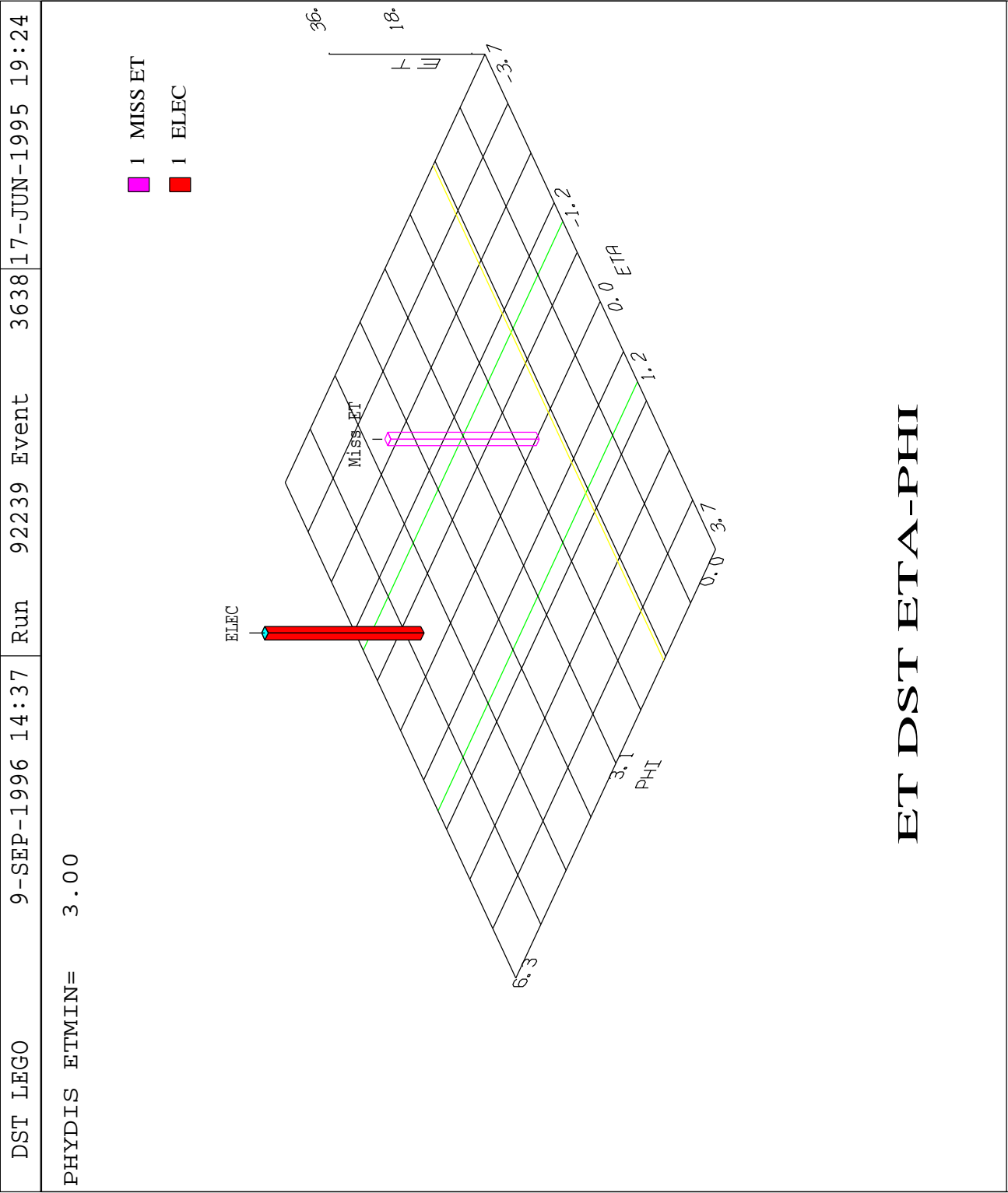


Figure 3.10:  $W$  Boson candidate.

# Chapter 4

## Background Estimation

Several processes can mimic the  $W \rightarrow e\nu$  signal and pass the  $W$  selection criteria and contaminate the data sample. We can estimate the background and make corrections to the measurement results.

### 4.1 Background Description

The background events in the data sample can be physical or instrumental. Physical backgrounds are the results of other physics process with a final state that is indistinguishable from the one under study. For the event sample  $W \rightarrow e\nu$ , one of the examples is  $W \rightarrow \tau\nu$ , where the tau can further decay into an electron and two neutrinos, giving a final state with an electron and  $\cancel{E}_T$ . Instrumental backgrounds are the results of physical processes with final state different from the one under study, but which are misidentified by the detector.

The  $W$  events cuts are designed to accept desired  $W$  events with high efficiency while rejecting as much background as possible. It is desirable to have a large sample of signal events in order to reduce statistical and therefore systematic uncertainties in some cases. These event cuts represent a compromise between

retaining high efficiency and reducing background. As a result, a small amount of background will enter into the data sample unavoidably. This should not cause a problem to the physics measurement as long as one has a good understanding of the amount of background.

The backgrounds to  $W \rightarrow e\nu$  events come from three sources: QCD multijet,  $Z \rightarrow e^+e^-$  and  $W \rightarrow \tau\nu \rightarrow e\nu\bar{\nu}\nu$ . For QCD multijet events, one jet may be lost in an un-instrumented region of the detector, while the others may pass our electron selection criteria and become fake electrons. For a similar reason, the process  $Z \rightarrow e^+e^-$  can also enter into the  $W \rightarrow e\nu$  data sample, where one electron is detected and the other is lost. The process  $W \rightarrow \tau\nu \rightarrow e\nu\bar{\nu}\nu$  has a signature similar to  $W \rightarrow e\nu$  decays, but at lower  $p_t$  and is included in our fast Monte Carlo simulation.

## 4.2 QCD Background

There are several methods to estimate the QCD background. In this analysis, the matrix method is used. The idea of the matrix method is to find two sets of data samples, both of which contain the signal and the background. One data set is a sub-set of the other through certain cuts. If we can determine the efficiency of both the signal and the background for these cuts, we can calculate the background from a simple algebra. The detailed matrix method description can be found in reference [60].

We define two sets of samples to determine the QCD background: the tight sample, which passes the cuts of all the  $W \rightarrow e\nu$  candidate selection, and the loose sample, which has one loose electron and passes all  $W$  selection cuts. The tight sample is just our data sample. The definition for the loose electron is: the existence of a cluster with  $|Z_{clus}| < 108 \text{ cm}$ , fiducial region:  $|\eta| < 1.1$  and  $0.1 < \text{mod}(\phi_{cluster}^e, 2\pi/32) < 0.90$ . This definition is consistent with that in the

CC and EC  $W$  mass analyses [61, 62, 63].

In the loose sample, the total number of events ( $N$ ) is composed of both the real signal events ( $N_s$ ) and the background events ( $N_b$ ), s.t.

$$N = N_b + N_s \quad (4.1)$$

In the tight sample, the total number of events  $N_t$ , is composed of the real signal events that pass the selection cuts and the background events that fake a signal, s.t.

$$N_t = \varepsilon_j N_b + \varepsilon_e N_s \quad (4.2)$$

where  $\varepsilon_e$  is the efficiency of the tight cuts for electron and  $\varepsilon_j$  is the efficiency for a jet to fake an electron.

The total number of QCD multi-jet background events as a function of the measurable quantities is given by

$$N^{QCD} = \varepsilon_j N_b \quad (4.3)$$

$$= \frac{\varepsilon_j}{\varepsilon_e - \varepsilon_j} (\varepsilon_e N - N_t) \quad (4.4)$$

and therefore the background fraction is

$$f_{QCD} = \frac{\varepsilon_j N_b}{N_t} = \frac{\varepsilon_j}{\varepsilon_e - \varepsilon_j} \frac{\varepsilon_e N - N_t}{N_t} \quad (4.5)$$

After we select the two data samples, it is important to measure the efficiencies  $\varepsilon_e$  and  $\varepsilon_j$ .

### 4.2.1 Electron Efficiency Determination

The only difference between the cuts for the loose sample and the tight sample is the electron cuts. The efficiency of the tight cuts is the efficiency of tight electron cuts. To calculate this, we need a clean sample of unbiased electrons. This diagnostic electron sample comes from the standard  $Z \rightarrow ee$  sample.

Our sample selection begins with events passing the `EM2_EIS_ESC` filter. This filter requires two EM clusters, where one cluster is isolated and has transverse energy  $E_T^{L2} > 20$  GeV, while the other has transverse energy  $E_T^{L2} > 16$  GeV. The event consists of two electron candidates in a good fiducial region of the detector, with  $E_T^e > 25$  GeV. Tight cuts are applied on one of the electrons, including  $E_T^{L2} > 20$  GeV and loose trigger isolation. If an electron passes the tight cuts, it is used to determine the  $z$ -coordinate of the event and the transverse energy of the electrons. The only condition applied to the second electron is  $E_T^{L2} > 16$  GeV. This cut is 100% efficient for electrons with off-line transverse energy,  $E_T > 25$  GeV. The second electron will therefore be unbiased and can be used to measure the efficiency. In addition, the invariant mass of the two electrons is required to be close to the true  $Z$  boson mass.

To correct the electron efficiency for any background events in the  $Z \rightarrow ee$  data sample, we use the sideband subtraction method [64]. Two sideband regions ( $57 \text{ GeV}/c^2 < M_{ee} < 67 \text{ GeV}/c^2$  and  $107 \text{ GeV}/c^2 < M_{ee} < 111 \text{ GeV}/c^2$ ), which are dominated by background, are defined around the signal region of  $82 \text{ GeV}/c^2 < M_{ee} < 92 \text{ GeV}/c^2$ . (The reason why the  $Z$  mass is not  $91 \text{ GeV}/c^2$  is that this data sample did not go through CAFIX, which fixes the energy scale [65, 66].) These regions are chosen to be symmetric around the signal region and each of them covers the same bin size in invariant mass. The number of background events is taken to be the average of the two sideband regions. The background subtracted efficiency of the tight cut relative to the loose cut is given by:

$$\varepsilon_e = \frac{N_s^t - N_b^t}{N_s^l - N_b^l}, \quad (4.6)$$

$M_{ee}$ region	Tight Sample	Loose Sample
$57 \text{ GeV}/c^2 < M_{ee} < 67 \text{ GeV}/c^2$	38	46
$82 \text{ GeV}/c^2 < M_{ee} < 92 \text{ GeV}/c^2$	1682	1951
$107 \text{ GeV}/c^2 < M_{ee} < 117 \text{ GeV}/c^2$	17	23
Average Background	27.5	34.5

Table 4.1: Number of  $Z \rightarrow ee$  events for tight and loose samples.

With the Run 1B  $Z \rightarrow ee$  data sample, we find the number of events as listed in Table 4.1. From it, we found the background subtracted result is

$$\varepsilon_t = 0.8633 \pm 0.0078(stat) \quad (4.7)$$

The invariant  $Z$  mass for loose and tight events is shown in figure 4.1.

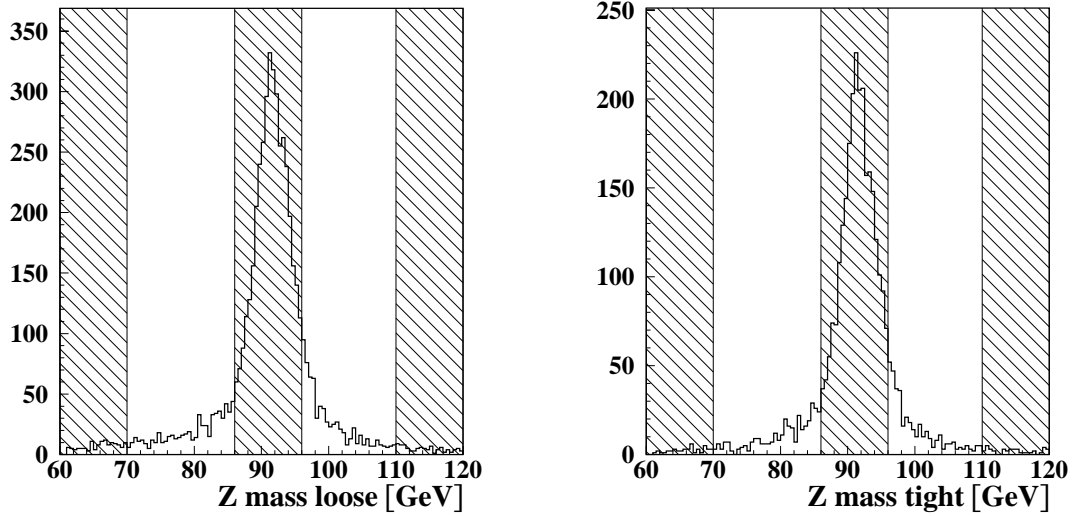


Figure 4.1:  $Z$  invariant mass for loose (left) and tight (right) electrons. The signal region and the two side-bands are hatched.

As a comparison, the efficiency without background subtraction is  $\varepsilon_t = 0.8621 \pm$



$0.0078(stat)$ . (The previous analysis of differential cross section of  $W$  [60] has  $\varepsilon_e = 0.8675 \pm 0.0047(stat)$ ).

The systematic uncertainties are determined by the standard weighted least-square procedure [12], following the unconstrained averaging prescription from the Particle Data Book. We can find  $\varepsilon_e$  in each bin and calculate the  $\chi^2$ . The systematic uncertainty is determined so that  $\chi^2$  is equal to one per degree of freedom and we have a systematic error of 0.0088. The efficiency is  $\varepsilon_e = 0.8633 \pm 0.0078(stat) \pm 0.0088(syst)$ . This leads to an overall efficiency

$$\varepsilon_t = 0.8633 \pm 0.0118 \quad (4.8)$$

To check if  $\varepsilon_e$  is dependent on transverse mass, we use the  $W \rightarrow e\nu$  events. By using the same method above, we divide the sample into three regions in transverse mass with roughly same events in each region. The results are  $\varepsilon_t = 0.8214 \pm 0.0048$  for  $m_T$  from 0 to 65  $GeV$ ,  $\varepsilon_t = 0.8399 \pm 0.0041$  for  $m_T$  from 65 to 75  $GeV$  and  $\varepsilon_t = 0.8280 \pm 0.0050$  for  $m_T$  from 75 to 200  $GeV$ . The uncertainties are statistical only. (The reason why  $\varepsilon_t$  is different from the above is that different L2 triggers are used.) So we can conclude that the dependence of  $\varepsilon_e$  on transverse mass in the interesting region is very small and we can take  $\varepsilon_e$  as constant over the whole region.

## 4.2.2 Jet Efficiency Determination

The jet efficiency ( $\varepsilon_j$ ) is obtained from a sample dominated by jets. We use a data sample with electron trigger EM1\_ELE\_MON. This trigger does not have a  $\cancel{E}_T$  requirement at Level-2. In the low  $\cancel{E}_T$  region (for example below 15  $GeV$ ), the events are dominated by background and they can be used to determine this jet efficiency. We selected two samples of events from this data, a tight sample and a loose sample. The tight sample requires the jet to pass tight electron cuts and the loose sample contains jets that pass the loose electron cuts. The efficiency is

$\cancel{E}_T$ region	event number	event number	$\varepsilon_j$
	in tight sample	in loose sample	
$0 < \cancel{E}_T < 5 \text{ GeV}$	551	9298	5.93%
$0 < \cancel{E}_T < 10 \text{ GeV}$	1086	19264	5.64%
$0 < \cancel{E}_T < 15 \text{ GeV}$	1311	22503	5.83%
$5 < \cancel{E}_T < 15 \text{ GeV}$	760	13205	5.76%

Table 4.2: Jet efficiency in different ranges of  $\cancel{E}_T$ .

calculated as the ratio of the number of background events in the tight sample to the number of background events in the loose sample.

$$\varepsilon_j = \frac{N_{tight}(\text{events below } \cancel{E}_T \text{ cut})}{N_{loose}(\text{events below } \cancel{E}_T \text{ cut})} \quad (4.9)$$

Using the data in  $\cancel{E}_T < 10 \text{ GeV}$ , the jet efficiency is:

$$\varepsilon_j = 5.83 \pm 0.16(\text{stat})\% \quad (4.10)$$

The main source of uncertainty comes from the assumption that the electrons from background sources in events with small  $\cancel{E}_T$  have the same value for  $\varepsilon_j$  as those in the signal region (which means  $\cancel{E}_T \approx 25 \text{ GeV}$ ). This uncertainty was studied and evaluated for the cross section measurement [67]. The study shows that the correlation between  $\cancel{E}_T$  and  $\varepsilon_j$  is small.

We estimate systematic uncertainty from the jet efficiency calculated in the region,  $\cancel{E}_T < 10 \text{ GeV}$ . For different  $\cancel{E}_T$  regions, the jet efficiencies are slightly different, as are listed in Table 4.2. We took the largest difference from the inclusive value as the systematic uncertainty, which is 0.19%.

We add these two contributions in quadrature and get 0.25% for total uncertainty. The jet efficiency is then

$$\varepsilon_j = 0.0583 \pm 0.0025 \quad (4.11)$$

### 4.2.3 QCD Background Shape

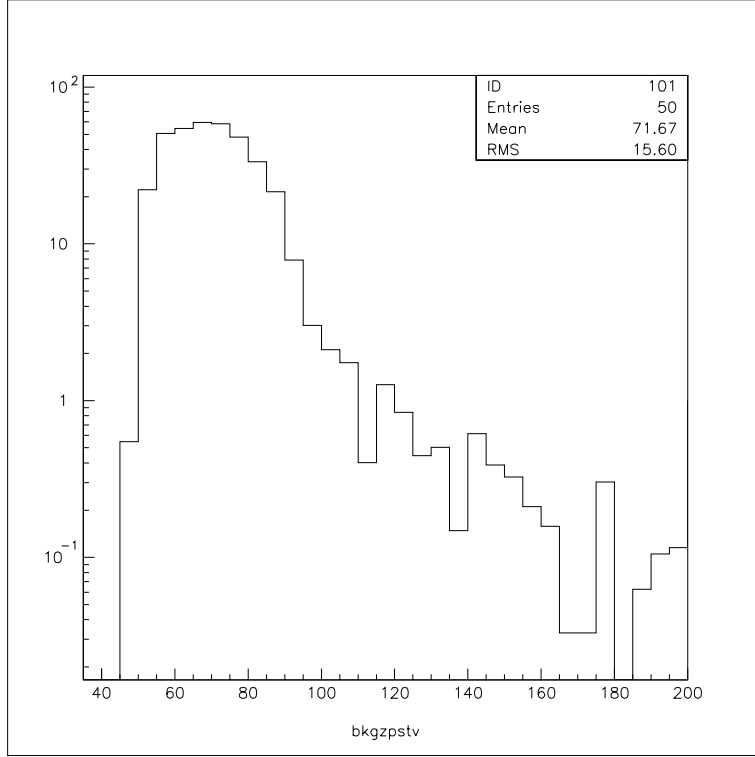


Figure 4.2: QCD background shape as a function of the transverse mass.

We use the efficiencies  $\varepsilon_e$  and  $\varepsilon_j$  to compute the inclusive background number and the fractions from equation (4.4) and equation (4.5). We obtain the estimated inclusive QCD background and its fraction in our data sample as follows

$$N_{QCD} = 367.1 \pm 31.3 \quad (4.12)$$

The result is sensitive to  $\varepsilon_e$ , the electron efficiency. Its uncertainty strongly affects the resultant uncertainty. Due to the limited  $Z \rightarrow ee$  event sample, we

cannot measure  $\varepsilon_e$  to a precision less than 1% and hence leave a large uncertainty in the final QCD background.

From a bin to bin calculation, we find the transverse mass shape of the QCD background. It is shown in Figure 4.2.

#### 4.2.4 QCD Background Fit

Although we can find the QCD background shape from the above bin to bin calculation, the shape has a large fluctuation due to limited events in each bin. This is especially true in the high mass tail. However, what we expect for the background shape is a smooth curve, instead of a fluctuated histogram.

The character of the QCD background shape is its sharply rising edge and fast decaying tail. There exist some functions for fitting the whole region [68]. However, these functions put more emphasis in the low transverse mass region, where there are large number of events in each bin, and do not fit very well in the high end region. In this measurement, we are more interested in the high tail region. There are many events in the low region and fitting programs give most weights in this area and does not fit very well the high end. For this analysis, we decide to use only the high end of the QCD background for fitting.

We use an exponential function to fit the QCD shape in the high end:

$$f_{fitting\ QCD} = EXP(a_0 + a_1 * x + a_2 * x^2 + a_3 * x^3) \quad (4.13)$$

After fitting the QCD background shape with this function, we obtain the parameters  $a_0, a_1, a_2$  and  $a_3$  and their uncertainties, shown in Table 4.3. From the fitting function, we take the area under each bin as the fitting background. Some bins are outside the fitting region and we take the original values. The fit background is shown in Figure 4.3.

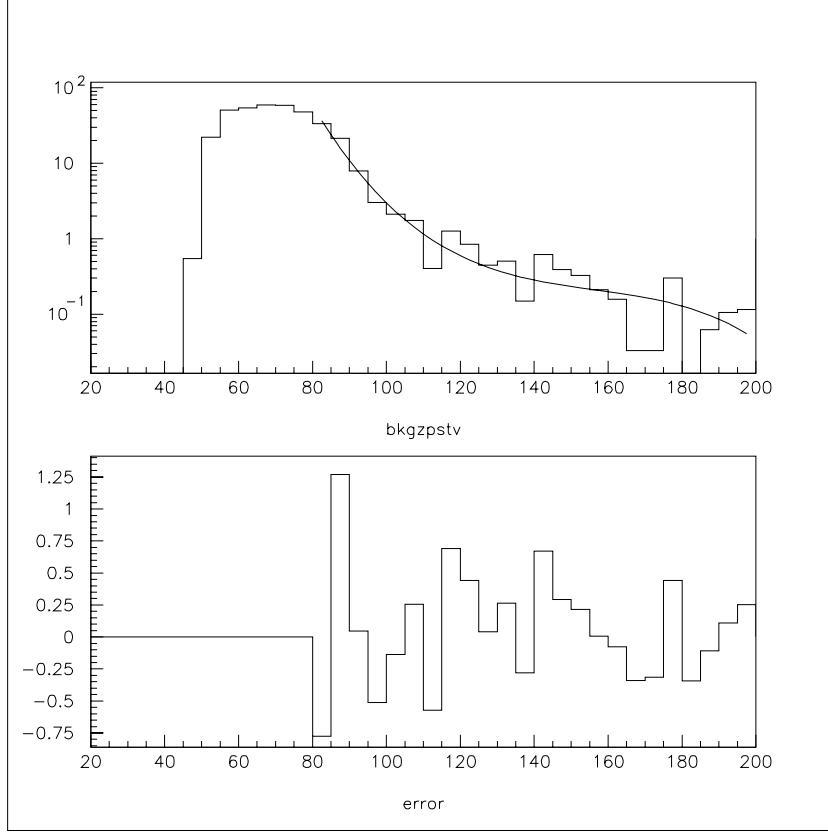


Figure 4.3: In the first plot, QCD background is fit in the high end  $m_t(W) > 80 \text{ GeV}$  with function  $f = \exp(a_0 + a_1 * x + a_2 * x^2 + a_3 * x^3)$ . The fit background is taken to be the area under the fitting curve. The second plot show (background(original) - background(fit))/error, where error is taken to be the square root of background(fit).

Parameter	Fitting Value	Uncertainty
$a_0$	39.153	0.12401E-01
$a_1$	-0.75100	0.43839E-03
$a_2$	0.47087E-02	0.40631E-05
$a_3$	-0.10046E-04	0.94607E-08

Table 4.3: QCD background fitting parameters and their uncertainties.

For the uncertainties, we consider two factors. One is due to the total background number fluctuation. Because of the error on electron and jet efficiencies, there is an error in the inclusive background number. We take one standard deviation to form the up and low boundaries as background fluctuations and scale the fitting background up or down by a factor, which will make the total background equal to the up or low boundaries of the background.

The other uncertainty is due to the fitting. There are uncertainties on the fitting parameters  $a_0, a_1, a_2$  and  $a_3$ . We take each parameter from its upper and lower limit by one standard deviation and generate a histogram. For 4 parameters, there are 8 histograms. We will use them later to calculate the  $W$  decay width uncertainty due to variation of these fitting parameters.

### 4.3 $Z \rightarrow ee$ Background

The  $Z \rightarrow ee$  background is determined by using events generated by the Monte Carlo. If one electron is not identified and shows up as missing energy, it will have the same signature as  $W \rightarrow e\nu$  and could enter our  $W \rightarrow e\nu$  data sample. A total of 8870  $Z \rightarrow ee$  events are generated by ISAJET and processed through DØRECO. The  $W$  boson selection cuts are then applied to the sample events and

the residual number of events is found to be 48 events. The shape of the  $Z \rightarrow ee$  background in transverse mass is shown in Figure 4.4.

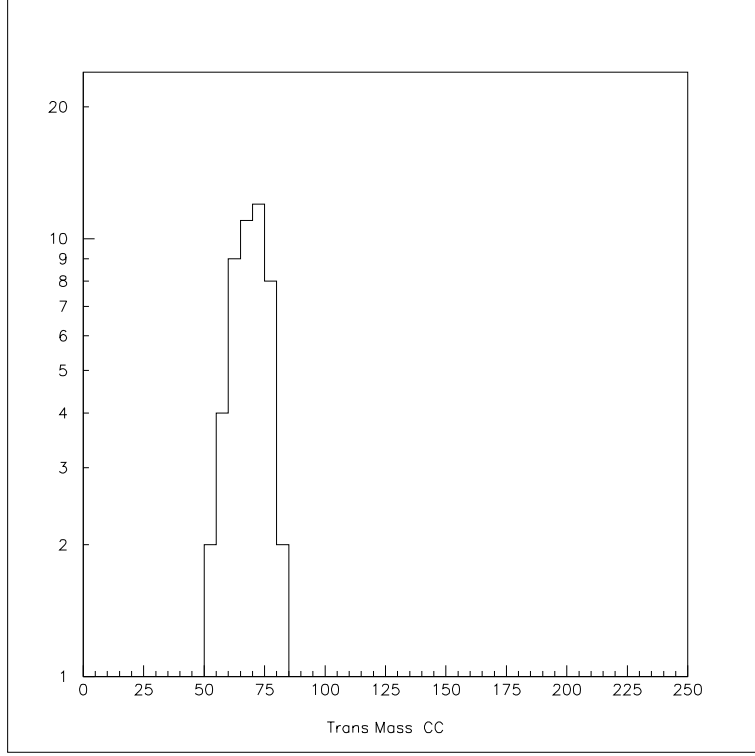


Figure 4.4: The  $Z \rightarrow ee$  background distribution as a function of the transverse mass.

To normalize it to the number of events in the  $W$  sample, we use the luminosity of the data and number of events from the MC sample. The normalized  $Z \rightarrow ee$  number of events is given by

$$N_{bkg}^{Z \rightarrow ee} = N_{MC}^{Z \rightarrow ee} \cdot \frac{\mathcal{L}^{data}}{\mathcal{L}^{MC}} \quad (4.14)$$

where  $N_{MC}^{Z \rightarrow ee}$  is the number of events in the MC sample that survive the  $W$  selection cuts,  $\mathcal{L}^{data}$  is the luminosity of the data and  $\mathcal{L}^{MC}$  is the effective luminosity of the MC sample, which is  $\mathcal{L}^{MC} = N_{total}^{MC} Z \rightarrow ee / \sigma_Z$ . The  $N_{total}^{MC} Z \rightarrow ee$  is the total  $Z \rightarrow ee$  event in the MC sample and  $\sigma_z$  is the  $Z$  cross section measured by DØ [67]. We estimate a total of 102  $Z \rightarrow ee$  background events in the  $W$  sample.

## 4.4 $W \rightarrow \tau\nu$ Background

$W \rightarrow \tau$  events where the  $\tau$  subsequently decays into an electron and two neutrinos are indistinguishable from  $W \rightarrow e\nu$  events. This background can only be estimated from Monte Carlo simulations. The tau background is calculated using the CMS Monte Carlo: a fraction of events is generated as tau's, decayed electronically and acceptance and fiducial cuts are applied to the decay electron in the same manner as for  $W \rightarrow e\nu$  events. The acceptance for  $W \rightarrow \tau\nu \rightarrow e\nu\nu$  is reduced by the branching fraction  $B(\tau \rightarrow e\nu\nu) = 18\%$  [69]. The kinematic acceptance is further reduced by the  $E_T$  cut on the electron since the three body decay of the  $\tau$  leads a very soft electron  $E_T$  spectrum compared to that from  $W \rightarrow e\nu$  events (see figure 4.5).

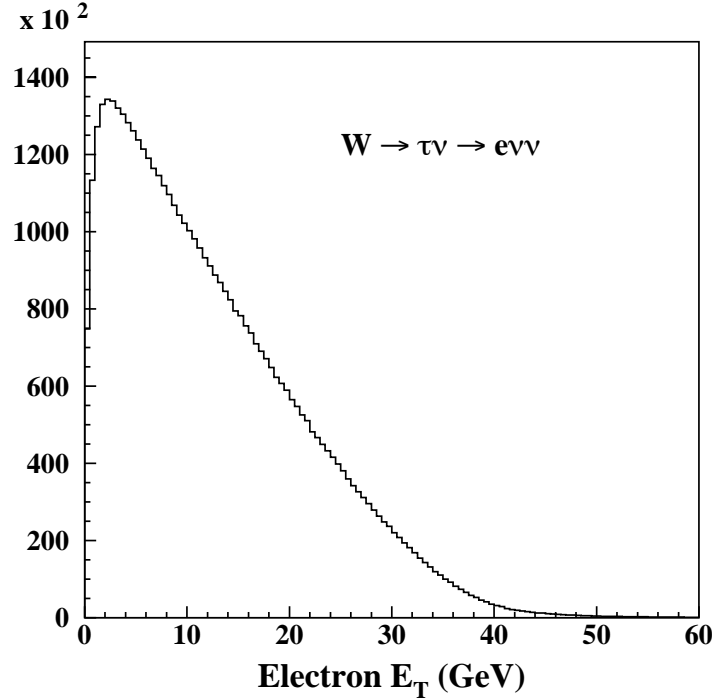


Figure 4.5: Electron  $E_T$  spectrum for  $W \rightarrow \tau\nu \rightarrow e\nu\nu$  events (from CMS).



# Chapter 5

## $W$ Width Measurement

After the  $W$  events are selected and backgrounds are estimated, the next step is naturally to measure the  $W$  decay width. To measure  $\Gamma_W$ , a very important tool, Monte Carlo, is used to generate a set of templates to compare with data. The maximum likelihood method is used to extract the  $W$  decay width. To complete the measurement, a thorough study of systematic uncertainty is included.

### 5.1 Monte Carlo

The kinematics of  $W$  boson production and decay are simulated using the fast Columbia-Michigan State (CMS) Monte Carlo generator [61]. CMS was initially written at DØ for the  $W$  mass analysis and has since been used in the measurement of the inclusive  $W$  and  $Z$  cross section [70], the measurement of the transverse momentum distribution for the  $W$  and the  $Z$  boson [71], angular distribution of  $W$  decay [72] and differential cross section of  $W$  [60].

CMS is not a full parton level generator. The kinematic distributions for various processes have to be produced using a full triple differential cross section generator like Resbos [73]. The parton level boson cross section enters CMS as a grid of

boson rapidity versus transverse momentum. The invariant  $W$  mass enters CMS as a Breit-Wigner function that depends on the center-of mass  $s$  of the quark-antiquark system. CMS subsequently decays the boson and smears the resulting particles by taking into account detector resolution effects. Acceptance effects are modeled by a parameterized detector simulation. A detailed description of the CMS Monte Carlo program is given in [74, 75, 76]. The following several sections will put emphasis on these parts that are important to this analysis.

### 5.1.1 $W$ Boson Generation

Ideally, vector boson production is modeled by a fully differential cross section:

$$\frac{d^5\sigma}{dm dp_T dy d\phi d\epsilon} \quad (5.1)$$

where  $m$ ,  $p_T$ ,  $y$ ,  $\phi$ , and  $\epsilon$  are the vector boson mass, transverse momentum, rapidity, azimuthal angle, and polarization, respectively. In the CMS Monte Carlo, this cross section is factorized into four pieces:

$$\frac{d^5\sigma}{dm dp_T dy d\phi d\epsilon} = \frac{d\sigma}{dm} \cdot \frac{d^2\sigma}{dp_T dy} \cdot \frac{d\sigma}{d\phi} \cdot \frac{d\sigma}{d\epsilon} \cdot \quad (5.2)$$

This factorization is not strictly correct, but correlations between the various terms are small. The  $\phi$ -term is simple: Vector bosons are produced uniformly in  $\phi$  so that CMS just picks a random  $\phi$  value in  $[0, 2\pi]$ . The polarization of a  $W$  boson is defined by its charge.

The other two parts of the cross section in equation 5.2 will be discussed below.

### 5.1.2 $d\sigma/dm$ Calculation

The  $W$  mass is modeled by a relativistic Breit-Wigner with an  $\hat{s}$ -dependent width modified by a parton luminosity term, which models the dependence of the mass

on the momentum distribution of the quarks:

$$\frac{d\sigma}{dm} = PL(m) \cdot \frac{m}{(m^2 - M^2)^2 + m^4 \Gamma^2 / M^2} , \quad (5.3)$$

where  $PL(m)$  is the parton luminosity term,  $m$  is the mass of the vector boson being generated, and  $M$  and  $\Gamma$  are the boson's true mass and natural width, respectively.

$PL(m)$  depends on the structure function and is well modeled by the following function:

$$PL(m) = \frac{e^{-\beta \cdot m}}{m} , \quad (5.4)$$

where the  $\beta$  is called parton luminosity slope. The value of  $\beta$  depends upon the rapidity distribution of the  $W$  boson, which is constrained by the kinematic and fiducial cuts applied to the leptons.

Since the CMS was produced for  $W$  mass analysis, there exist  $\beta$ 's for some of the PDFs from the end-cap calorimeter(EC)  $W$  mass analysis. These  $\beta$ 's are calibrated for EC  $W$  events, where electron cuts are different from that of a CC electron. To test if these  $\beta$ 's are valid for this analysis,  $W$  events with different PDF are generated and the unsmeared quantities of  $W$ , electron and neutrino are compared. It was found that the difference due to different PDFs is very small for mass distribution and hence transverse mass. However, the beta value has a large effect on the  $W$  mass and transverse mass  $m_T$  distribution, especially in the high end region. Around the peak of the  $W$  mass, the difference is small, which means that it will not have a large error in mass measurement. In the region away from the peak, the difference is obvious. This is clearly shown in Figure 5.1 and Figure 5.2. It is easy to see that  $\beta$  is very critical for our analysis.

To find the  $\beta$  value for this measurement, the RESBOS program is used to generate n-tuples with different PDFs, such as CTEQ4M and MRSA. After applying the fiducial cuts, described in the  $W$  event selection, the  $W$  mass spectrum is

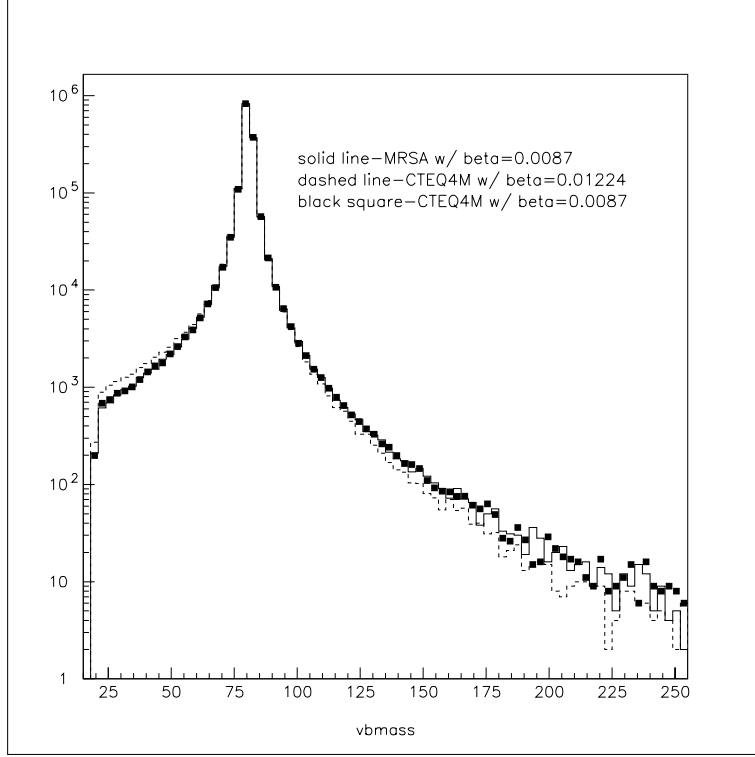


Figure 5.1: The unsmeared  $W$  mass distribution for different PDFs and  $\beta$ 's. For different PDFs of CTEQ4M [77] and MRSA with the same  $\beta$  (solid line and black square), the spectrum is nearly identical. However, for the same PDF of CTEQ4M (solid line and dashed line) with different  $\beta$ 's,  $W$  mass distributions have an obvious difference, especially in the low mass region and high mass tail.

reconstructed and fit with the function:

$$\frac{d\sigma}{dQ} = \frac{e^{-\beta Q}}{Q} \frac{Q^2/M_W^2}{(Q^2 - M_W^2)^2 + Q^4\Gamma_W^2/M_W^2} \quad (5.5)$$

From fitting, both beta and its uncertainty are determined, which is listed in Table 5.1. The different fitting regions will give different beta values. The fitting region is selected by choosing the one with smallest chi-square. The fitting plots are shown in Figure 5.3 and Figure 5.4.

Our fitting result for beta of MRSA is  $0.00852 \pm 0.00013$ . As a comparison, the

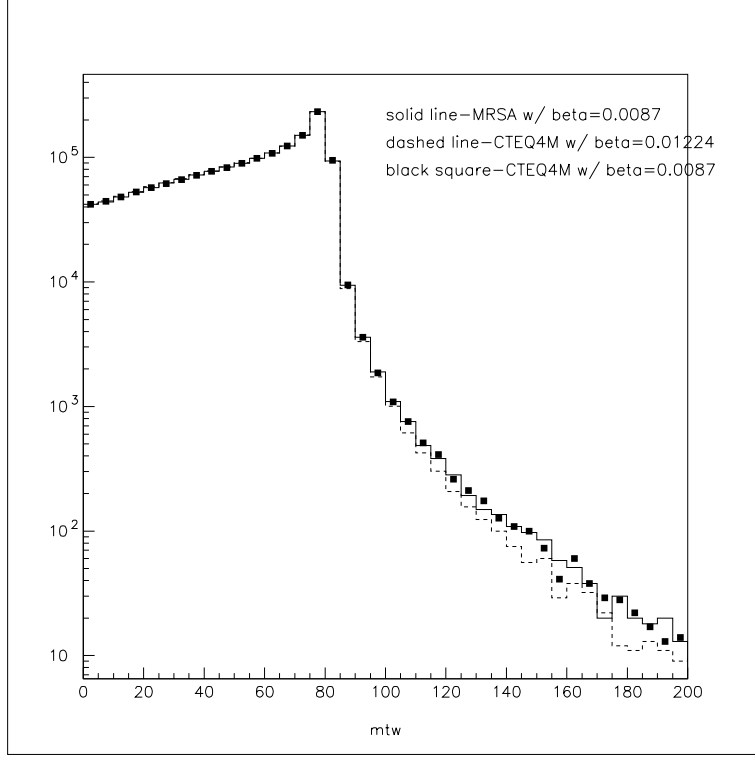


Figure 5.2: The transverse mass distribution for different PDFs and  $\beta$  values. In the low end of the spectrum, all distributions are close. The difference appears in the high end. For different PDFs of CTEQ4M and MRSA with the same  $\beta$  (solid line and black square), the spectrum is nearly identical. But for the same PDF of CTEQ4M (solid line and dashed line), the difference in  $\beta$  causes the obvious different distributions.

beta of MRSA in the published  $W$  CC mass paper is 0.0086. The fitting result in  $W$  EC mass measurement for  $W$  CC events is 0.00836. The difference between this analysis and those of  $W$  mass results are 0.00008(0.92%) and 0.00016(1.8%) respectively. They are in good agreement. The fitting of beta for CTEQ4M is  $0.00852 \pm 0.00012$ .

<b>pdf</b>	$\beta(\text{GeV}^{-1})$	uncertainty
MRSA	0.00852	0.00012
CTEQ4M	0.00852	0.00013

Table 5.1: Patron luminosity slope  $\beta$  in the  $W$  production model.

### 5.1.3 $d^2\sigma/dp_t dy$ Calculation

As already discussed in Chapter 1, at lowest order the  $W$  boson is produced through a Drell-Yan diagram as shown in figure 5.5.  $W$  bosons produced this way have longitudinal momentum due to the momentum imbalance of the incoming quarks but no transverse momentum since the momenta of the proton and antiproton are collinear with the beam axis. The fact that  $W$  bosons are produced with finite transverse momentum is attributed to contributions from higher order diagrams as shown in figure 5.6. The additional quark- or gluon-jet recoils against the  $W$  boson and carries away transverse momentum equal and opposite to  $p_T^W$ .

In CMS, as mentioned before, the differential cross section in  $W$  boson  $p_T$  and  $y$  enters the CMS Monte Carlo as a two dimensional histogram, which is called the grids file. This histogram was generated according to theory calculations including perturbative and non-perturbative effects. For large  $p_T^W$  (above 50 GeV), fixed order perturbation theory describes the production of vector bosons well. A calculation to next-to leading order ( $\mathcal{O}[\alpha_s^2]$ ) in perturbative QCD [78] is used in this regime. For  $p_T^W < 20$  GeV, a resummed calculation [79] is used. The  $p_T$  distributions from both theories are matched at intermediate  $p_T^W$  to ensure a smooth transition.

The resummed calculation is performed in impact parameter space where the impact parameter  $b$  is the Fourier-transformed variable to  $p_T$ . The double differ-

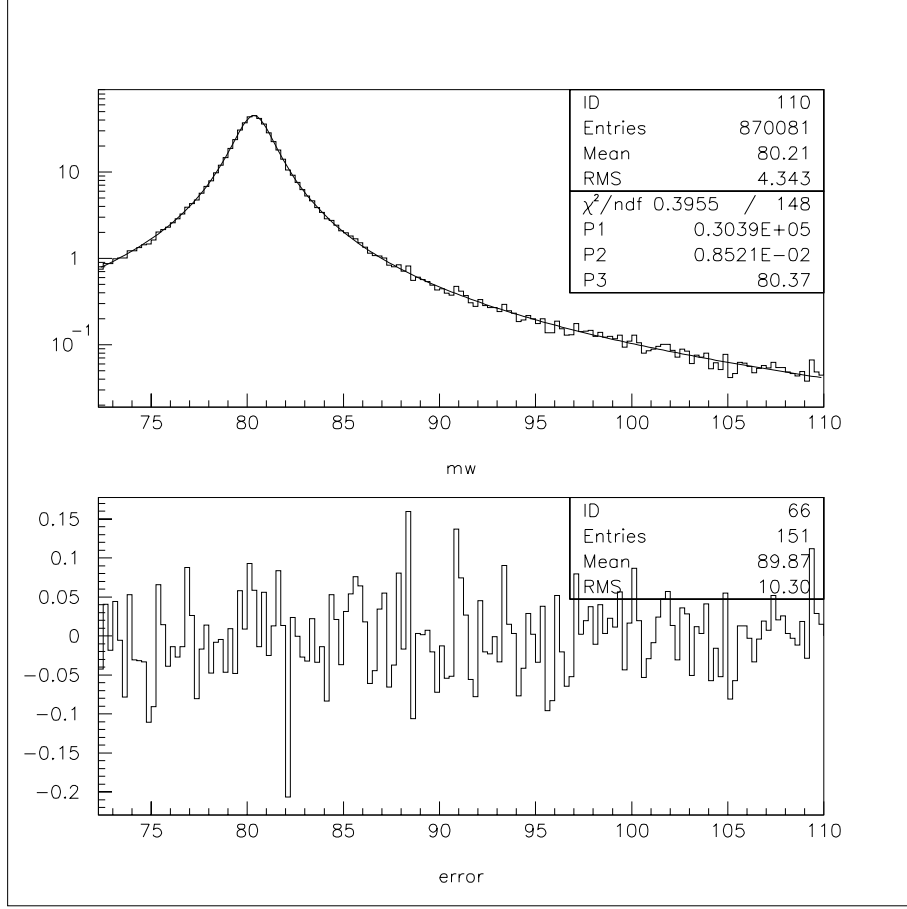


Figure 5.3: The luminosity fitting for MRSA. The  $W$  mass spectrum is generated by applying lepton fiducial cuts to the data made by RESBOS. The fitting function is Breit-Wigner skewed by  $e^{-\beta \cdot mass}/mass$ . The fitting parameters are normalization factor(p1), beta(p2) and  $W$  mass(p3). The fitted  $W$  mass is 80.374, which is a good check for this fitting. The chi-square is 0.3955 for 148 degrees of freedom. The fitting region is 72 GeV to 110 GeV. The result is  $\beta = 0.00852 \pm 0.00012$ . The second plot shows the  $(data-fit)/\sqrt{fit}$  in each bin.

ential cross section for vector boson production is written as:

$$\frac{d^2\sigma}{dp_T dy} \propto \int \frac{d^2b}{(2\pi)^2} e^{i\vec{b} \cdot \vec{p}_T} W(b_\star) e^{-S_{NP}(b)} , \quad (5.6)$$

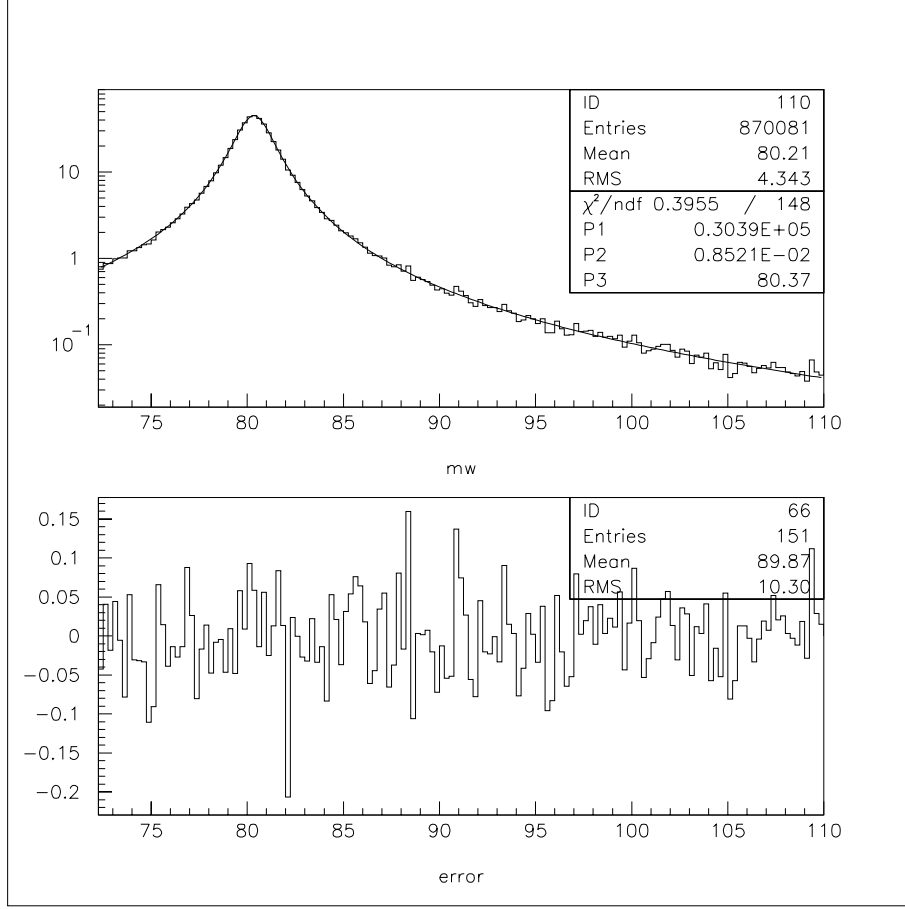


Figure 5.4: The luminosity slope fitting for CTEQ4M. The method and procedure is the same as that for MRSA. The chi-square is 0.3955 for 148 degrees of freedom. The fitting region is 72 GeV to 110 GeV. The fitting result is  $\beta = 0.00852 \pm 0.00013$ . The second plot shows the (data-fit)/sqrt(fit) in each bin.

where  $b_\star$  is a function of  $b$  which handles the divergence at large  $b$  or small  $p_T$  by introducing a cutoff  $b_{max}$ :

$$b_\star = \frac{b}{\sqrt{1 + b^2/b_{max}^2}} . \quad (5.7)$$

The function  $W(b_\star)$  describes the perturbative part of the calculation while non-perturbative effects at large  $B$  are contained in the function  $S_{NP}(b)$ , which in



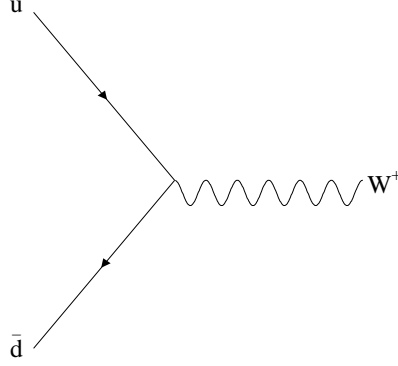


Figure 5.5: Lowest order (Drell-Yan) diagrams for  $W$  production.

the parameterization used by Ladinski and Yuan is written as:

$$S_{NP} = g_1 b^2 + g_2 b^2 \ln \left( \frac{Q}{2Q_o} \right) + g_1 g_3 \ln(100 x_A x_B) , \quad (5.8)$$

with  $Q_o$  an arbitrary momentum scale,  $Q$  the mass of the vector boson, and  $x_A$ ,  $x_B$  the momentum fractions of the incoming quarks. The parameters  $g_1$ ,  $g_2$ , and  $g_3$  are determined by Ladinsky and Yuan. They fit their hypothesis to the available Drell-Yan and  $Z$  production data and obtain the values:

$$g_1 = 0.11^{+0.04}_{-0.03} \text{ GeV}^2 \quad g_2 = 0.58 \pm 0.06, \text{ GeV}^2 \quad g_3 = -1.5^{+0.1}_{-0.1} \text{ GeV}^{-1} , \quad (5.9)$$

where  $Q_o = 1.6 \text{ GeV}$ , and  $b_{max} = 0.5 \text{ GeV}^{-1}$  are chosen. It has been shown [75] that  $g_2$  is the dominant parameter. Its error will change the histogram file which enter into CMS MC and eventually cause the uncertainty in the fitting result. This effect will be under study when the systematic uncertainty is calculated. The above value for  $g_2$  is from the new  $D\bar{O} \ Z \rightarrow ee$  data [80, 71].

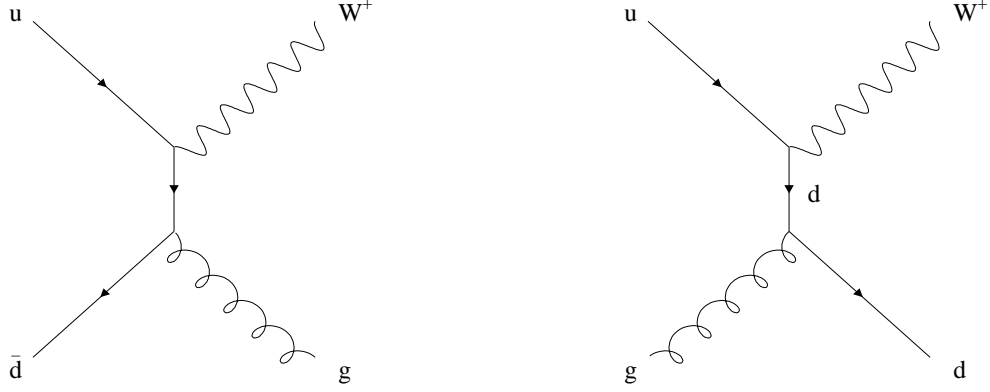


Figure 5.6: Higher order diagrams for  $W$  production: (left) the initial state gluon radiation process and the (right) Compton process.

#### 5.1.4 $W$ Boson Decay

The decay of the  $W$  boson is performed in the rest frame of the  $W$ . The decay products, leptons, are produced back-to-back in the rest frame. Each lepton is produced with momentum equal to  $1/2$  the boson mass. The decay angle of the lepton is generated first in the rest frame and subsequently boosted to the lab frame. Figure 5.7 shows the leading order diagram for  $W \rightarrow e\nu$  decay.

#### 5.1.5 QED Radiative Decays

Final state radiation (Bremsstrahlung) of a photon from the decay electron is a correction to the lowest order decay process that has to be taken into account since the photon can lower the momentum of the electron. A calculation by Berends and Kleiss [81] to  $\mathcal{O}[\alpha_{EM}]$  concludes that in 31% of the  $W$  decays, a photon with energy above 50 MeV is radiated. In CMS, these photons are generated for the

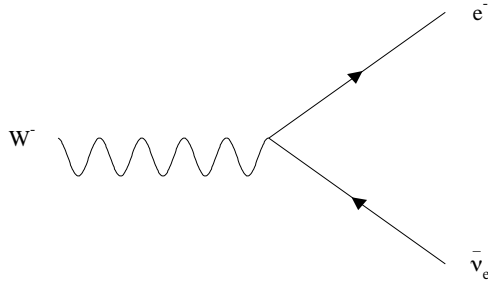


Figure 5.7: Leading order diagrams for  $W \rightarrow e\nu$  decays.

correct fraction of events, subsequently the electron, the neutrino, and the photon are boosted into the lab frame. If the electron and photon are close in  $\eta \times \phi$  space ( $\mathcal{R} = \sqrt{\Delta\phi^2 + \Delta\eta^2} < 0.3$ ), they are merged, otherwise the photon is treated as a separate object.

### 5.1.6 Simulation of $W \rightarrow \tau\nu \rightarrow e\nu\nu$

$W \rightarrow \tau\nu$  decays where the tau subsequently decays electronically are indistinguishable from  $W \rightarrow e\nu$  events: both are characterized by an electron and large missing  $E_T$  in the final state. The CMS Monte Carlo produces  $W \rightarrow \tau\nu \rightarrow e\nu\nu$  events with a branching ratio to account for this production mode. The production kinematics for  $W \rightarrow \tau\nu$  events are exactly the same as the ones for  $W \rightarrow e\nu$ . Kinematic differences come in through the subsequent three body decay  $\tau \rightarrow e\nu\nu$ , which is performed in the rest frame of the  $\tau$ . The energy and angular correlations of the

electron with respect to the  $\tau$  polarization vector are correctly taken into account by selecting them from a two-dimensional distribution obtained from  $\tau \rightarrow e\nu\nu$  decays generated with the ISAJET [82] Monte Carlo.

### 5.1.7 Detector Simulations

In CMS, detector simulation takes a parameterized model to simulate the detector response and resolution to obtain the electron and recoil momentum.

For calorimetric measurements, the determination of the overall energy scale relies on the particles of known momenta and on the reconstruction of the mass of well known particles. The calibration of the energy scale of the DØ electromagnetic calorimeters was previously determined [74, 62, 83, 84, 85] using test beam data,  $Z$ ,  $\pi^0$  and  $J/\psi$  decays.

In the CMS parametric simulation, the EM energy scale was implemented with the assumption that the measured energy, denoted by  $E_{measured}$ , is related to the originally generated energy,  $E_{true}$ , by a scale  $\alpha_{EM}$  and an offset  $\beta_{EM}$

$$E_{measured} = \alpha_{EM} E_{true} + \beta_{EM} \quad (5.10)$$

The  $Z \rightarrow ee$  events are used to constrain the energy scale, as it was done in the  $W$  mass analysis [62, 61, 63]. The dielectron invariant mass  $M_{ee}$  spectrum from  $Z \rightarrow ee$  data events and CMS Monte Carlo simulations are used to determine these EM scale parameters. This analysis was based on  $Z$  boson events with both electrons in the central region (CC–CC events).

A set of sample  $Z \rightarrow ee$  events with different inputs  $\alpha_{EM}$  is generated and the invariant mass distribution,  $M_{ee}$ , is reconstructed. The resulting  $M_{ee}$  spectrum is fitted using the sum of a convolution of the  $Z$  boson Breit-Wigner resonance with a Gaussian resolution function and a linear background contribution. Figure 5.8 shows the procedure for  $\alpha_{EM} = 0.95$  with  $M_{ee} = 87.00$ .

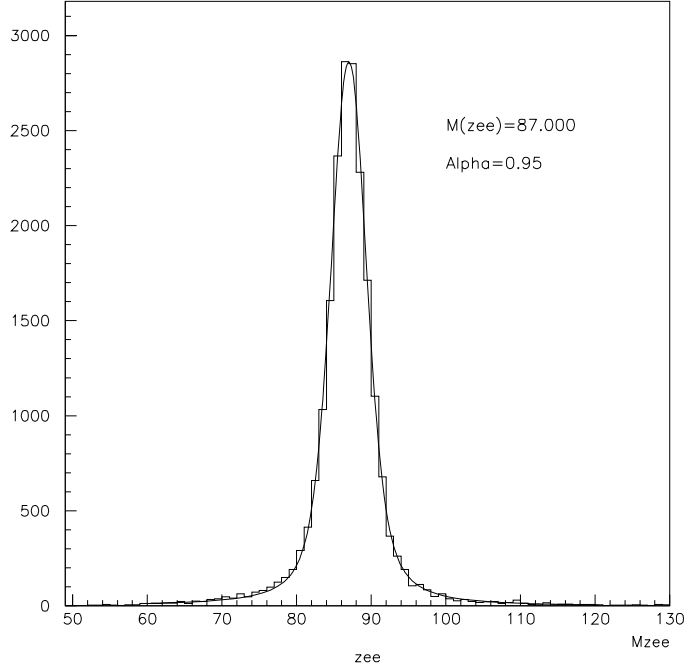


Figure 5.8: Invariant dielectron mass distribution of  $Z \rightarrow ee$  MC simulation events. The  $M_{Zee}$  is obtained by fitting the histogram with the sum of a Breit-Wigner convoluted with a Gaussian and a linear background contribution. The histogram is the MC sample. The curve is the fitting.

The fitting peak  $M_{ee}$  as a function of the input scale  $\alpha_{EM}$  is shown in Figure 5.9. The  $M_{ee}$  vs.  $\alpha_{EM}$  is fitted with a linear function. The EM scale  $\alpha_{EM}$  is determined so that the generated CMS dielectron invariant mass  $M_{ee}$  is equal to that in  $Z \rightarrow ee$  data, which is 87.40 GeV. This leads to the result:

$$\alpha_{EM} = 0.9547 \quad (5.11)$$

Compared to the  $\alpha_{EM} = 0.9545$  that was used in the published  $W$  mass analysis [63], the result is consistent. For this analysis,  $\alpha_{EM} = 0.9545$  and other detector simulation parameters from the  $W$  mass analysis are used so as to be consistent

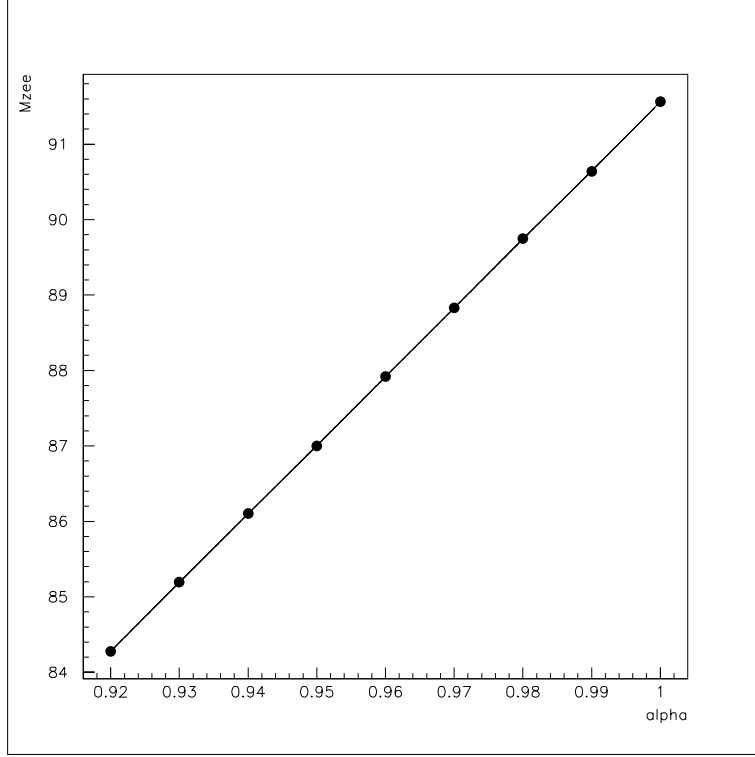


Figure 5.9: Invariant dielectron mass of  $Z \rightarrow ee$  as a function of input  $\alpha_{EM}$ . The black dots are data that was determined by fitting the MC sample. The line is the fitted with slope=90.986 and offset=0.57154.

with their results. The invariant mass distribution of  $Z \rightarrow ee$  data and its fitting with comparison to MC at  $\alpha_{EM} = 0.9545$  is shown in figure 5.10.

### 5.1.8 Comparison of MC and Data

After all simulation parameters are defined, it is critical to compare the data to that generated by the CMS MC. The purpose is to make sure that the CMS MC simulation represents the true physics process. The plots are shown in Figure 5.11 and Figure 5.12. The first plot is the comparison of all data events to the CMS MC sample. The second one is the comparison for these data and MC events only with  $m_T > 90 GeV$ . The data and CMS are in good agreement in both plots. This

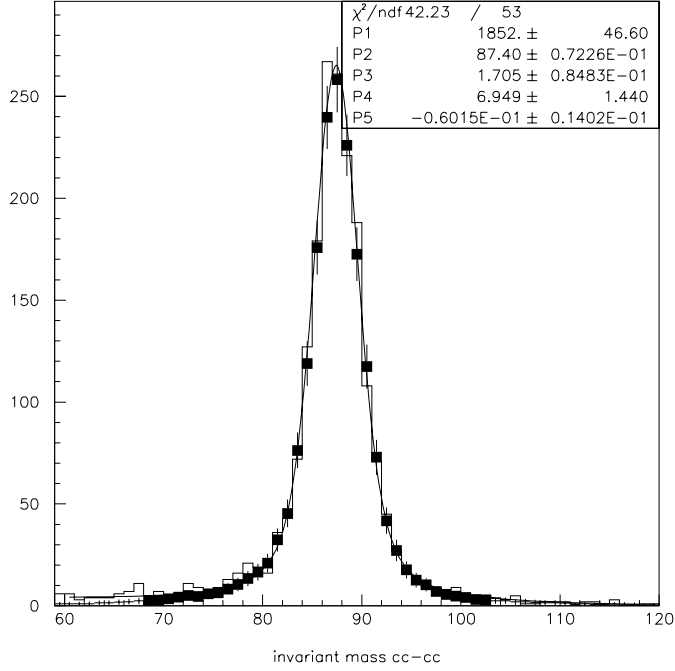


Figure 5.10: Comparison of invariant dielectron mass of  $Z \rightarrow ee$ , its fitting and MC simulation. The histogram is  $Z \rightarrow ee$  from data. The curve is the fitting. The black square with error bar on it is the MC simulation with  $\alpha_{EM} = 0.9545$ . They are normalized to the number of events in the data.

means that we understand the data very well and CMS MC simulates the physics process as well too, both in  $p\bar{p}$  collision and in detector response.

## 5.2 Determination of the $W$ Boson Width

We determined the  $W$  width by performing binned log-likelihood fits of the transverse mass distribution in the data to the Monte Carlo templates with different values of  $\Gamma(W)$ .

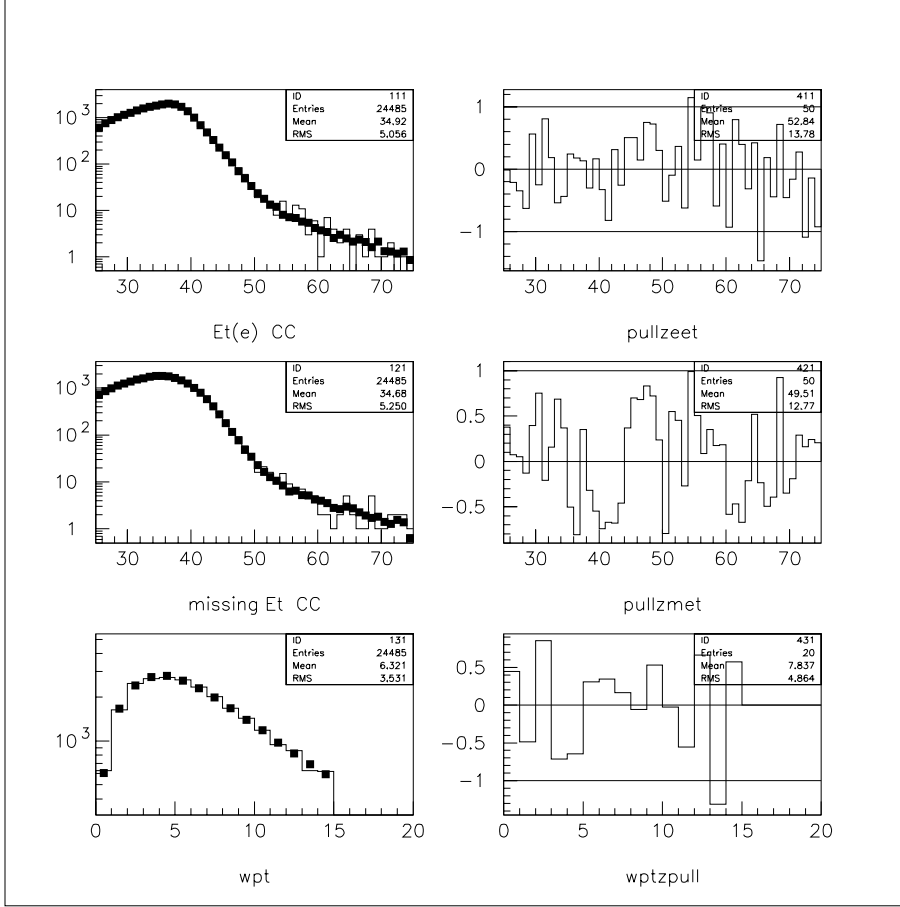


Figure 5.11: The comparison of data to CMS. The left column is the data overlap with CMS MC for electron  $E_t$ , missing  $E_t$  and  $W$   $p_t$ . The solid line is for the data and the black square is for the MC sample. The CMS MC samples are generated with  $\Gamma(W) = 2.050 \text{ GeV}$  and normalized to the number of events in the data. There is no background added to the MC sample. The right column is  $(\text{data} - \text{MC})/\text{error}$  in each bin, where error is taken to be  $\sqrt{\text{MC}} + \sqrt{\text{data}}$  in each bin.

### 5.2.1 Log-likelihood

The log-likelihood is the product of the probabilities of the events coming from a given distribution. The likelihood  $(L(\Gamma))$  as a function of a given width  $\Gamma$  is



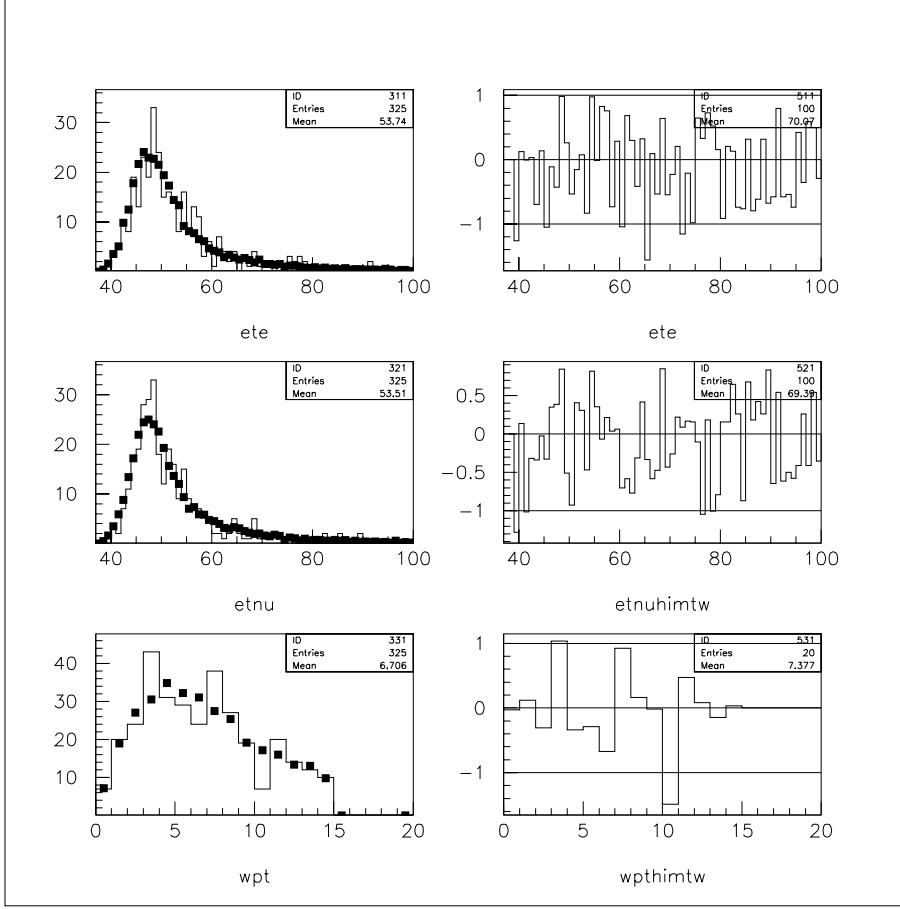


Figure 5.12: The comparison of data to CMS. Everything is the same as the previous plots, except the data events and MC sample are only these events with  $m_T > 90 GeV$ .

$$L(\Gamma) = \prod_{event} P_i(\Gamma) \quad (5.12)$$

where  $P_i(\Gamma)$  is the probability of each event. In the case of binned data, it is the probability of each bin at given event number for a width  $\Gamma$ . Usually, the

$\log(\text{likelihood})$  (which is  $\log \mathcal{L}$ ) is used and given by

$$\mathcal{L} = \ln L \quad (5.13)$$

$$= \sum_{bin} \ln P_i(\Gamma). \quad (5.14)$$

The width is given by  $\Gamma$ , at which  $\mathcal{L}$  is maximum:

$$\Gamma_W = \Gamma(\mathcal{L} = \mathcal{L}_{maximum}) \quad (5.15)$$

$$= \Gamma\left(\frac{\partial \mathcal{L}}{\partial \Gamma} = 0\right) \quad (5.16)$$

The statistical error on  $\Gamma(W)$  is the region allowed by the maximum of  $\mathcal{L}$  to decrease 1/2 a unit. The probability at a given  $i^{th}$  bin is a Poisson distribution and therefore the log-likelihood is

$$\ln \mathcal{L} \equiv \sum_i^{bin} [x_i \cdot \ln \mu_i - \mu_i - \ln(x_i!)], \quad (5.17)$$

where the sum is over the bins in fitting region of transverse mass distribution,  $x_i$  is the number of events observed in each transverse mass bin from data, and  $\mu_i$  is the expected number of events in each bin  $\mu_i = bkg_i + W_i$ , where  $bkg_i$  is the background in the  $i^{th}$  bin and  $W_i$  is the MC data in the  $i^{th}$  bin.

### 5.2.2 Fitting

The MRST [86] PDF is used to generate the MC event sample. The choice of particular PDF is consistent with the  $W$  mass analysis. A set of MC templates with different  $\Gamma_W$  starting from 1.55 GeV to 2.75 GeV with a step of 50 MeV are generated. These MC events are normalized to  $24479 - 469.11 = 24009.89$ , where 24479 is the total number of  $W$  events and 469.11 is the total number of background events in the region of 0 to 200 GeV for  $m_T$ .

Fundamentally, we can take different parts of the transverse mass spectrum for the likelihood fitting. As we can expect, different fitting regions will give different

Fitting Region $m_T(GeV)$	Number of Events	$\Gamma$ ( $GeV$ )	Stat. Error ( $GeV$ )	$\chi^2$ per DOF	KS
All(0-200)	24479	2.175	+0.112/-0.108	1.159	0.596
65-200	16450	2.174	+0.112/-0.109	1.199	0.440
75-200	6286	2.217	+0.118/-0.115	1.265	0.951
85-200	713	2.208	+0.124/-0.120	1.177	0.721
90-200	319	2.231	+0.145/-0.138	1.177	0.434
95-200	196	2.285	+0.179/-0.167	1.177	0.251

Table 5.2: The maximum likelihood fitting results of  $W$  decay widths for different fitting regions and their statistical uncertainties. The chi-square and Kolmogorov-Smirnov(KS) are also listed.

results and these results should be consistent with each other. Since the decay width is sensitive to the high tail, as is shown in Chapter 1, we expect that the fitting region with only the high end will give similar fitting results as that with the whole fitting region. However, a smaller fitting region includes less events for fitting which results in larger statistical uncertainty. For the purpose to study statistical and systematic uncertainties, we take different fitting regions and the fitting results are listed in Table 5.2.

From the table, it is clear that the statistical error is larger for a narrower fitting region due to a smaller number of events in the region. There is a fluctuation in the fitting results, but they are within their statistical error and consistent with each other. In the table, the  $\chi^2$  and Kolmogorov-Smirnov(KS) test are listed for different fitting regions.

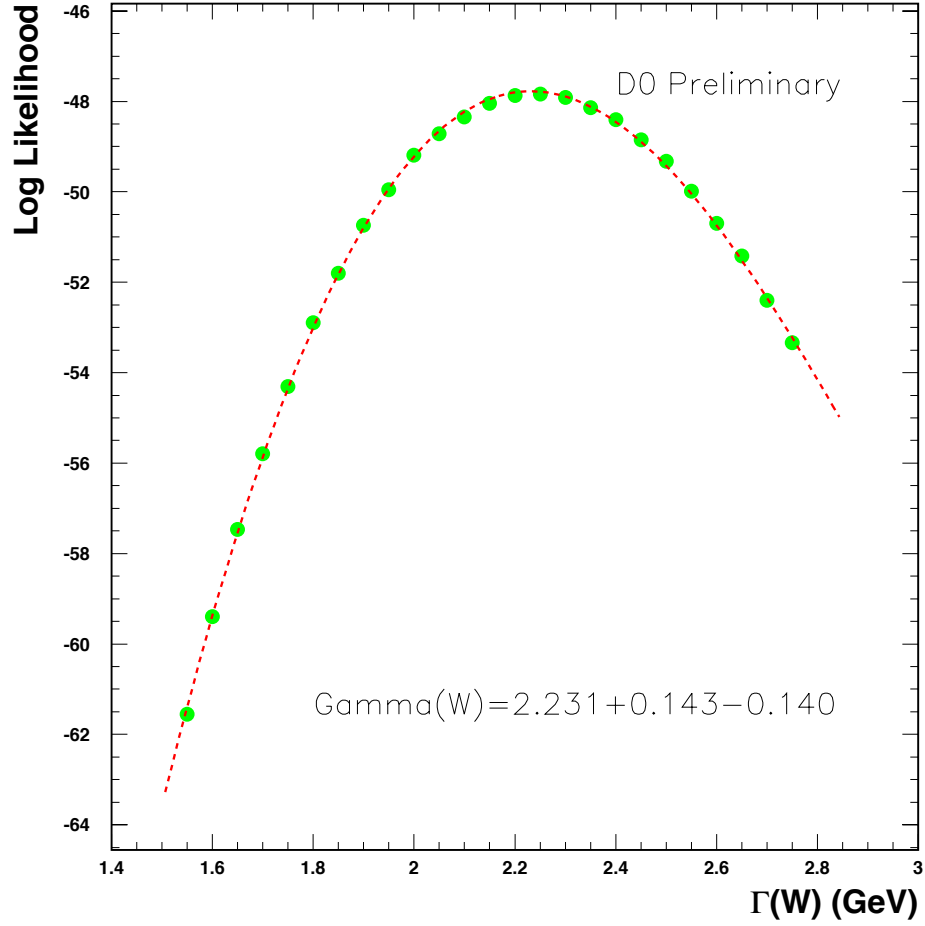


Figure 5.13: Results of the log-likelihood fit of the data to Monte Carlo templates. Monte Carlo templates are generated with values of  $\Gamma(W)$  between 1.55 and 2.75 GeV at 50 *MeV* intervals. Each point represents a log-likelihood fit performed over the range  $90\text{GeV} < m_t < 200\text{GeV}$ . The curve is the best fit of the likelihood points to a fourth order polynomial. The best fitting value is  $\Gamma(W) = 2.231$  GeV. The uncertainty is statistical only.

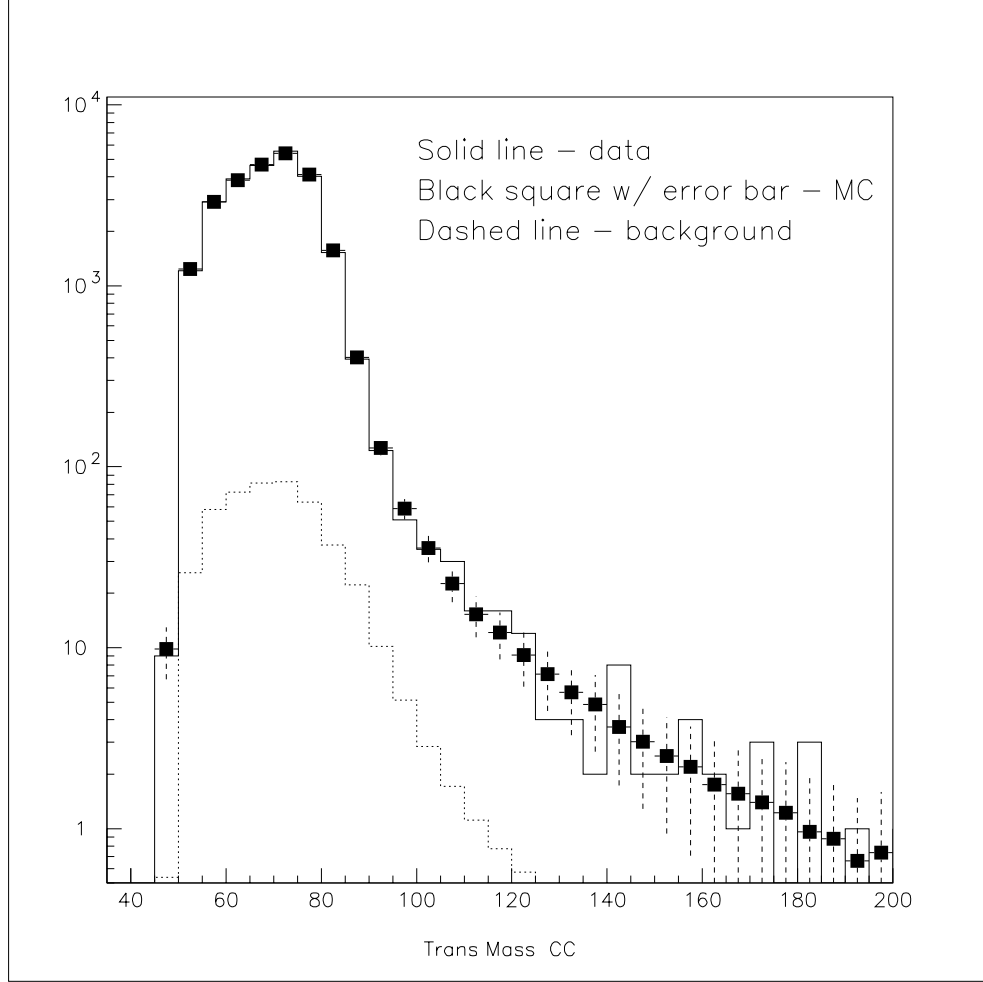


Figure 5.14: Comparison of data to Monte Carlo templates. The solid line of the histogram is data. Black squares with error bars are the MC plus background. Monte Carlo templates are generated with  $\Gamma(W) = 2.231$  GeV and normalized to the data with background subtracted. The dashed line is the background.

Figure 5.13 shows the fitting of likelihood. The log-likelihoods at different decay widths have been fit to a fourth order polynomial and the peak position is determined by finding the maximum of the fitting function. The statistical uncertainty is taken to be the difference of the mean value and the value when likelihood decreases by a half unit. Figure 5.14 shows the data histogram overlapped with

the MC templates and background. The fitting region is from 90 to 200 GeV in transverse mass.

### 5.3 Systematic Uncertainties

The systematic uncertainties in the determination of the  $W$  width are due to effects that could alter the shape of the transverse mass distribution. Basically, every parameter in the MC could cause errors in the final fitting result. The important ones, in addition to the background, are electron energy resolution, hadronic energy resolution, electron energy scale, hadronic energy scale,  $W$  mass variation,  $W$  pt theory( $g_2$ ) pdf's, beta, electron angular calibration and radiative decay.

Generally, to estimate the effects, we allow these input parameters to vary by one standard deviation and generate MC event sample with CMS. With the transverse mass spectrum constructed from the MC sample, we fit it to a standard MC template, which has large MC events. The detailed procedure is the same as was done to determine the mean value of the  $W$  width, except that we use the MC sample to substitute the data sample which has very limited events. If the variation of the  $W$  boson decay width with respect to a parameter is not linear, the error is symmetrized by assigning it the largest value. This estimation method applies to electron energy resolution, hadronic energy resolution, electron energy scale, hadronic energy scale,  $W$  mass variation, beta and radiative decay.

For uncertainties of  $W$  pt theory( $g_2$ ) and pdf's, we need different grid files as input to CMS. The grid file is a 2-D histogram file with respect to  $W$  pt and rapidity. For  $W$  pt theory( $g_2$ ), we use the results from DØ  $Z$  pt analysis, which gives  $g_2 = 0.58 \pm 0.06$ . For uncertainty due to different pdfs, we use MRSA, CTEQ4M and CTEQ5M, with results listed in Table 5.3. For the uncertainty due to different PDF, the largest ones are chosen.

Fitting Region $m_T(GeV)$	MRSA	CTEQ4M	CTEQ5M	$\delta\Gamma$ $MeV$
all(0-200)	+21	-6	-14	21
65-200	+27	-3	-14	27
75-200	+33	+3	-16	33
85-200	+39	+10	-14	39
90-200	+27	+13	0	27
95-200	+14	-1	+5	14

Table 5.3: The uncertainty due to PDFs. The uncertainty listed is the difference between the fitting width with a specific PDF as input for CMS when generating MC data and the width for the main template. The  $\delta\Gamma$  in the last column is the maximum of the differences.

Fitting Region	a1	a2	a3	a4	$\delta\Gamma$
$m_T(GeV)$					$MeV$
all(0-200)	2.3	8.1	7.9	2.2	11.8
65-200	2.4	8.3	7.9	2.0	11.9
75-200	2.5	9.2	8.9	2.9	13.4
85-200	3.5	9.9	9.6	3.0	14.5
95-200	5.1	12.0	12.9	5.6	19.2

Table 5.4: QCD background uncertainties due to fitting parameters in different fitting regions. The uncertainties listed are taken to be the difference between the fitting  $W$  width when a specific parameter is taken at its up or low limit and the mean value when the parameter is taken at its mean value. The total  $\delta\Gamma$  error is the quadratic summation of all the four individual errors.

For errors due to the background, as discussed in the section about background, we have two effects. One is due to the uncertainty of the background event number. We scale up or down the fitting background shape by a ratio, which will make the total background number equal to its upper or lower limit by one standard deviation. The other one is due to the fitting. We change each fitting parameter by its error to generate fitting backgrounds. The difference from the mean value is the uncertainty due to that parameter. There are 4 parameters and results are listed in Table 5.4.



Parameter	Value	$\delta\Gamma(W)$ $M_T$ in (65,200)	$\delta\Gamma(W)$ $M_T$ in (75,200)	$\delta\Gamma(W)$ $M_T$ in (85,200)	$\delta\Gamma(W)$ $M_T$ in (90,200)	$\delta\Gamma(W)$ $M_T$ in (95,200)
EM energy resolution	$0.0115^{+0.0027}_{-0.0036}$	54	50	44	27	23
Hadronic energy resolution	$0.49 \pm 0.14$	71	68	69	55	43
EM energy scale	$0.9545 \pm 0.0008$	41	42	47	41	39
Hadronic energy scale	$0.693 \pm 0.060$	32	31	32	22	39
$W$ pt theory( $g_2$ )	$0.58 \pm 0.06$	27	17	4	12	13
$W$ mass	$80.436 \pm 0.037$	22	25	29	15	17
Background(uncertainty)	$368.19 \pm 31.3$	14	14	14	15	16
Background(fitting)	(4 parameters)	12	13	15	16	19
PDF(MRST, CTEQ5M, MRSA)	-	27	33	39	27	14
Beta(luminosity slope)	$(8.52 \pm 0.12) \times 10^{-3}$	20	21	24	28	36
Radiative decay	$0.3 \pm 0.1$	25	23	16	10	15
e angular calibration	$0.988 \pm 0.001$	17	15	19	9	22
Systematic Error		119.4	115.8	117.9	92.0	93.3
Statistical Error		+112 -109	+118 -115	+124 -120	+145 -138	+179 -167
Total Uncertainty		+164 -162	+165 -163	+171 -168	+172 -166	+202 -191

Table 5.5: The systematic uncertainties and total uncertainty on the  $W$  width measurement for the different fitting regions. The unit of errors is in  $MeV$ .

Table 5.5 lists all the sources of systematic uncertainties for the  $W$  decay width in different fitting regions. The total uncertainty is included when combined with the statistical error.

From this table, we can see that different fitting regions give different systematic uncertainty. Generally, the systematic uncertainty is smaller with less fitting area. But less fitting area also means that less events are included in fitting and statistical uncertainty will be larger, especially in the very high end where the events are very limited and statistical uncertainty increases dramatically. The total uncertainty shows a slow increase from fitting region (65, 200) to (90, 200). The difference is less than 10  $MeV$ . After that, the total uncertainty is very large. Basically we can take any of the fitting regions listed except the last one for our fitting region. Considering the large statistical error in the high tail, we will choose the one with the smallest systematic error, which is from 90 to 200  $GeV$  in transverse mass. This selection is also true for future study when we will have more  $W$  events and statistical uncertainty is not a dominant uncertainty.

## 5.4 Consistency Check of the Result

For our measurement, we have many ways to check the results. This procedure is necessary to make sure our measurement results represent the true physics quantity.

### 5.4.1 Number of Events Ratio

As a good consistency check of our results, we define a ratio  $R$ , which is the number of events in the fitting region to the total number of events, and use it to find the  $W$  decay width. The definition is:

$$R = \frac{N(in\ sensitive\ region)}{N(total\ event\ number)} \quad (5.18)$$

For this check, we will take the sensitive region to be the area that changes its shape for different  $W$  widths, which will be from 85 to 200 GeV. From the data sample, we need to subtract the background in the sensitive region and calculate the ratio. This leads to  $R = 0.02771 \pm 0.001059$ . The error is statistical only and dependent on the total number of events available.

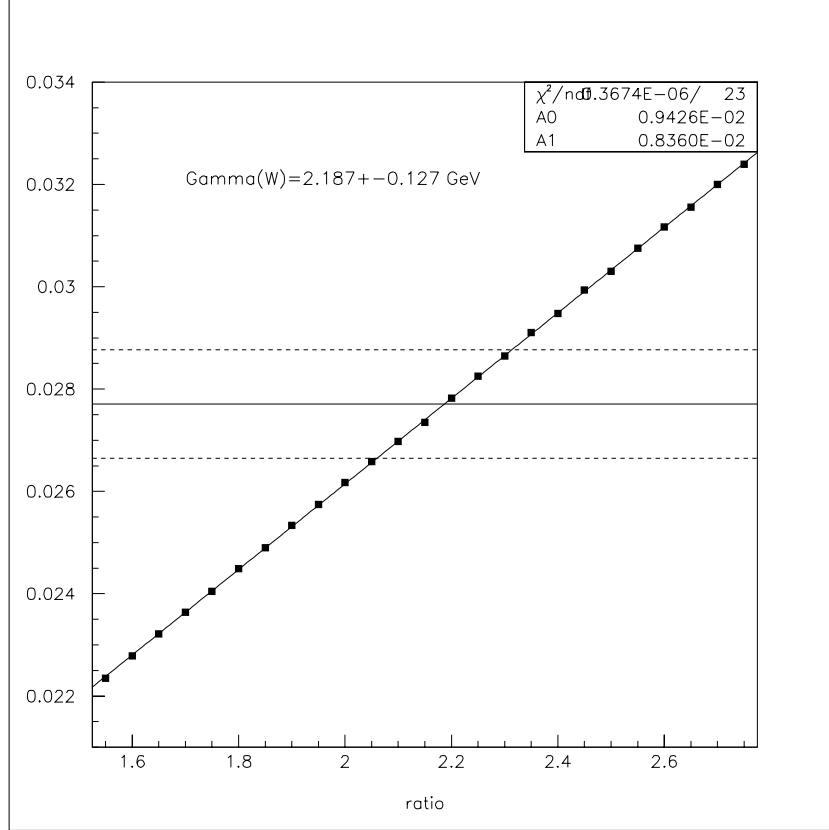


Figure 5.15: The ratio vs.  $W$  decay width. The dots are the ratio from MC for different  $W$  decay widths. It is fit with a straight line. The horizontal solid line represents the ratio from data. The two horizontal dashed lines show the uncertainties.

From the Monte Carlo templates, we also calculate the ratio  $R$  for different  $W$  decay widths. The plot for this ratio vs. decay width is shown in Figure 5.15.

We fit the ratio with a straight line and found that it can be written as  $R = 0.00836 * \Gamma(W) + 0.009426$ . In the y-axis, we take the ratio of the data and its upper and lower limits, shown as the solid line and two dashed lines respectively. This leads to the result of  $\Gamma(W) = 2.187 \pm 0.127 GeV$ , compared to the maximum likelihood fitting result  $\Gamma(W) = 2.208 \pm 0.125 GeV$  for the same fitting region. Both errors shown here are statistical only.

The ratio method takes only event numbers for width extraction, instead of spectrum shape as in the maximum likelihood fitting. This could lose some information that is useful in the width determination. Nevertheless, we can see that results from both methods are in good agreement.

#### 5.4.2 $P_t(W)$ Cut

We select  $W$  events by requiring that  $P_t(W) < 15 GeV$ . For high  $P_t(W)$  events, the detector response will be different and needs to be constrained. Our fitting results should not be sensitive to this cut. This means that if we change this cut, the measurement result should not change much and be well within statistical error. To study this effect, we changed the  $P_t$  cut by 3 GeV. Similar to the above study, we take the sensitive region to be from 85 to 200 GeV. For these three various  $P_t(W)$  cuts, the results are listed in the Table 5.6.

From the table, we can see that for various  $p_t(W)$  cuts, both the ratio fitting and maximum likelihood fitting give consistent results and the differences between various  $W$  pt cuts are very small compared to their statistical uncertainty. We also notice that the results for  $p_t(W) < 12 GeV$  have a smaller difference from that of  $p_t(W) < 15 GeV$  and are much closer than these for  $p_t(W) < 18 GeV$ . The reason is that the cut  $p_t(W) < 15 GeV$  was chosen because detector response will be different for events with  $p_t(W)$  above 15 GeV. In this checking, we keep the detector response the same and our results show the effects of high- $p_t(W)$ .

$p_t(W)$ cut	12 GeV	15 GeV	18 GeV
Total $W$ events in (0-200)	22377(91.4%)	24479	25716(105%)
$W$ events in (85-200)	629(88.2%)	713	783(110%)
Total background in (0-200)	388.4(82.8%)	469.1	538.1(115%)
Background in (85-200)	41.52(87.1%)	47.69	53.95(113%)
Ratio $R \pm \delta R$	0.02672(99)	$0.02771 \pm 0.00106$	0.02896(125)
Ratio fitting(GeV)	2.201(14)	$2.187 \pm 0.127$	2.229(42)
Likelihood fitting(GeV)	2.213(5)	$2.208 \pm 0.125$	2.235(27)

Table 5.6: Consistency check for various  $p_t(W)$  cuts. The  $p_t(W)$  cut is changed by 3 GeV. The numbers in parenthesis of the first four rows are percentages compared to a  $p_t(W)$  cut of 15 GeV. For the last three rows, the numbers in parenthesis mean the difference starting from the least significant digit compared to  $p_t(W) < 15 \text{ GeV}$ . The ratio, ratio fitting results and likelihood fitting results are all within their uncertainties.

### 5.4.3 Non-linearity of the Calorimeter

The non-linearity of the calorimeter has been studied previously [63]. It was found that an extra non-linear term may exist for electron energy:

$$E_{true} = \alpha E^{obs} + \beta + 0.0001 \times (E^{obs} - 45.6)^2 \quad (5.19)$$

where  $E^{obs}$  is the measured energy and  $E_{true}$  is the true energy of electron.

We study the effect of this term in two different ways. One is to add this extra term into the energy correction when we calculate electron energy for  $W$  event selection. Thus we will have a different number of events when this term is added, compared to what we have without this term. We use the new data sample for fitting and calculate the difference. The other way is to add the non-linear term into the MC, which can also see the difference. The results are listed in Table 5.7.

As we can see from the table, both methods give compatible results. They are in good agreement. Since the extra term is added to real data in one method and to the MC in the other, the results from both methods are in opposite signs.

The uncertainties due to non-linearity of the calorimeter are negligible, compared to other systematic errors. There are two reasons why the results are small. First, the non-linear term is added to electron energy only and the missing  $E_t$  is calculated afterwards. The change in transverse mass will be much smaller than the change in the energy of the electrons itself. The second reason is that the extra term will have large effects on electron above 150  $GeV$  and will be smaller for electrons with energies less than 100  $GeV$ . In the transverse mass spectrum, the event numbers above 125  $GeV$  in each bin is less than 10. The most important part to fitting is the transverse mass spectrum around 100  $GeV$ , where the extra non-linearity term will not have much effect.

Fitting region $m_T(GeV)$	Non-linear term in $W$ event selection	Non-linear term in CMS MC
all(0-200)	+11	-6
65-200	+8	-5
75-200	+7	-2
85-200	+4	-3
90-200	0	+2
95-200	+10	-11

Table 5.7: The fitting width change due to non-linearity term of calorimetry. Units are in  $MeV$ . The non-linear term of the calorimeter is added to electron energy, either in electron energy calibration when  $W$  events are selected or in CMS MC simulation. The fitting results are compared to the normal fitting results without the non-linear term.

#### 5.4.4 Ensemble Study for Background

To study the effect of background shape due to its uncertainty, we did an ensemble study of the background. We used the multinomial distribution to let the background in each bin fluctuate while at the same time keeping the total background the same. The multinomial distribution is defined as:

$$P(N_1, N_2, \dots, N_{ch}) = N_{total} \prod_{i=1}^{N_{ch}} \frac{P_i^{N_i}}{N_i!} \quad (5.20)$$

where  $ch$  is the number of bins,  $N_{total}$  is the total number of events,  $P_i$  is the original probability and  $N_i$  is the event number in the  $i$ -th bin.

For each background distribution, we add it to the MC sample and fit to data. In this study, we took total ensample  $N=40$  and here are the results. For the fitting region of  $m_T$  in  $(90, 200)$ , the ensemble study gives the mean fitting width of  $2.238 \text{ GeV}$  and the sigma of  $0.039 \text{ GeV}$ . This gives us a shift of  $0.007 \text{ GeV}$  compared to our fitting mean value  $\Gamma(W) = 2.231 \text{ GeV}$ . As a comparison, for fitting region of  $m_T$  in  $(0, 200)$ , ensemble study has the results of mean equal to  $2.183 \text{ GeV}$  and sigma equal to  $0.025 \text{ GeV}$ . The shift is  $0.002 \text{ GeV}$ , compared to  $\Gamma(W) = 2.185 \text{ GeV}$ . The results show that the ensemble study is consistent with our fitting measurement.

#### 5.4.5 Upper Limit of Fitting Region

The change of upper limit for the fitting region will also change the fitting result. We expect the difference to be very small, due to a very limited number of events in the region above  $150 \text{ GeV}$ . To check this effect, the results are listed in Table 5.8.

We can see that the difference is very small, compared to the statistical uncertainty.



Fitting Region in $m_T$	Fitting Result	Compared to $m_{Tin}(90, 200)$
90-160	2.225	-0.006
90-170	2.221	-0.010
90-180	2.226	-0.005
90-190	2.235	+0.004

Table 5.8: The effect of change of fitting region upper limit, compared to our standard fitting region.

#### 5.4.6 Different Bin Size

In this section, we will study the effect of different bin sizes on the fitting result.

Since statistics in the high end is very limited, we tried to combine bins in the high end. First we double the bin size above 100 GeV and keep the lower region the same, i.e. 5 GeV per bin from 0 to 100 GeV and 10 for 100 to 200 GeV. This gives the fitting width 2.164 GeV, without obvious change.

Next, we double the high end bin size so that the number of events in each bin will be around 10. The bin sizes are 5 GeV for 0 to 100 GeV, 10 GeV for 100 to 160 GeV and 20 GeV for 160 to 200 GeV. We have the  $W$  width of 2.163 GeV.

From this study, we can see that the bin size will obviously not change the fitting width.

#### 5.4.7 Statistical Error Checks

We perform two statistical error checking to see if statistical uncertainty is consistent with the data.

The first one is to consider the different event numbers in the fitting regions. For the various fitting regions, the number of events is different. For the data set

of a narrow region, the data sample is a subset of a wide one and we can check if the fitting results are consistent.

For the fitting region (85, 200) of  $m_T$ ,  $N_{event} = 713 \equiv N_1 + N_2$  and fitting width  $\Gamma_W = 2.203 \text{ GeV}$  with  $\sigma = 0.124 \text{ GeV}$ . On the other hand, for fitting region (95, 200) of  $m_T$ ,  $N_{event} = 196 \equiv N_1$  and  $\Gamma_{W1} = 2.285 \text{ GeV}$ . So statistically  $\sigma(\Gamma_W - \Gamma_{W1}) = \sigma\sqrt{N_2/N_1} = 0.201 \text{ GeV}$ . The actual difference between  $\Gamma_W$  and  $\Gamma_{W1}$ , which is  $0.082 \text{ GeV}$ , is much less than the allowed error. We can conclude that the fitting results for various fitting regions are in good consistency.

The second one is the function of likelihood. We fit the likelihood by a 4th order polynomial. In that case, we will have an unsymmetric statistical uncertainty. If we fit the likelihood with a 2nd order polynomial around the peak, we should have consistent results. If a 2nd order polynomial is used, we have  $\Gamma(W) = 2.168 \pm 0.111 \text{ GeV}$ , compared to  $\Gamma(W) = 2.164_{-0.107}^{+0.110} \text{ GeV}$  with 4th order polynomial fitting. There is no obvious deviation.

## 5.5 Prospective for Run II

The Run II is underway at the time this thesis is being written. The upgraded DØ detector [87, 88] has a central 2 Tesla magnetic field for sign identification of particles. Another major improvement will be the installation of a silicon microstrip tracker (SMT) for precise tracking and vertex finding. In addition, a preshower detector, both central and forward, was installed to help identify electrons.

We will expect a  $2 \text{ fb}^{-1}$  integrated luminosity in the Run IIa. This could produce about 3 million  $W$  events in each of the  $e$  and  $\nu$  channels [89]. Supposing we have the same event selection efficiency, we could have a data sample of about 500 thousand events, a factor of 20 increase over Run I. With this sample, the statistical uncertainty could decrease by a factor of more than 4. It is hard to directly estimate the systematic uncertainty. With more  $W$  and  $Z$  events, we

could determine our parameters in the MC more precisely and systematic errors will also decrease. Assuming it could decrease by a factor of about 3-4, we will expect the uncertainty for  $W$  width measurement to be at the neighborhood of 50  $MeV$ .

## 5.6 Conclusion

We have directly measured the  $W$  boson decay width,  $\Gamma(W)$  by fitting the transverse mass in  $W \rightarrow e\nu$  events that was recorded in Run 1B of 1.8 TeV  $p\bar{p}$  collisions.

By using the fast CMS Monte Carlo, we have measured the  $W$  width  $\Gamma(W)$  to be

$$\Gamma(W) = 2.231^{+0.145}_{-0.138}(stat) \pm 0.092(sys) GeV \quad (5.21)$$

$$= 2.231 \pm 0.172 GeV \quad (5.22)$$

This result is consistent with the Standard Model prediction [12] of

$$\Gamma(W) = 2.0937 \pm 0.0025 GeV. \quad (5.23)$$

As a comparison, the indirect measurement from previous analysis in  $D\bar{O}$  yields  $\Gamma(W) = 2.152 \pm 0.066 GeV$  [64, 69].

# Bibliography

- [1] Donald H.Perkins, Introduction to High Energy Physics,(Addison Wesley),  
Third Edition
- [2] UA1 Collaboration, G. Arnison *et al.*, Phys. Lett. B **122**, 103 (1983).
- [3] UA2 Collaboration, P. Bagnaia *et al.*, Phys. Lett. B **122**, 476 (1983).
- [4] UA1 Collaboration, G. Arnison *et al.*, Phys. Lett. B **126**, 398 (1983).
- [5] UA2 Collaboration, P. Bagnaia *et al.*, Phys. Lett. B **129**, 130 (1983).
- [6] S. Glashow, Nucl. Phys. **22**, 579 (1961).
- [7] S. Weinberg, Phys. Rev. Lett. **19**, 1264 (1967) .
- [8] A. Salam in Elementary Particle Theory, edited by N. Svartholm (Almquist  
and Wiksells, Stockholm), 367 (1969).
- [9] W. Bardeen, H. Fritzsch, M. Gell-Mann in Scale and Conformal Symmetry in  
Hadron Physics, edited by R. Gatto (Wiley, New York), 139 (1973).
- [10] D. Gross and F. Wilczek, Phys. Rev. D **8**, 3633 (1973).
- [11] S. Weinberg, Phys. Rev. Lett. **31**, 494 (1973).
- [12] D.E. Groom *et al.*.(Particle Data Group), European Physical Journal, C15  
(2000)

- [13] C. Albajar *et al.*, Physics Letter, B253, 503(1991)
- [14] J. Alitti *et al.*, Physics Letter, B276, 365(1992)
- [15] T. Affolder *et al.*, Physics Review Letter, 25 3347(2000)
- [16] F. Abe *et al.*, Physics Review, D52, 2624(1995)
- [17] B. Abbott *et al.*, Physics Review, D61, 072001(2000)
- [18] M. Acciarri *et al.*, Physics Letter, B454, 386(1999)
- [19] G. Abbiendi *et al.*, Physics Letter, B507 29(2001)
- [20] P. Abreu *et al.*, Physics Letter, B459 382(1999)
- [21] R. Barate *et al.*, European Physical Journal, C17 241(2000)
- [22] G. Kane, Modern Elementary Particle Physics, Perseus Books,1993
- [23] C. Quigg, Gauge Theories of the Strong, Weak and Electromagnetic Interaction, Benjamin/Cummings, 1983
- [24] I.J.R. Aitchison and A.J.G. Hey, Gauge Theories in Particle Physics, Institute of Physics Publishing, Bristol and Philadelphia, 1993
- [25] P. Aurenche, The Standard Model of particle physics, *hep-ph/9712342 (1997)*
- [26] J. Rosner, M. Worah, and T. Takeuchi, “Oblique Corrections to the W Width”, Phys. Rev.**D49**, 1363(1994).
- [27] ATLAS Technical Report, CERN
- [28] J. Kalinowski and P.M. Zerwas, Phys. Lett. B 400, 112(1997)
- [29] A. D. Martin, R. G. Roberts and W. J. Stirling, Phys. Lett. **B306**, 147 (1993) and erratum-ibid **B309** 492 (1993).

- [30] LEP Electroweak Working Group, CERN Report No. CERN/PPE/93-157, 26 August 1993 (to be published).
- [31] T. Affolder *et al.* (CDF Collaboration), FERMILAB-PUB-00/085-E (2000)
- [32] I.F Ginzburg, K. Melnikov, About the modern “experimental value” of  $W$  boson width, MZ-TH/95-03 ENSLAPP-A505/95, September 12, 1997.
- [33] David Summers, Transverse mass as a means of measuring the  $W$  width at the Tevatron, CERN-TH/96-205, August 1996.
- [34] J. Smith, W. L. Van Neerven, J. A. Vermaseren, “Transverse Mass and Width of the  $W$  boson”, Phys. Rev. Lett. 50 22 (1983) 1738-1740.
- [35] V.D.Barger and R.J.N.Phillips, 'Collider Physics', Volume 71 of Frontiers in Physics, Addison-Wesley(1987)
- [36] Design Report, The DØ Experiment at the Fermilab  $p\text{-}\bar{p}$  Collider, November 1994
- [37] S. Abachi *et al.*, Nucl. Instr. and Methods, A338, 185, 1994
- [38] H.T. Edwards, Ann. Rev. Nucl. Part. Sci. 35, 605(1985)
- [39] S. Abachi *et al.* (DØ Collaboration), Phys. Rev. Lett. 74, 2632 (1995).
- [40] F. Abe *et al.* (CDF Collaboration), Phys. Rev. Lett. 74, 2632 (1995).
- [41] S. Snyder DØ internal note 2500
- [42] A. R. Clark et al., Nucl. Instr. and Methods, A315, 193, 1992
- [43] J. Kadyk, Nucl. Instr. and Methods, A300, 436, 1991
- [44] “The Central Drift Chamber for the DØ Experiment: Design, Construction and Test”, Ties Behnke, Ph.D Thesis, State University of New York at Stony Brook, August 1989 (unpublished).

- [45] “Results from a Beam Test of the DØ Forward Drift Chambers”, R. Avery *et al.*, IEEE Trans. Nucl. Science (1992).
- [46] R. Fernow, Introduction to experimental particle physics Cambridge(1986)
- [47] C.Fabjan. Calorimetry in high-energy physics. In: Thomas Ferbel, editor, Experimental Techniques in High Energy Physics, pages 257 - 324. Addison-Wesley, 1987
- [48] J. Kotcher, Response of the DØ calorimeter to Cosmic Ray Muons. PhD. thesis, New York University, New York, 1992 (unpublished)
- [49] M. Abolins et al., “The level one framework” *DØ internal note 328 revised, DØ internal note 705, 1988.*
- [50] M. Abolins et al., *IEEE Trans. Nucl. Sci.*, **36(1):384-389**, 1989
- [51] M. Abolins, D. Edmunds, P.Laurens, and B. Pi, *Nucl. Instr. and Methods*, **A289:543-560**, 1990
- [52] J. Drinkard, “The DØ Level 1.5 Calorimeter Trigger,” *DØ internal note 2274*
- [53] The Zebra manual is available at: <http://consult.cern.ch/writeup/zebra/>
- [54] P. Grudberg, Measurement of the  $W$  and  $Z$  Boson Production Cross Sections in  $p\bar{p}$  Collisions at  $\sqrt{s} = 1.8$  TeV with the DØ Detector, PhD thesis, University of California at Irvine, Irvine, California, 1997 (unpublished).
- [55] M. Narain, *DØ internal note 2386*
- [56] M. Narain, U. Heintz, *DØ internal note 2355*
- [57] R. Raja et al., “Reconstruction and Analysis: Tracking Packages, CalorimeterPackages,” *DØ internal note 1006 (1990)*

- [58] R. Raja, “H-matrix Analysis for top→lepton + jets,” *DØ internal note 1192 (1992)*
- [59] M. Narain, “Electron Identification in the DØ Detector”, Proceedings of the American Physical Society Division of Particles and Fields Conference, Fermilab, Batavia, Illinois (1992).
- [60] C. Gerber, R. Piegaia, M. Mostafa, DØ Note #3550, hep-ex/0010026.  
G. Manning, DØ Note #2452.
- [61] B. Abbott *et al.* (DØ Collaboration), Phys. Rev. D 58, 092003(1998), FER-MILAB PUB-97/422-E, hep-ex/9801025.
- [62] B. Abbott *et al.* (DØ Collaboration), *Phys. Rev. Lett.* 80, 3000 (1998).
- [63] B. Abbott *et al.* (DØ Collaboration), Phys. Rev. Letters 84, 222(2000), FER-MILAB PUB-99/259-E, hep-ex/9909030.
- [64] Jamal Tariazi, Ph.D. thesis, ‘A Measurement of the Cross Section Ratio of the  $W$  and  $Z$  Electronic Decays and the Total Width of the  $W$  with the DØ Detector’ University of California at Irvine, 1997(unpublished)
- [65] R. Kehoe, R. Astur, *DØ internal note 2908*
- [66] V. Daniel Elvira, *DØ internal note 3139*
- [67] B. Abbott *et al.* (DØ Collaboration), Phys. Rev. D 61, 072001(2000), FER-MILAB PUB-99/171-E, hep-ex/9906025.
- [68] Private e-mail exchange with Marcel Demarteau(DØ Collaboration)
- [69] Jamal Tarazi, *PhD thesis, University of California, Irvine, Irvine(1997) (unpublished)*



- [70] P. Grudberg, Measurement of the  $W$  and  $Z$  Boson Production Cross Sections in  $p\bar{p}$  Collisions at  $\sqrt{s}=1.8\text{TeV}$  with the  $D\bar{O}$  Detector, PhD thesis, University of California, Berkeley, 1997
- [71] “Measurement of the transverse momentum of dielectron pairs in proton-antiproton collisions”, D. Casey, PhD Thesis, Univ. of Rochester, 1997.
- [72] G. Steinbrueck, Measurement of the Angular Distribution of Electrons from  $W$  boson Decay at  $D\bar{O}$ ., University of Oklahoma, 1999
- [73] C. Balazs and C.-P. Yuan, Phys. Rev. **D56** 5558-5583,1997
- [74] Eric Flattum, *PhD thesis, Michigan State University, 1996 (unpublished)*
- [75] I. Adam, *PhD thesis, Columbia University, 1997 (unpublished), Nevis Report #294*
- [76] B. Abbott et al, *Physics Rev. Lett. 80 5498 (1998)*
- [77] J. Botts *et al.* (CTEQ Collaboration), Phys. Lett. B **304**, 159 (1993);  
H.L. Lai *et al.* (CTEQ Collaboration), Phys. Rev. D **51**, 4763 (1995);  
H.L. Lai *et al.* (CTEQ Collaboration), Phys. Rev. D **55**, 1280 (1997);  
<http://www.phys.psu.edu/cteq>.
- [78] P. B. Arnold and M. H. Reno, Nucl. Phys. **B319**, 37 (1989). Erratum, Nucl. Phys. **B330**, 284 (1990).
- [79] G. A. Ladinsky and C. P. Yuan, *Phys. Rev. D* **50**, 4239 (1994).
- [80] B. Abbott et al., “Measurement of the Transverse Momentum of  $Z$  Boson produced in  $p\bar{p}$  Collisions at  $\sqrt{s} = 1.8 \text{ TeV}$ ” *to be published in Phys.Rev., D*
- [81] F. A. Berends and R. Kleiss, Zeit. Phys. **C27** 365(1985)

- [82] F. Paige and S. Protopopescu, ISAJET 5.20: A Monte Carlo Event Generator for  $pp$  and  $\bar{p}p$  Reactions. *BNL-38034 (1996)*
- [83] U. Heintz, DØ internal Note 2268.
- [84] I. Adam, DØ internal Note 2298.
- [85] U. Heintz, DØ internal Note 2739.
- [86] A.D. Martin, *et al.*, Parton Distribution and the LHC:  $W$  and  $Z$  Production, hep-ph/9907231
- [87] “The DØ Upgrade”, Fermilab Pub-96/357-E, available at: <http://higgs.physics.lsa.umich.edu/dzero/d0doc96/d0doc.html>
- [88] “DØ Technical Design Summary”, DØ internal note 2962.
- [89] “QCD and Weak Boson Physics in RUN II”, Fermilab-Pub-00/297, Editors: U. Baur, R.K. Ellis and D. Zeppenfeld, November 2000